

Syracuse University

SURFACE

Dissertations - ALL

SURFACE

December 2015

Fundamentals of microlayer evaporation and its role on boiling heat transfer enhancement

An Zou

Syracuse University

Follow this and additional works at: <https://surface.syr.edu/etd>



Part of the [Engineering Commons](#)

Recommended Citation

Zou, An, "Fundamentals of microlayer evaporation and its role on boiling heat transfer enhancement" (2015). *Dissertations - ALL*. 417.

<https://surface.syr.edu/etd/417>

This Dissertation is brought to you for free and open access by the SURFACE at SURFACE. It has been accepted for inclusion in Dissertations - ALL by an authorized administrator of SURFACE. For more information, please contact surface@syr.edu.

Abstract

Boiling, a dynamic and multiscale process, is widely used in industrial applications as it can transfer a large amount of heat over a small surface area. It has been studied for over five decades; however, a comprehensive understanding of the process is still lacking. The bubble ebullition cycle (nucleation, growth and departure) happens over a very short time-span (milliseconds) making it challenging to study the near-surface interfacial characteristics of a single bubble, which involves a microlayer. The microlayer is a thin film present at the bubble base and varies from nano-scale to micro-scale in thickness. The dynamics of the microlayer dictates bubble growth and departure, making it of significant importance in understanding the fundamental behavior of the boiling phenomenon, and is the focus of this work.

Firstly, a new mechanism of boiling enhancement based on the additional evaporation of the thin film is proposed and validated by fabricating micro-ridges on a surface and testing its boiling performance. A critical height of the ridges is found to exist, determined by the film thickness, below which no enhancement is observed while above which similar enhancements are achieved regardless of the ridge height. An analytical model is developed to determine the critical height from the experimental results.

Secondly, the effect of ridge spacing on boiling enhancement is investigated. A ~120% enhancement in the critical heat flux is attained with only 18% increase in surface area due to the presence of ridges. The new enhancement mechanism is determined to be the early evaporation of microlayer, which leads to an increase in the bubble growth rate and departure frequency. Three enhancement regions are mapped based on ridge spacing and height: full enhancement

region, partial enhancement region, and no enhancement region. The mechanism of early evaporation of microlayer is further verified by comparison of the bubble growth rate of a laser-created vapor bubble on a ridge-structured surface and on a plain surface.

Next, *in-situ* imaging of microlayer and contact line region is performed in a steady-state vapor bubble created by laser heating. The *in-situ* measurement of contact angle of vapor bubbles is conducted. For the laser power studied, the contact line readily forms in regular DI water which contains dissolved air, while in degassed water, the microlayer covers the entire bubble base. The vapor bubble contact angle is found to resemble a drop contact angle on the same surface if the three-phase contact line forms; otherwise it is dependent on the curvature of the microlayer and the bubble, and decreases with increasing heating power. The overall heat transfer coefficient and width of the evaporating region in the microlayer are estimated using experimental data and finite-element-method based numerical simulations, thus defining an upper limit to the heat transfer coefficient possible in nucleate boiling and thin-film evaporation.

Finally, the contact line and microlayer behavior during bubble formation, growth, and movement is investigated. During bubble formation, the microlayer initially covers the entire bubble base, decreases in thickness as the bubble grows, and eventually forms the three-phase contact line. The surface wettability strongly affects contact line motion. On hydrophobic Trichlorosilane (FOTS) surface, the bubble remains adhered to the surface and does not follow the laser movement; while on hydrophilic SiO_2 surface, the bubble moves smoothly following the laser. This difference in behavior is determined to originate from the change in direction of the liquid-vapor surface tension force, which results in a negative net force on FOTS surface inhibiting the bubble from following the laser, while it results in a positive net force on SiO_2 surface causing the bubble to move on the surface.

FUNDAMENTALS OF MICROLAYER EVAPORATION AND ITS ROLE ON BOILING HEAT TRANSFER ENHANCEMENT

By

An Zou

B.S., East China University of Science and Technology, 2007

M.S., East China University of Science and Technology, 2010

DISSERTATION

Submitted in partial fulfillment of the requirements for the Degree of Doctor
of Philosophy in Mechanical Engineering

Syracuse University
December 2015

Copyright © An Zou 2015
All Rights Reserved

To my family for their unconditional love and support

Acknowledgements

First and foremost I would like to thank my advisor, Dr. Shalabh C. Maroo, for introducing me to the field of thermal management and heat transfer science. In these years, Dr. Maroo has always been supportive of my study and research. His patience, continuous encouragement and enthusiasm, and insightful suggestions are the main driving forces to lead me through my PhD study. He is a nice person and great teacher. He is concerned not only with research progress but also with students' life and future. I am truly grateful for having him as my PhD advisor and I am sure that I will keep benefitting in my future career from what I have learned in these years.

I wish to thank my thesis committee members, Dr. Jeongmin Ahn, Dr. H. Ezzat Khalifa, Dr. Roger R Schmidt, Dr. Radhakrishna Sureshkumar, and Dr. Jianshun Zhang for their valuable and insightful guidance on the work. Their advice has helped improve this work.

I express my sincere gratitude to my Master's thesis advisor, Professor Gance Dai, for leading me into scientific and engineering research, and inspired my interest in transport phenomena. I really appreciate his help.

I also want to thank all the research group members, Ashish Chanana, Sumith YD, Dharendra Singh, Nikolay Rodionov, Dan Stack, Peetak Mitra, Ryan Olson, and Geoffrey Vaartstra for their friendship and support. I wish them all the best in their current and future endeavors.

Finally, I give my appreciation to my family for their unconditional support and love through my life. They are my supreme inspiration to continuously seek and pursue higher knowledge and achievement in my life. I gratefully dedicate this thesis to them.

Table of Contents

Abstract.....	i
Acknowledgements.....	vi
List of Symbols.....	xi
List of Tables.....	xv
List of Figures.....	xvi
1. Introduction.....	1
1.1 Boiling Curve.....	1
1.2 Bubble Ebullition Cycle.....	3
1.3 Boiling Heat Transfer Mechanisms and Models.....	7
1.3.1 Transient Conduction Model.....	9
1.3.2 Microconvection Model.....	9
1.3.3 Microlayer Evaporation Model.....	10
1.3.4 Contact Line Evaporation Model.....	11
1.4 Critical Heat Flux (CHF).....	11
1.4.1 Hydrodynamic Models.....	12
1.4.2 Bubble Nucleation Models.....	13
1.4.3 Mushroom Bubble Models.....	14
1.4.4 Force Balance Models.....	15
1.5 Objectives of Current Work.....	17
2. Boiling Enhancement by Micro/Nano Structures.....	19
2.1 Irregular Structures.....	19
2.1.1 Nanofluids.....	19
2.1.2 Graphite fibers.....	20
2.1.3 Sponge-like layers.....	21
2.1.4 Nanowires and Carbon Nanotubes (CNT).....	22
2.1.5 Nanorods and Nanoparticles.....	26
2.2 Regular Structures.....	28
2.2.1 Fins, Pillars and Cavities.....	28
2.2.2 Channels/Ridges.....	31

2.3 Hybrid Structures	33
2.4 Enhancement Mechanism	36
2.4.1 Increased Nucleation Site Density.....	37
2.4.2 Facilitated Liquid Supply	37
2.4.3 Separated Liquid/Vapor Pathways	39
2.4.4 Increased Roughness	40
2.4.5 Summary.....	40
3. Critical Height of Micro/Nano Structures to Enhance CHF.....	42
3.1 Hypothesis.....	42
3.2 Experimental Methods	44
3.2.1 Sample Fabrication.....	44
3.2.2 Boiling Rig and Experiment Procedure.....	49
3.2.3 Uncertainty Analysis	51
3.3 Experimental Results.....	52
3.3.1 Heat Loss from the Sample	52
3.3.2 Effect of Heat Conduction.....	53
3.3.3 Boiling Curves.....	55
3.4 CHF Enhancement Mechanisms	57
3.4.1 Effect of Wettability	59
3.4.2 Effect of Liquid Supply	62
3.4.3 Effect of Roughness.....	64
3.4.4 Additional Evaporation of the Thin Film	65
3.5 Summary	69
4. Early Evaporation of Microlayer to Enhance CHF.....	71
4.1 Hypothesis.....	71
4.2 Experimental Results.....	75
4.2.1 Sample Fabrication.....	75
4.2.2 Boiling Curves.....	76
4.2.3 Effect of Ridge Shape.....	78
4.2.4 Effect of Ridge Spacing.....	79
4.2.5 Enhancement Map	83

4.3 Early Evaporation of Microlayer.....	84
4.3.1 Experimental Setup and Sample Fabrication.....	85
4.3.2 Experimental Procedure	87
4.3.3 Bubble Volume.....	88
4.3.4 Validation of Early Evaporation of Microlayer.....	89
4.4 Summary	93
5. Steady Vapor Bubble in Pool Boiling.....	94
5.1 Introduction	94
5.2 Experimental Methods	97
5.2.1 Sample Fabrication.....	97
5.2.2 Experimental Setup and Sample Preparation	99
5.3 Bubble Contact Angle	101
5.3.1 Bubble Contact Angle Measurement.....	101
5.3.2 Uncertainty Analysis	102
5.3.3 Experimental Results.....	103
5.4 Microlayer underneath the Steady Bubble	106
5.4.1 Fringe Patterns.....	106
5.4.2 Microlayer Profile.....	108
5.4.3 Effect of Microlayer on Bubble Contact Angle.....	110
5.4.4 Steady Bubble with Completely Wetted Base.....	111
5.5 Heat Transfer Characteristics in Evaporating Region.....	112
5.5.1 Bubble Growth Rate in Regular Water.....	112
5.5.2 Heat Transfer Coefficient in Evaporating Region.....	115
5.6 Summary	118
6. Contact Line Behavior of a Vapor Bubble	120
6.1 Introduction	120
6.2 Experimental Methods	121
6.3 Contact Line Behavior in Bubble Formation and Growth	121
6.4 Contact Line Behavior in Bubble Movement	124
6.4.1 Bubble Movement on Hydrophobic surface.....	124
6.4.2 Bubble Movement on Hydrophilic Surface.....	129

6.5 Summary	133
7. Conclusions and Future Work	135
7.1 Conclusions	135
7.1.1 Critical Height of Microstructures to Enhance CHF	135
7.1.2 Early Evaporation of Microlayer to Enhance CHF	135
7.1.3 Steady Vapor Bubble in Pool Boiling	136
7.1.4 Contact Line Behavior of a Vapor Bubble	137
7.2 Future Work	137
7.2.1 Early Evaporation Induced by Hydrophobic Patterns	137
7.2.2 Boiling Heat Transfer Mechanisms	138
7.2.3 “Controlling” the Bubbles Behavior in Boiling	139
References	141
Vita.....	161

List of Symbols

A_s	surface area
A_v	vapor area
C_E	Ergun coefficient
c_{pl}	liquid heat capacity
CHF_{exp}	experimental critical heat flux
CHF_{mp}	model predicted critical heat flux
d	liquid flow distance
D_C	diameter of the capillary tube
D_d	bubble departure diameter
D_W	diameter of the wetting area on the surface
E_a	natural convection to air underneath the sample
E_b	heat dissipated by boiling
E_w	natural convection to water outside the boiling area
f	bubble departure frequency
f_{ne}	additional evaporation factor
H	ridge height
H_{cr}	critical height
H_f	full enhancement height
h_{lv}	latent heat
K	permeability of the wicking structure
k_l	thermal conductivity of liquid

k_s	thermal conductivity of solid
k_v	thermal conductivity of vapor
L	expanded boiling length
M_{H_2O}	molecular weight of water
N_a	nucleation site density
P_l	liquid pressure
Pr_l	Prandtl number
q_{cl}	contact line evaporation
q_{ml}	microlayer evaporation
q_{sl}	evaporation of thermal boundary layer
q_{tc}	transient conduction
q''	heat flux
q_a''	heat flux of natural convection to air underneath the sample
q_b''	boiling heat flux
q_w''	heat flux of natural convection to water outside the boiling area
$q''_{CHF,c}$	CHF due to capillary limit
$q''_{CHF,w}$	CHF due to wicking limit
R	bubble radius
r	roughness
r_c	radius of cavity
r_e	radius of bubble embryo
r_{dryout}	radius of dryout region
S	spacing

ΔT	superheat; temperature difference
ΔT_{OSB}	wall superheat for onset of boiling
T_R	temperature reading from thermocouples
T_{sat}	liquid saturation temperature
T_w	wall temperature
T_∞	temperature at infinite distance
t	time
t_d	bubble departure time
t_w	waiting time
t_g	bubble growth time
E_{bg}	increased bubble growth rate
V	volume of liquid
V_b	bubble volume
V_{ne}	bubble volume contributed by additional evaporation
V''_0	liquid volume flux
v	flow velocity
v_l	specific volume of liquid
v_v	specific volume of vapor
W	width
Wi	dimensionless wicking number
α_l	thermal diffusivity of liquid
β	thermal expansion
δ	thickness

δ_0	thin film thickness
δ_t	thermal boundary layer thickness
θ	contact angle
θ_{rec}	receding contact angle
θ_w	contact angle in Wenzel state
θ_{CB}	contact angle in Cassie-Baxter state
λ_D	most dangerous wavelength
λ_H	Helmholtz critical wavelength
μ_l	liquid viscosity
ν_l	liquid kinematic viscosity
ρ_l	liquid density
ρ_v	vapor density
σ	surface tension
σ_{lv}	liquid-vapor surface tension
σ_{sl}	solid-liquid surface tension
σ_{sv}	solid-vapor surface tension
φ	tilted angle of surface
φ_s	porosity of the structure
φ_w	ratio of the wetting area to the projected area in CB state

List of Tables

Table 2 - 1 Boiling enhancement by sponge-like layers.....	22
Table 2 - 2 Boiling enhancement by nanowires and CNTs	25
Table 2 - 3 Boiling enhancement by nanorods and nanoparticles	28
Table 2 - 4 Boiling enhancement by fins, pillars, and cavities.....	31
Table 2 - 5 Boiling enhancement by channels and ridges	33
Table 2 - 6 Boiling enhancement by hybrid structures.....	36
Table 3 - 1 Geometry of fabricated ridges	48
Table 3 - 2 Contact angles in two directions for all samples	60
Table 3 - 3 Effect of capillary pumping flow	63
Table 3 - 4 Comparison between experimental data and Chu's model	65
Table 4 - 1 Geometry of fabricated ridges	76
Table 5 - 1 Sample surfaces and liquids used for experiments.....	98

List of Figures

Figure 1 - 1 Typical boiling curve: (a) ΔT controlled; (b) q'' controlled	3
Figure 1 - 2 Schematic showing the various stages of bubble ebullition cycle	4
Figure 1 - 3 Thermal boundary layer close to the heated surface	4
Figure 1 - 4 Heat transfer mechanisms during (a) bubble growth and (b) bubble departure.....	8
Figure 1 - 5 Schematic CHF mechanisms and models (a) hydrodynamic model (b) mushroom bubble model (c) force balance model	14
Figure 2 - 1 Porous layer of graphite fibers to enhance boiling heat transfer published in literatures	21
Figure 2 - 2 Sponge-like layers to enhance boiling in published literatures.....	21
Figure 2 - 3 Nanowires and CNTs in literatures	24
Figure 2 - 4 Nanorods and nanoparticles in the literatures	26
Figure 2 - 5 Fins, pillars, and cavities in the literatures.....	29
Figure 2 - 6 Channels and ridges in the literatures	32
Figure 2 - 7 Hybrid structures in the literatures	35
Figure 2 - 8 Evaporation momentum forces acting on a growing bubble (a) on plain surface (b) at the corner of the fin base and resulted seperated liquid vapor flow pathways	39
Figure 3 - 1 Schematic of the bubble base depicting the microlayer and its three regions	42
Figure 3 - 2 Distribution of local temperature and heat flux in microlayer region.....	43
Figure 3 - 3 Hypothesis of thin film rupture and evaporation underneath the bubble on ridge- structured surface for pool boiling heat transfer enhancement.....	44

Figure 3 - 4 Sample design (a) side view (b) top view (c) bottom view (sizes are not scaled)	45
Figure 3 - 5 Fabrication procedure of Si and SiO ₂ ridges (not scaled).....	47
Figure 3 - 6 SEM images of side view of Si ridges with height (a) 300 nm, (b) 585 nm, and (c) 1.27 μm; SiO ₂ ridges with height (d) 585 nm, (e) 1.06 μm, and (f) 1.53 μm.....	48
Figure 3 - 7 Boiling rig setup.....	50
Figure 3 - 8 Heat loss from the sample.....	52
Figure 3 - 9 Effect of heat conduction in the fabricated samples	53
Figure 3 - 10 Actual boiling area calibration.....	54
Figure 3 - 11 Boiling curves based on projected area for Si samples.....	55
Figure 3 - 12 Boiling curves based on projected area for SiO ₂ samples	56
Figure 3 - 13 Boiling curves based on the wetting area for Si samples.....	57
Figure 3 - 14 Boiling curves based on the wetting area for SiO ₂ samples	57
Figure 3 - 15 Liquid droplets on a structured surface in (a) Wenzel state and (b) Cassie-Baxter state.....	59
Figure 3 - 16 Stretched droplet along ridges and different contact angles in two directions	60
Figure 3 - 17 Comparison of CHF in current work to (a) Dhir's model and (b) Kandlikar's model	61
Figure 3 - 18 Pumping effect of spacing between ridges.....	62
Figure 3 - 19 Comparison between experimental data and Chu's model.....	65
Figure 3 - 20 Comparison of experimental CHF's with the analytical model	69
Figure 4 - 1 Microlayer connected to bulk liquid with large ridge space	71
Figure 4 - 2 Early evaporation and four types of ridges	73

Figure 4 - 3 SEM images of fabricated ridges	75
Figure 4 - 4 Boiling curves of samples with the ridge spacing of 5 μm and 9 μm	77
Figure 4 - 5 Boiling curves of samples with the ridge spacing of 20 μm	77
Figure 4 - 6 Boiling curves of samples with the ridge spacing of 48 μm	78
Figure 4 - 7 Comparison of CHF enhancements in current work with literatures.....	78
Figure 4 - 8 Three regions of CHF enhancement	79
Figure 4 - 9 Relation between enhancement variable and H/H_f	81
Figure 4 - 10 Relation between the full enhancement variable and the ratio of ridge spacing to width	82
Figure 4 - 11 CHF enhancement map.....	83
Figure 4 - 12 Schematic of the experiment setup for bubble growth rate comparison.....	86
Figure 4 - 13 Schematic of the samples for bubble growth rate comparison (a) plain surface (b) ridge-structured surface	87
Figure 4 - 14 (a) schematic of bubble image; typical bubble image on plain surface (b1) white (b2) red illumination and on ridge-structured surface (c1) white (c2) red illumination.....	89
Figure 4 - 15 Bubble growth on plain surface with (a) white and (b) red illumination.....	90
Figure 4 - 16 Bubble growth on ridge-structured surface with (a) white and (b) red illumination	90
Figure 4 - 17 Comparison of bubble growth rate on plain surface and ridge-structured surface .	91
Figure 4 - 18 Comparison of CHF on plain surface and ridge-structured surface.....	92
Figure 5 - 1 Description of fabricated sample for (a) SiO_2 surface (b) FOTS surface (not scaled)	97

Figure 5 - 2 Diffusion profile of air in degassed water with time.....	100
Figure 5 - 3 (a) Typical bubble image. Bubble shape and contact angle estimation on (b) hydrophilic SiO ₂ and (c) hydrophobic FOTS surface	101
Figure 5 - 4 Images of a bubble on normal SiO ₂ in regular water at different laser power (a) 120 mW (b) 140 mW (c) 160 mW (d) 180 mW (e) 200 mW.....	103
Figure 5 - 5 Images of a bubble on normal SiO ₂ in degassed water at different laser power (a) 120 mW (b) 140 mW (c) 160 mW (d) 180 mW (e) 200 mW	103
Figure 5 - 6 Images of a bubble on FOTS in degassed water at different laser power (a) 120 mW (b) 140 mW (c) 160 mW (d) 180 mW (e) 200 mW	104
Figure 5 - 7 Bubble base diameter and bubble diameter	104
Figure 5 - 8 Bubble contact angles on the hydrophilic surface.....	105
Figure 5 - 9 Bubble contact angle on the hydrophobic surface	106
Figure 5 - 10 Optical paths for laser interferometry	107
Figure 5 - 11 Typical fringe patterns	108
Figure 5 - 12 Optical images of the bubble with 50× magnification under white-light and HeNe laser illumination and microlayer profile (a) bubble on normal SiO ₂ surface in regular water (b) bubble on normal SiO ₂ surface in degassed water and (c) FOTS surface in degassed water	109
Figure 5 - 13 Evolution of the microlayer with bubble growth	110
Figure 5 - 14 Two types of bubble (a) a bubble with a microlayer wetting the entire bubble base (b) a bubble with three-phase contact line: non-evaporating region (R3), evaporating film region (R2), bulk meniscus region (R1) and the dry spot (R4)	112
Figure 5 - 15 Calculation of bubble volume	113

Figure 5 - 16 Bubble volume growth with constant laser power	114
Figure 5 - 17 Bubble diameter and base growth with constant laser power	114
Figure 5 - 18 Contact angle evolution with constant laser power.....	115
Figure 5 - 19 Simulation domain	116
Figure 5 - 20 Approximation of heat transfer coefficient and width of evaporating region.....	117
Figure 5 - 21 Surface temperature profile.....	118
Figure 6 - 1 Contact line behavior during bubble formation and growth	123
Figure 6 - 2 Contact line behavior on FOTS surface with white light.....	126
Figure 6 - 3 Contact line behavior on FOTS surface with red light	127
Figure 6 - 4 Change of direction of surface tension at point <i>a</i> on FOTS surface	129
Figure 6 - 5 Contact line behavior on SiO ₂ surface with white light	131
Figure 6 - 6 Contact line behavior on SiO ₂ surface with red light	131
Figure 6 - 7 Microlayer profile at point <i>a</i> during laser movement	132
Figure 6 - 8 Change of direction of surface tension at point <i>a</i> on SiO ₂ surface.....	133

1. Introduction

Boiling is a liquid-to-vapor phase-change process which involves the formation of liquid-vapor interfaces (bubble generation) at discrete sites on the heated surface or in a superheated liquid layer adjacent to the heated surface.¹ Boiling is one of the most efficient heat transfer mechanisms as it utilizes the latent heat of vaporization and allows a large amount of heat to be transferred over a small surface area. It is widely used in industries that require the removal of high heat flux, from small electronic chip cooling² to large scale power plants.³ Pool boiling, as the name implies, is the type of boiling that occurs when the heater surface is submerged in an extensive pool of stagnant liquid. Typically pool boiling heat flux is limited to $\sim 50\text{-}100\text{ W/cm}^2$ on flat surfaces, with this limit called the critical heat flux (CHF). Great effort has been made to enhance pool boiling heat transfer coefficient and CHF.⁴

1.1 Boiling Curve

Boiling heat transfer can be described by a boiling curve, which was introduced by Nukiyama⁵ in 1934. Boiling curve is a plot of heat flux transferred to liquid versus wall superheat, which is defined as the temperature difference between the heated surface and the pool of liquid. Figure 1 - 1 (a) depicts a typical boiling curve with controlled superheat on a flat horizontal plate. With the increase of superheat, natural convection heat transfer occurs due to the presence of gravity, as shown in the region a-c. At a certain value of superheat (point c), nucleation is triggered and vapor bubbles begin to form. Point c is defined as the onset of boiling. After the inception of boiling, more heat can be transferred to the liquid due to increase in bubble formation and the use of latent heat of vaporization, resulting in a vertical line c-d in the boiling curve. In region d-e, at

relatively low superheat, the distance between adjacent nucleation sites is large enough to prevent bubbles to merge together, and hence it is termed as the isolated bubble regime. With the increase of superheat, in region e-f (regime of slugs and column), more and more nucleation sites are activated and the adjacent sites are close enough to allow the bubbles to coalesce. The vapor generation rate also increases so that numerous vapor columns form and rise in the liquid away from the surface. Once the bubble generation rate is larger than the bubble removal rate, at point f, the heated surface cannot be completely rewetted by liquid and a partial vapor film forms over the surface. This vapor film serves as a thermal resistance due to its low thermal conductivity, resulting in the decrease of local heat transfer coefficient and heat flux. The heat flux at point f is called critical heat flux (CHF). In region f-g, more and more nucleation sites are covered by the vapor film as superheat increases, leading to the decrease of the overall heat transfer coefficient and heat flux. This region is termed as transition boiling, which is generally characterized by rapid and severe fluctuations in local heat transfer coefficient and heat flux because the dry regions formed are unstable. At point g, the vapor film completely covers the surface and the heat flux increases with superheat primarily due to radiation heat transfer. This region is known as film boiling, as shown in g-h.

Figure 1 - 1 (b) shows a typical boiling curve, with q'' controlled. There are two main differences compared to ΔT (superheat) controlled boiling curve. The first one is region c-d. At boiling inception, as more heat is suddenly removed by liquid, the temperature of the heated surface decreases, resulting in a horizontal line c-d in the curve. The other difference is the transition from nucleate boiling to film boiling. After CHF, a very small increase of heat flux induces a dramatic increase in the surface temperature due to reduced heat transfer to the liquid, as shown in region f-g. The surface temperature can be as high as 500°C, or even more than 1000°C in

such cases. In industrial applications, this jump in temperature can damage the surface or even cause it to melt; hence, CHF must be avoided and serves as the operation limit.⁶

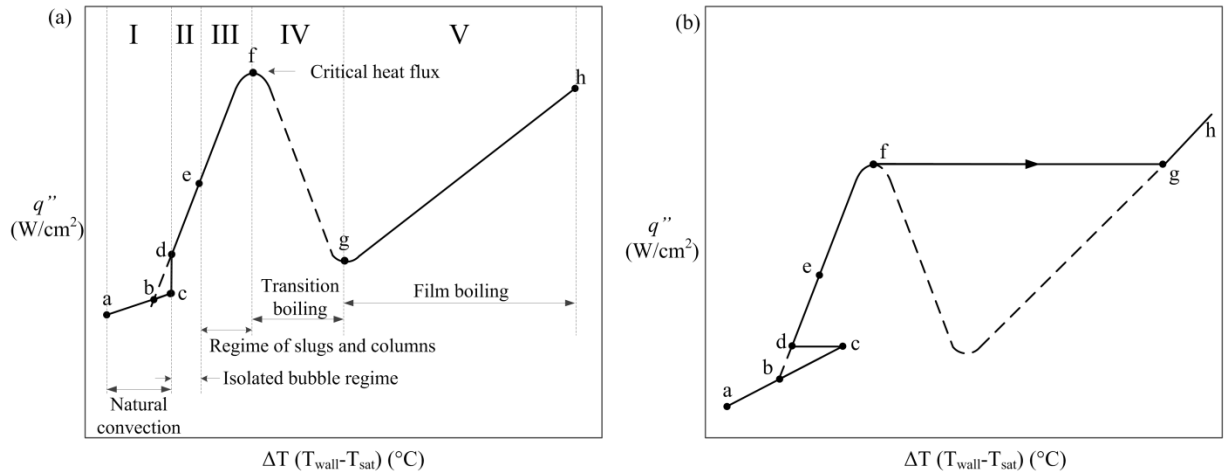
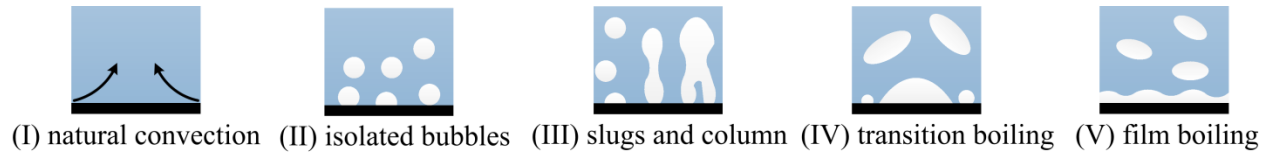


Figure 1 - 1 Typical boiling curve: (a) ΔT controlled; (b) q'' controlled

1.2 Bubble Ebullition Cycle

Figure 1 - 2 shows a typical bubble ebullition cycle in nucleate boiling. It is generally divided into four stages: waiting period, inertia-controlled growth stage, heat-transfer-controlled growth stage, and departure.

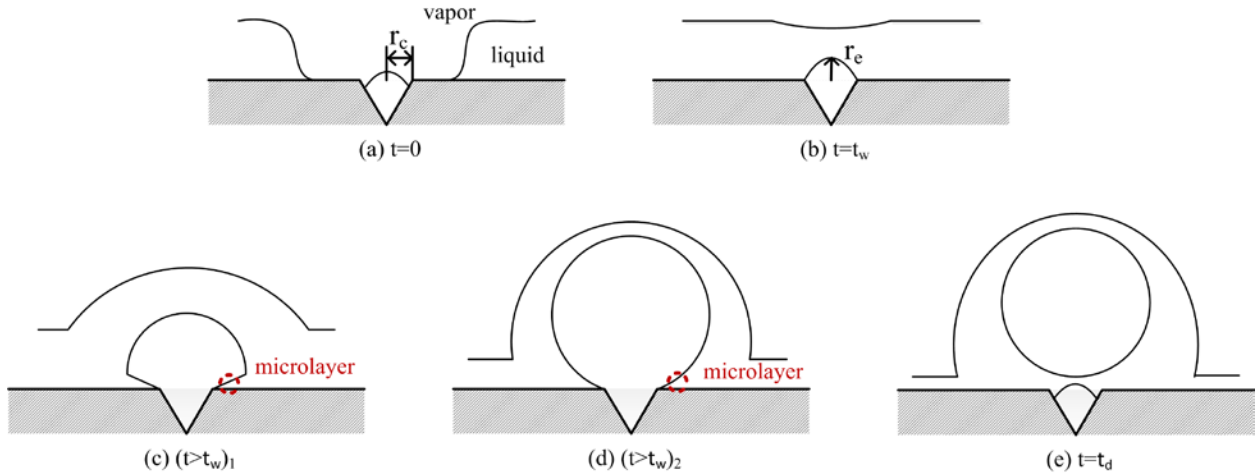


Figure 1 - 2 Schematic showing the various stages of bubble ebullition cycle⁶

For a certain nucleation site (a cavity with radius r_c), after the release of a previous bubble, a small bubble embryo with radius r_e exists due to the residual vapor left by the previous bubble (Figure 1 - 2 (a)). Due to the temperature difference between the liquid and surface, the liquid adjacent to the surface is heated and a thermal boundary layer forms close to the wall (Figure 1 - 3). This process, known as waiting time (t_w), is shown in Figure 1 - 2 (a) and (b). However, this nucleation site is active only when the value of r_c is located in the range shown in Eq. (1-1).⁷

$$\left\{ \begin{matrix} r_{c,min} \\ r_{c,max} \end{matrix} \right\} = \frac{\delta_t}{4} \left[1 - \frac{T_{sat}(P_l) - T_\infty}{T_w - T_\infty} \cdot \begin{Bmatrix} +1 \\ -1 \end{Bmatrix} \cdot \sqrt{\left(1 - \frac{T_{sat} - T_\infty}{T_w - T_\infty} \right)^2 - \frac{12.8\sigma T_{sat}(P_l)}{\rho_v h_{lv} \delta_t (T_w - T_\infty)}} \right] \quad \text{Eq. (1-1)}$$

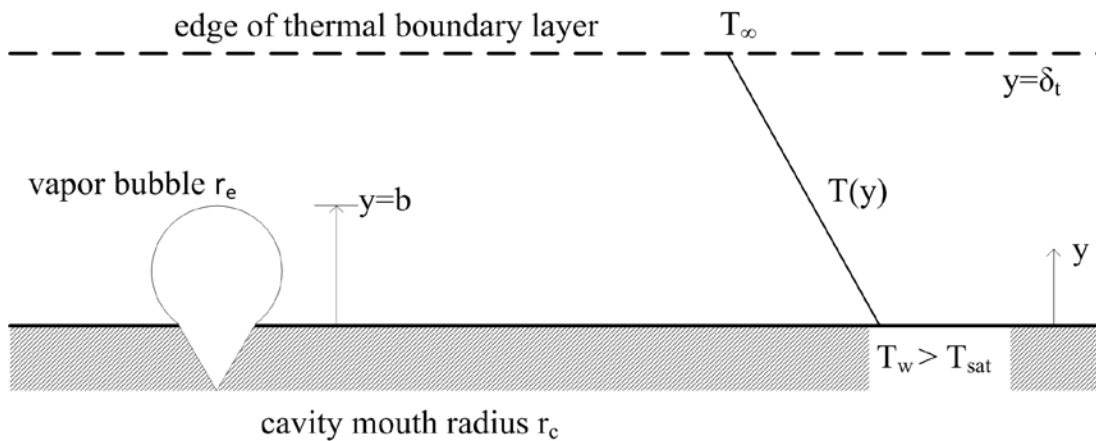


Figure 1 - 3 Thermal boundary layer close to the heated surface

Eq. (1-1) implies that for those nucleation sites with values of r_c bigger than $r_{c,max}$, the embryo bubble is so large that it protrudes beyond the thermal boundary layer. Hence, the upper portion of the bubble is exposed to bulk liquid that is not superheated, leading to the condensation of vapor to counteract vaporization occurred at lower portion of the bubble. Consequently, the embryo bubble is prevented from growing. For those nucleation sites with values of r_c smaller than $r_{c,min}$, the embryo bubble is so small that the required equilibrium superheat is bigger than current superheat level, and thus to make these sites active, higher superheat is necessary. Eq. (1-1) also indicates that in the case that superheat decreases, eventually the terms inside the square root will become zero and result in $r_{c,max} = r_{c,min}$. Hence, only one specific cavity size is active under this superheat. If the superheat keeps decreasing further, no real solution exists, implying that no cavities can be activated. In other words, there exists a threshold value for superheat, below which all nucleation sites with any size could not be active; this threshold value is the minimum superheat required to initiate and maintain nucleate boiling.

Once the nucleation site is activated, the bubble forms and starts growing. At the early stage of bubble growth, the liquid adjacent to the interface is superheated. The heat transfer is greater than what is required to evaporate the liquid, and the bubble growth is limited by the rate of momentum transfer to the surrounding liquid. At this stage, the bubble is nearly hemispherical. There exists a thin microlayer of liquid underneath the bubble. Most heat and mass transfer occurs in this thin layer. As the bubble grows, inertia force becomes relatively small and the heat transfer becomes the limiting factor. This is the case because the liquid temperature decreases away from the interface; thus, bubble growth is limited by the rate at which heat can be conducted to the liquid-vapor interface. This stage is heat transfer controlled and the bubble is pulled into a spherical shape by the surface tension. By assuming that the total kinetic energy of

the moving liquid equals the work done at the liquid boundaries (ignoring irreversible conversion to internal energy, gravitational effects and work done by viscous forces), B.B. Mikic *et al.* derived the bubble growth rate as Eq. (1-2) in a uniformly superheated liquid by solving the continuity equation⁸.

$$R^+ = \frac{2}{3} \left[(t^+ + 1)^{\frac{3}{2}} - (t^+)^{\frac{3}{2}} - 1 \right] \quad \text{Eq. (1-2)}$$

where

$$R^+ = \frac{R}{B^2/A}; \quad t^+ = \frac{t}{B^2/A^2}$$

$$A = \left[\frac{\pi \Delta T h_{lv} \rho_v}{7 T_{sat} \rho_l} \right]^{\frac{1}{2}}; \quad B = \left[\frac{12}{\pi} \text{Ja}^2 \alpha_l \right]^{\frac{1}{2}}$$

Ja is Jakob number which is the ratio of sensible to latent energy absorbed during liquid-vapor phase change (Eq. (1-3)).

$$\text{Ja} = \frac{\rho_l c_{pl} (T_\infty - T_{sat}(P_\infty))}{\rho_v h_{lv}} \quad \text{Eq. (1-3)}$$

Eq. (1-2) is valid in both inertial controlled and heat transfer controlled stages. The authors⁹ further extended the model to the bubble growth in a non-uniform temperature field which approximated the conditions in boiling from a heated surface, as shown in Eq. (1-4).

$$R(t) = \frac{2\text{Ja}\sqrt{3\pi\alpha_l t}}{\pi} \left\{ 1 - \frac{T_w - T_\infty}{T_w - T_{sat}} \left[\left(1 + \frac{t_w}{t} \right)^{1/2} - \left(\frac{t_w}{t} \right)^{1/2} \right] \right\} \quad \text{Eq. (1-4)}$$

where the time for waiting period t_w is obtained from Eq. (1-5).

$$t_w = \frac{1}{4\alpha_l} \left\{ \frac{r_c}{\text{erfc}^{-1} \left[\frac{T_{sat} - T_\infty}{T_w - T_\infty} + \frac{2\sigma T_{sat}(v_v - v_l)}{(T_w - T_\infty) h_{lv} r_c} \right]} \right\}^2 \quad \text{Eq. (1-5)}$$

During bubble growth, surface tension acting along the contact line holds the bubble on the surface, while other forces (such as buoyancy, drag, and inertia forces) try to pull the bubble away. As the bubble grows bigger, these detaching forces become stronger and eventually overcome the surface tension. The bubble then departs from the surface to end one bubble ebullition cycle. One of the most famous models to predict bubble departure diameter was proposed by Zuber¹⁰ as Eq. (1-6).

$$Bo_d^{1/2} = \left(\frac{\sigma}{g(\rho_l - \rho_v)} \right)^{-1/6} \left[\frac{6k_l(T_w - T_{sat})}{q''} \right]^{1/3} \quad \text{Eq. (1-6)}$$

where Bo_d is departure Bond number which is defined by Eq. (1-7).

$$Bo_d = \frac{g(\rho_l - \rho_v)D_d^2}{\sigma} \quad \text{Eq. (1-7)}$$

The bubble departure frequency depends directly on the bubble departure size and bubble growth rate. Based on similarity between the bubble release process and natural convection, Zuber¹¹ also suggested Eq. (1-8) as the relation between bubble departure diameter and bubble departure frequency.

$$fD_d = 0.59 \left[\frac{\sigma g(\rho_l - \rho_v)}{\rho_l^2} \right]^{1/4} \quad \text{Eq. (1-8)}$$

1.3 Boiling Heat Transfer Mechanisms and Models

During a bubble ebullition cycle, there are numerous mechanisms that transfer heat from the surface to liquid (Figure 1 - 4). As shown in Figure 1 - 4 (a), during bubble growth, the evaporation of the microlayer (q_{ml}), which is defined as the liquid layer between the quickly growing hemispherical bubble and the wall, contributes to bubble growth. The evaporation of thermal boundary layer (q_{sl}) also occurs surrounding the bubble cap. After the formation of the

dry spot due to the partial dryout of the microlayer, another mechanism of evaporation (q_{cl}) occurs at the three-phase contact line, also contributing to the bubble growth. In addition to these evaporation mechanisms, boiling heat transfer includes the background natural convection (q_{nc}) and microconvection (q_{mc}) due to the perturbation of the liquid adjacent to the bubble and disruption in the natural convection boundary layer. Heat transfer mechanisms during the bubble departure process are illustrated in Figure 1 - 4 (b). In addition to these mechanisms appearing in the bubble growth, when fresh liquid rewets the dryout region, transient conduction (q_{tc}) occurs into the advancing liquid front, thus superheating the liquid and forming the thermal boundary layer.

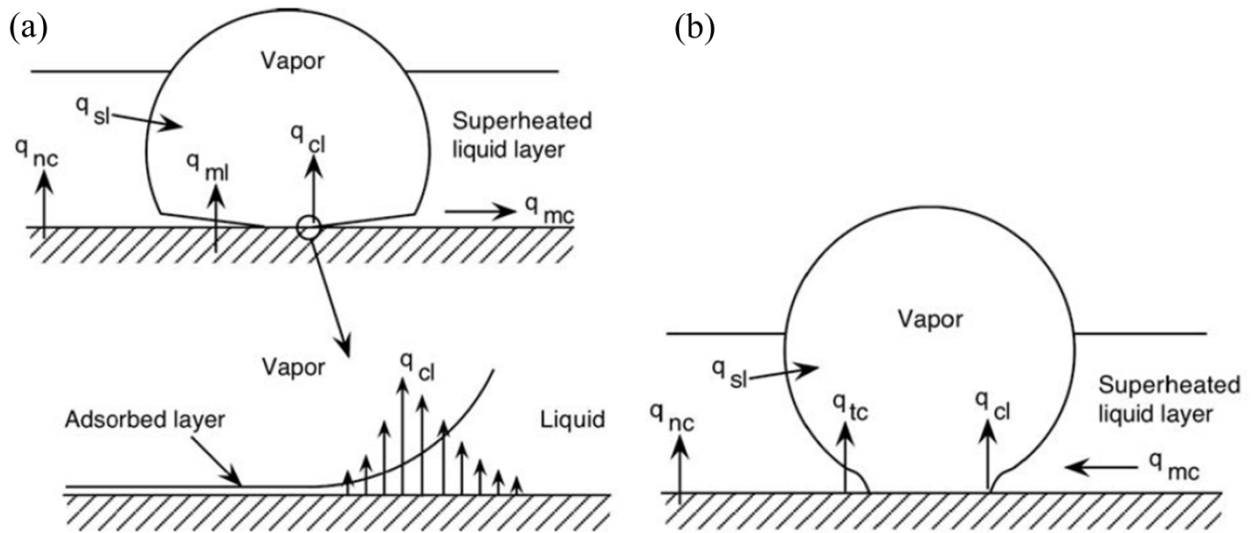


Figure 1 - 4 Heat transfer mechanisms during (a) bubble growth and (b) bubble departure¹²

There are so many heat transfer mechanisms involved in boiling that it has been debated over many decades which mechanisms dominate the boiling process. The boiling heat transfer models can be classified as four categories: transient conduction model, microconvection model, microlayer evaporation model, and contact line evaporation model.

1.3.1 Transient Conduction Model

A widely accepted transient conduction model was proposed by Mikic *et al.*,¹³ who suggested that a part of the superheated layer is removed with the departing bubble. The diameter of the affected area in which the superheated layer is taken away by the bubble is twice that of departing bubble. After the bubble departs, the liquid at bulk temperature flows into the affected area and comes into contact with the surface. By assuming that only pure conduction occurs in the liquid in the affected area, the average heat flux over the complete boiling surface was proposed as Eq. (1-9).

$$q'' = \frac{2\pi k_l (T_w - T_{sat})}{\sqrt{\pi \alpha_l}} \cdot N_a \cdot [D_b^2 (\sqrt{f})] \quad \text{Eq. (1-9)}$$

The transient conduction model has been recently further supported by Chen *et al.*¹⁴ and Gerardi *et al.*¹⁵ With a constant surface temperature, Chen *et al.*¹⁴ experimentally observed that the a narrow peak of heat flux corresponded to both bubble departure and new bubble nucleation, while heat flux reduced during bubble growth. Gerardi *et al.*¹⁵ demonstrated that transient conduction dominates the total boiling heat flux.

1.3.2 Microconvection Model

Many early models for boiling heat transfer are based on the assumption that convective heat transfer from surface to liquid is facilitated by the bubble growth and departure due to induced motions of its surrounding liquid⁶. One of the most successful applications of this approach was proposed by Rohsenow¹⁶. He developed a model (Eq. (1-10)) attributing high heat transfer coefficient of boiling to liquid flow behind the wake of departing bubbles.

$$\frac{q''}{\mu_l h_{lv}} \left[\frac{\sigma}{g(\rho_l - \rho_v)} \right]^{1/2} = \left(\frac{1}{C_{sf}} \right)^{1/r} \text{Pr}_l^{-s/r} \left[\frac{c_{pl}(T_\infty - T_{sat}(P_l))}{h_{lv}} \right]^{1/r} \quad \text{Eq. (1-10)}$$

where $C_{sf} = \sqrt{2}C_b\theta/A$. The value of C_{sf} is dependent on system and its recommended value is in the range between 0.005 and 0.015. Here, r is 0.33 and s is 1.0 for water.

1.3.3 Microlayer Evaporation Model

Moore *et al.*¹⁷ found that the temperature fluctuated on the wall under the bubble during boiling and postulated that microlayer evaporation removed more heat at that region. With constant heat flux, Cooper *et al.*¹⁸ found a sharp drop in surface temperature associated with microlayer evaporation, a recovery in temperature once a dry spot formed, and a small drop again as liquid rewetted the dry spot during bubble departure. Judd *et al.*¹⁹ proposed a model based on microlayer evaporation. The total heat flux q'' consisted of three contributions: microlayer evaporation q_{ml} , nucleate boiling q_{nb} , and natural convection q_{nc} . q_{ml} is given by Eq. (1-11), q_{nb} is adopted from Mikic's model¹³ of Eq. (1-9) and q_{nc} is given by Eq. (1-12). q'' is sum of these three contributions.

$$q_{ml} = 2\pi\rho_l h_{lv} f N_a \int_0^R r [\delta_0(r) - \delta(r, t)] dr \quad \text{Eq. (1-11)}$$

$$q_{nc} = 0.18k_l \left[\left(\frac{g\beta\rho_l^2}{\mu_l^2} \right) \left(\frac{\mu_l c_{pl}}{k_l} \right) \right]^{1/3} (T_w - T_\infty)^{4/3} [1 - C\pi R^2 N_a] \quad \text{Eq. (1-12)}$$

where $\delta_0(r)$ is initial local microlayer thickness, $\delta(r, t)$ represents instantaneous microlayer thickness C is a constant with a recommended value of 1.8 for water.

Eq. (1-11) shows that it is important to get the information about microlayer profile ($\delta(r, t)$) during the bubble ebullition cycle. If the temperature distribution is known simultaneously, the percentage of microlayer evaporation contributed can also be calculated. Many efforts have been made to obtain this information²⁰⁻²³. However, information about microlayer profile during the bubble ebullition cycle and its contribution to the total heat flux is still lacking.

1.3.4 Contact Line Evaporation Model

The contact line evaporation model is based on the observation that heat transfer in boiling is dominated by the evaporation of a thin liquid meniscus at the three-phase contact line. Although only an extremely small area is covered by this thin film, heat transfer rate through it can be very high.²⁴ It can contribute up to 38% of the total heat transferred at a superheat of 3.5 °C and 60% at a superheat of 4.5 °C in the evaporation of a free extended meniscus.²⁵ In nucleate boiling, 10% – 30 % of the total heat is transferred within the narrow contact line region, depending on the exact configuration.^{26,27} The local heat flux near the contact line was observed to be an order of magnitude greater than the average heat flux.²⁸ It is constant when the bubble grows and increases dramatically once the bubble starts departing from surface. This is because when the bubble departs, the meniscus moves over the dried region which is at higher temperature. Stephan *et al.*²⁹ developed a contact line evaporation model that includes heat transfer through the contact line region (Eq. (1-13)) and the macro-region (Eq. (1-14)).

$$q_{cl} = -\frac{h_{lv}}{3v_l r} \frac{d}{dr} \left(\frac{dP_c}{dr} r \delta^3 \right) \quad \text{Eq. (1-13)}$$

$$\frac{\partial}{\partial r} \left(k_l \left(\frac{\partial T}{\partial r} \right) \right) + \frac{\partial}{\partial z} \left(k_l \left(\frac{\partial T}{\partial z} \right) \right) = 0 \quad \text{Eq. (1-14)}$$

Eq. (1-13) and Eq. (1-14) can be simultaneously solved by numerical methods. According to this model, a heat flux in the order of 1500 W/cm² should be observed at a distance around 1 μm away from the contact line.

1.4 Critical Heat Flux (CHF)

CHF is the maximum heat flux that can be reached in a non film-boiling mode. As point f shows in Figure 1 - 1, it is the upper heat flux limit of nucleate boiling. At CHF, the heat cannot be removed from the surface due to the low thermal conductivity of the vapor covering the surface,

thus causing a dramatic increase in surface temperature and possibly causing irreparable damage to the surface. Thus, accurate predictions and enhancement of CHF are essential for the design of a boiling system due to concerns about efficiency and safety. However, a universal CHF trigger mechanism and model has yet to be developed. Current models can be categorized to four types: hydrodynamic models, bubble nucleation models, mushroom bubble models, and force balance models as explained in the following sections.

1.4.1 Hydrodynamic Models

In earlier years many researchers, including Zuber, treated CHF as a purely hydrodynamic phenomenon. Zuber developed a model based on Kelvin-Helmholtz instability,¹⁰ which was further refined by Lienhard *et al.*³⁰. In this model, a vapor column forms at very high heat flux such that the bubble coalesces with the previous bubble formed at the same nucleation site. CHF is triggered when the Helmholtz instability of the large vapor jet breaks the liquid-vapor interface due to the velocity difference between the ascending vapor column and the liquid descending, preventing the liquid from rewetting the surface and eventually the surface is blanketed with vapor. Eq. (1-15) can be used to predict CHF based on the following idealizations (Figure 1 - 5 (a)):

1. The centerline spacing of the vapor columns is equal to the wavelength λ_D , predicted by Taylor instability of the horizontal interface between a semi-infinite liquid region above a layer of vapor
2. The column radius is equal to $\lambda_D/4$
3. The Helmholtz unstable wavelength imposed on the columns is equal to λ_D

$$q''_{CHF} = 0.131 h_{lv} \rho_v \left[\frac{\sigma(\rho_l - \rho_v) g}{\rho_v^2} \right]^{1/4} \quad \text{Eq. (1-15)}$$

Eq. (1-15) does not include the possible effects of geometry, surface condition, and wetting characteristics of the heater surface on CHF. Many models including these effects were developed by modifying Eq. (1-15) to the form of Eq. (1-16).

$$\frac{q''_{CHF}}{q''_{CHF,Z}} = f \left(L/L_b \right) \quad \text{Eq. (1-16)}$$

where $q''_{CHF,Z}$ is Eq. (1-15) and L_b is the bubble length scale defined in Eq. (1-17).

$$L_b = \sqrt{\frac{\sigma}{g(\rho_l - \rho_v)}} \quad \text{Eq. (1-17)}$$

The ratio L/L_b represents the size of a finite-sized heater relative to the expected spacing of the vapor columns.

1.4.2 Bubble Nucleation Models

Rohsenow *et al.*³¹ hypothesized that the bubble departure size and frequency were independent of heat flux while nucleation site density increased with heat flux. More and more nucleation sites were activated with increase of heat flux and CHF occurred when the spacing of the bubbles was so small that neighboring bubbles join and the surface was partially covered by the vapor and eventually becomes fully covered. Based on this mechanism, CHF was expressed as Eq. (1-18).

$$q''_{CHF} = 143 h_{lv} \rho_v \frac{(\rho_l - \rho_v)^{0.6}}{\rho_v} \quad \text{Eq. (1-18)}$$

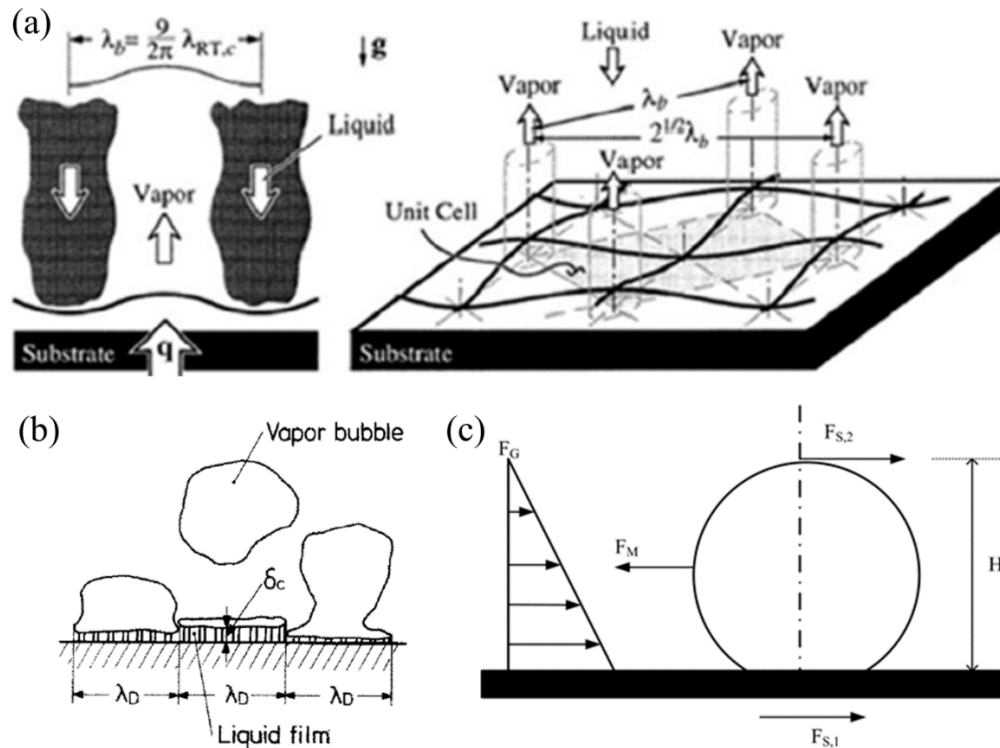


Figure 1 - 5 Schematic CHF mechanisms and models (a) hydrodynamic model³² (b) mushroom bubble model³³ (c) force balance model³⁴

1.4.3 Mushroom Bubble Models

In hydrodynamic models, the vapor phase is treated as continuous columns near CHF, while in bubble nucleation models it is in the form of discrete bubbles. Haramura *et al.*³³ proposed a model based on postulation of combining these two as a large mushroom bubble, under which there existed a thin liquid sublayer consisting of vapor stems and liquid columns (Figure 1 - 5 (b)), which was later observed by experiments³⁵. In this model, CHF occurred when the liquid columns evaporate completely before the large mushroom bubble departed from surface. By assuming the sublayer thickness as $\lambda_H/4$ and the centerline spacing of large bubbles as λ_D , Eq. (1-19) (Katto's model) was developed to predict CHF.

$$q''_{CHF} = 0.72 h_{lv} \rho_v \left[\frac{\sigma(\rho_l - \rho_v)g}{\rho_v^2} \right]^{1/4} \left(\frac{A_v}{A_s} \right)^{5/8} \left(1 - \frac{A_v}{A_s} \right)^{5/16} \left[\frac{\frac{\rho_l + 1}{\rho_v}}{\left(\frac{11\rho_l + 1}{16\rho_v} \right)^{3/5}} \right]^{5/16} \quad \text{Eq. (1-19)}$$

Eq. (1-19) is in good agreement with Eq. (1-15) if the ratio A_v/A_w is given as Eq. (1-20).

$$\frac{A_v}{A_s} = 0.584 \left(\frac{\rho_v}{\rho_l} \right)^{0.2} \quad \text{Eq. (1-20)}$$

Guan *et al.*³⁶ had a similar philosophy for heat flux approaching CHF: liquid macrolayer and vapor jets existed under a mushroom bubble. But in their model, CHF occurred when the vapor momentum flux was sufficient to lift the liquid macrolayer up and away from the surface. CHF was expressed by Eq. (1-21).

$$q''_{CHF} = 0.2445 \rho_v h_{lv} \left[\frac{\sigma(\rho_l - \rho_v)g}{\rho_v^2} \right]^{1/4} \left[1 + \frac{\rho_v}{\rho_l} \right]^{1/4} \left(\frac{\rho_v}{\rho_l} \right)^{1/10} \quad \text{Eq. (1-21)}$$

In Katto's model, it was assumed that the thin liquid sublayer was replenished only after the mushroom bubble departed from surface. This assumption had been questioned by many researchers because it was observed experimentally that the large mushroom bubbles were separated from a sublayer by long, larger vapor jets, implying that the layer was continuously replenished. The good agreement to Zuber's model was only dimensionally consistent.⁶

1.4.4 Force Balance Models

A number of experimental studies showed the effect of surface wettability on CHF.⁶ However, none of the above CHF mechanisms and models includes it directly. In a more recent study, Kandlikar³⁴ proposed a model by analyzing forces exerted on a bubble (Figure 1 - 5 (c)), including bubble growth momentum force (depended on heat transfer), surface tension, buoyancy, and gravity. CHF occurs when momentum force dominates over the sum of the forces that hold the bubble to the surface, such as surface tension. Once this happens, bubbles expand

on the surface and merge together; eventually the vapor film forms and covers the whole surface. The bubble momentum force can be related to heat flux as in Eq. (1-22).

$$F_M = \frac{q_I'' \times H_b \cdot 1}{h_{lv}} \times \frac{q_I'' \times H_b \cdot 1}{h_{lv}} \cdot \frac{1}{\rho_v} \cdot \frac{1}{H_b \cdot 1} \quad \text{Eq. (1-22)}$$

where q_I'' is the heat flux at the interface, which is an average value during the growth of the bubble since its inception and H_b is the height of the bubble.

Based on the assumption that the affected area by a single bubble has a diameter twice that of the bubble, and bubble departure diameter is half of the Taylor instability wavelength of a vapor film over the heater surface, Eq. (1-23) was obtained to predict CHF.

$$q_{CHF}'' = h_{lv} \rho_v^{1/2} \left(\frac{1 + \cos\theta}{16} \right) \left[\frac{2}{\pi} + \frac{\pi}{4} (1 + \cos\theta) \cos\phi \right]^{1/2} [\sigma g(\rho_l - \rho_v)]^{1/4} \quad \text{Eq. (1-23)}$$

In Eq. (1-23), it is more appropriate to use the dynamic receding contact angle for the value of θ , instead of the equilibrium steady contact angle. Compared to previously mentioned models, Kandlikar's model includes the effect of the contact angle directly and also takes into account the effect of micro/nano structures on CHF because one of the widely accepted CHF enhancement mechanisms due to these structures is improved wettability.

However, Eq. (1-23) only includes the effect of micro/nano structures on CHF by the changed wettability due to these structures. The effects of roughness and the elongated contact line are not considered. Chu *et al.* modified Kandlikar's model by changing the term of surface tension to take into account the elongated contact line and obtained Eq. (1-24) to predict CHF.³⁷

$$q_{CHF}'' = h_{lv} \rho_v^{1/2} \left(\frac{1 + \cos\theta}{16} \right) \left[\frac{2}{\pi} \frac{1 + \alpha}{1 + \cos\theta} + \frac{\pi}{4} (1 + \cos\theta) \cos\phi \right]^{1/2} [\sigma g(\rho_l - \rho_v)]^{1/4} \quad \text{Eq. (1-24)}$$

where $\alpha = r \cos\theta_{rec}$.

1.5 Objectives of Current Work

There are four objectives in current work. First, CHF is the maximum heat flux that can be reached by nucleate boiling and it serves as the operational limit of boiling. Thus, increasing CHF allows us to transfer more heat in a safe condition and is the first objective of the current work. Although micro/nano scale surface modifications by fabricating micro/nano structures can enhance boiling heat transfer, the effect of microlayer evaporation on these enhancements is still not well understood. Based on microlayer evaporation, we present a new CHF enhancement mechanism which is the second objective of current work. Further, most literature on evaporating region (in which maximum heat flux occurs) has been reported based on numerical simulations, and characterizing this region experimentally is the third objective. Last, imaging of microlayer and contact line behavior has been studied from a free meniscus of a constrained vapor bubble, and obtaining these images directly in a vapor bubble is the last objective of current work.

In chapter 2, a literature review on boiling heat transfer enhancement by micro/nano surface modification is conducted. Further, the enhancement mechanisms in current literature are summarized.

Chapter 3 introduces a new hypothesis of boiling enhancement achieved by additional evaporation of the thin film present underneath a bubble, which is validated by fabricating ridges with height of about a micrometer and testing its boiling performance. An analytical model is developed to estimate the critical height of microstructures to enhance boiling heat transfer.

Chapter 4 introduces the study of effect of ridge spacing on boiling heat transfer enhancement. A new enhancement mechanism of early evaporation of microlayer is proposed and further

validated by experiments. An enhancement map is introduced to identify the enhancement region depending on ridge height and spacing.

In chapter 5, a steady vapor bubble is created to allow bubble contact angle measurement and imaging of microlayer and contact line region. Heat transfer characteristics of evaporating region are identified based on experimental and numerical investigation.

Chapter 6 introduces the investigation of microlayer and contact line movement behavior on hydrophilic and hydrophobic surfaces, respectively. The different behavior induced by surface wettability is explained by the surface tension acting on the contact line.

2. Boiling Enhancement by Micro/Nano Structures

The critical heat flux (CHF) limit of pool boiling of water on plain surfaces ranges from ~50 W/cm² to ~120 W/cm², depending on the surface material. This value is far less than the theoretically possible evaporation kinetic limit of around 10,000 W/cm² (Eq. (2-1) obtained based on the assumption that all liquid evaporate without condensing back).³⁸ Hence, there is a large potential for enhancing CHF. Various researchers over the last few years have made an effort to enhance CHF by micro/nano scale surface modifications due to the development of micro/nano scale fabrication techniques.^{4,39}

$$q_{max} = \rho_v h_{lv} \sqrt{RT/2\pi} \quad \text{Eq. (2-1)}$$

Based on the appearance, the surface modification can be divided into three categories: irregular structures, such as porous layer deposited by boiling nanofluids, graphite fibers, sponge-like layers, nanowires/carbon nanotubes (CNT), nano rods/particles etc.; regular geometries, such as micro fins, pillars and cavities, channels, and ridges, etc.; and hybrid structures in which nanowires or nano particles are fabricated on regular geometries. Compared to a plain SiO₂ surface, CHF of boiling water has been increased from ~80 W/cm² to ~200 W/cm² for single irregular-structured or regular-structured surface and ~250 W/cm² for hybrid-structured surface.

2.1 Irregular Structures

2.1.1 Nanofluids

Nanofluids are uniform and stable suspensions of nanoparticles (nominally 1-100 nm in size) in conventional host liquid, such as water, oils, etc..⁴⁰ The concept of nanofluids was first introduced by Choi *et al.*⁴¹ He showed the increase of thermal conductivity of nanofluids made

by suspensions of copper or aluminum nanoparticles in water and other liquids, and further concluded the potential for large increases in heat transfer. You *et al.*⁴² achieved ~200% enhancement of CHF with low concentrations of 0.005 g/l of Al₂O₃-water nanofluids at a pressure of 2.89 psia ($T_{sat} = 60^{\circ}\text{C}$). After that, a large number of researchers made efforts on the use of nanofluids to enhance CHF.³² Several comprehensive reviews of CHF enhancement by boiling nanofluids have been reported.⁴³⁻⁴⁷ Generally speaking, nanofluids at lower concentrations (0.32% – 1.25% by weight) enhance CHF while nanofluids at higher concentrations (4% – 16% by weight) deteriorate CHF.⁴⁸⁻⁵⁰ Although it was the increased thermal conductivity of nanofluids that motivated the research of using nanofluids to enhance pool boiling, it turned out that this enhancement was not related to it. The surface roughness alone did not explain the enhancement, either. Although some researchers claimed that the enhancement was due to surface properties related to thermal effusivity,⁵¹ disjoining pressure,⁵² and shorter Taylor instability wavelength,⁵³ it was widely accepted that the enhancement was attributed to nanoparticles deposition on the surface, resulting in improved wettability and capillarity of the surface.⁵⁴

2.1.2 Graphite fibers

Forming a porous layer by depositing graphite fibers is another way to enhance boiling heat flux. It resulted in ~2 times enhancement in heat transfer coefficient and ~3 times enhancement in CHF.⁵⁵⁻⁵⁷ Researchers bonded commercial graphite fiber to surfaces using epoxy and achieved enhancement. Figure 2 - 1 shows these porous layers. The researchers attributed the enhancement to the high thermal conductivity of the fibers (1200 W/mK) and a large number of embryo cavities.⁵⁶

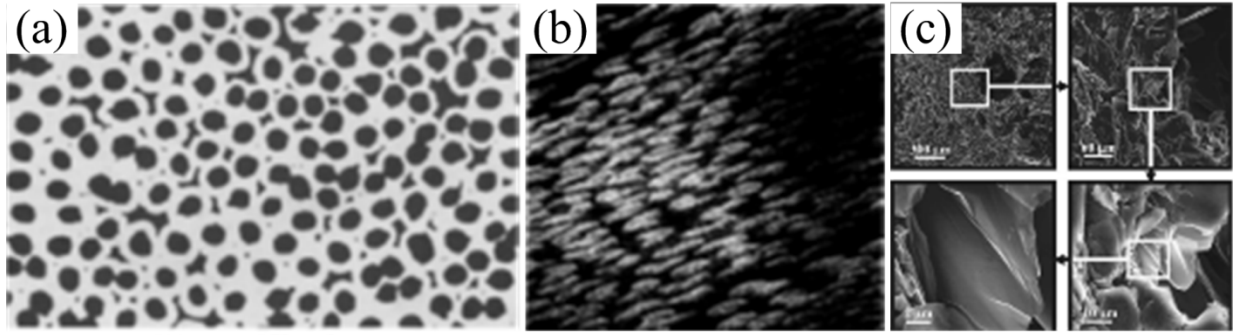


Figure 2 - 1 Porous layer of graphite fibers to enhance boiling heat transfer published in literatures: (a)⁵⁵ (b)⁵⁶ (c)⁵⁷

2.1.3 Sponge-like layers

Li *et al.*⁵⁸ fabricated sponge-like structures on copper surfaces, as shown in Figure 2 - 2 (a), by electrolyte deposition technique. The authors achieved 17 times enhancement in the heat transfer coefficient (HTC), and attributed it to nanocavities and special vertical channels formed during the electrodeposition process. During this process the departing hydrogen bubbles sought the lowest resistance path, creating low impedance vapor escape channels. Nanocavities increased nucleation site density and the channels facilitated vapor transportation.

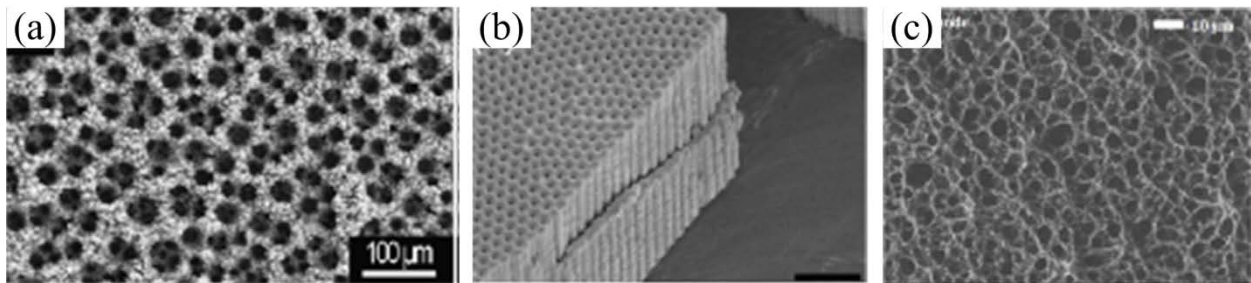


Figure 2 - 2 Sponge-like layers to enhance boiling in published literatures: (a)⁵⁸ (b)⁵⁹ (c)⁶⁰

Figure 2 - 2 (b) shows sponge-like structures fabricated by Zhang *et al.*⁵⁹ The researchers obtained this layer using electropolishing and anodizing techniques. The porous feature size can vary from a few nanometers to sub-millimeters, depending on anodizing voltage, temperature, and electrolytes. In this study the pore's diameter ranged from 100 nm to 500 nm. They obtained

2.3 times enhancement in HTC at low heat flux (2 – 4 W/cm²) and 1.75 times enhancement at high heat flux (4 – 10 W/cm²). The effect of CHF was not studied. The enhancement in HTC was explained by augmented surface area and increased nucleation site density.

Ahn *et al.*^{60,61} obtained sponge-like layers on SiO₂ substrate by boiling reduced graphene oxide colloid on SiO₂ surface, as shown in Figure 2 - 2 (c). The authors observed that the wall temperature increased very slowly after reaching CHF while normally it increased dramatically in boiling water. CHF of boiling water was enhanced 2 times on the surface after colloid boiling and they attributed the enhancement to the deposition of sponge-like layers during colloid boiling, which resulted in greatly enhanced thermal conductivity and vapor escape resistance.

Table 2 - 1 shows the summary of the research on boiling heat transfer enhancement by deposition of sponge-like layers.

Table 2 - 1 Boiling enhancement by sponge-like layers

	Substrate	Liquid	HTC Enhancement	CHF Enhancement
Li <i>et al.</i> ⁵⁸	Copper	R134a	17	N/A
Zhang <i>et al.</i> ⁵⁹	Alumina	Water	2.3 at low heat flux 1.75 at high heat flux	N/A
Ahn <i>et al.</i> ^{60,61}	SiO ₂	Water	N/A	2

2.1.4 Nanowires and Carbon Nanotubes (CNT)

A nanowire is a nanostructure in the form of wire with a diameter smaller than about 100 nm. A hollow nanowire, typically with a wall thickness on the order of molecular dimensions, is referred to as nanotube. Following the discovery of carbon nanotubes by Iijima in 1991,

researchers saw its potential in improving surface wettability and enhancement of heat transfer in pool boiling. In 2006, Ahn *et al.*^{62,63} fabricated multiwall carbon nanotubes (MWCNT) on silicon substrates using chemical vapor deposition (CVD). The diameters of the tubes varied from 8 to 16 nm, and the pitch was from 8 to 16 nm. Figure 2 - 3 (a) shows the side view image of the MWCNT. The heights of MWCNT were 9 μm (type A) and 25 μm (type B). The experimental results showed that CHF was enhanced by 25-28% for both type A and B, but for film boiling regime, 25 μm height MWCNT yielded 57% higher heat flux at Leidenfrost point, while no improvement was observed for 9 μm height MWCNT. The authors further explained this was because the minimum vapor film thickness in film boiling is 10 – 15 μm as predicted by numerical models. Thus there was no difference between flat surface and 9 μm height MWCNT surface in film boiling. Although a critical height for enhancement was observed in film boiling regime, both heights performed similarly in the nucleate boiling region and CHF was not affected by MWCNT height, which was also confirmed by Lu *et al.*'s observation in 2011.⁶⁴

In 2007, Ujereh *et al.*⁶⁵ coated silicon and copper substrates with nanotubes with different CNT array densities and area coverage on silicon and copper surfaces. The MWCNTs were approximately 50 nm in diameter and 20-30 μm in height. Figure 2 - 3 (b) shows a lightly (30 CNTs/ μm^2) coated CNT array. In all cases, the onset superheat of boiling was reduced and heat transfer coefficients were improved. CHF was increased by 44.8% for densely coated silicon and 6.0% for copper substrate compared to flat surfaces; this difference was due to the fact that flat silicon surface is very smooth and has very few nucleation sites. The enhancement mechanism was attributed to the addition of nucleation cavities offered by the abundance of zero cone angles and 'reservoir-type' cavities. Although the higher CNT mesh density reduced wall superheat slightly at incipience, it also decreased CHF because of the reduced effective surface area.

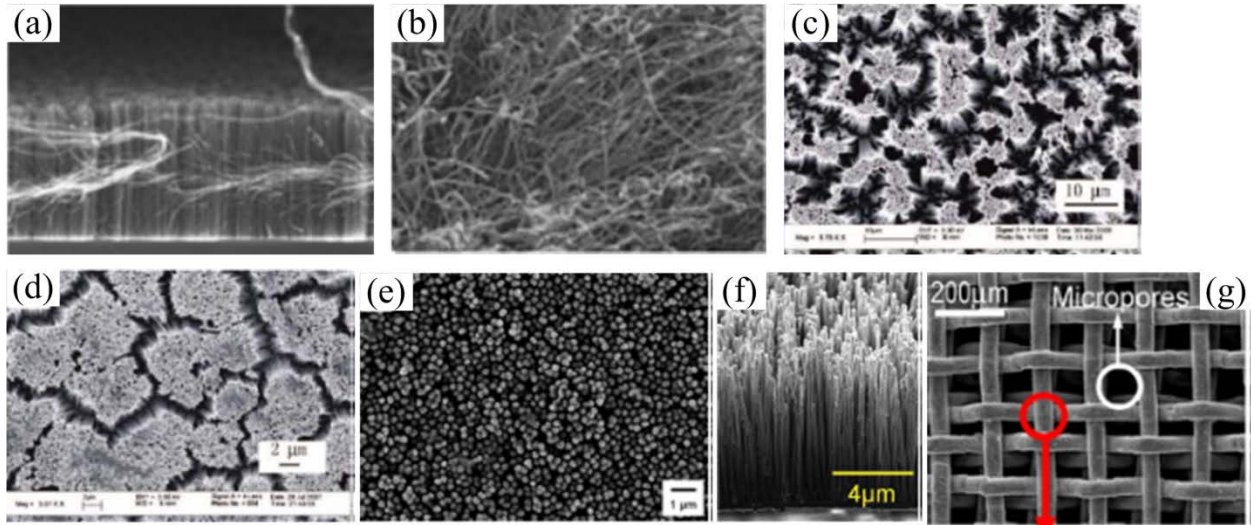


Figure 2 - 3 Nanowires and CNTs in literatures: (a)⁶² (b)⁶⁵ (c)⁶⁶ (d)⁶⁶ (e)⁶⁷ (f)⁶⁸ (g)⁶⁹

In 2009, Chen *et al.*⁶⁶ published the first paper on the effect of nanowires on pool boiling. In this case, silicon nanowires were synthesized by immersing a silicon wafer into an aqueous solution of AgNO_3 and HF acid. As shown in Figure 2 - 3 (c), the silicon nanowires were vertically aligned with the diameter in the range of 20-300 nm, and the height in the range of 40-50 μm . The copper nanowires were then synthesized by electroplating copper into nanoscale pores of commercially available porous alumina membranes. Figure 2 - 3 (d) shows that the resulting copper nanowires were approximately 200 nm in diameter and 40-50 μm in height with 50% filling ratio. Compared to the flat silicon surface, more than 100% improvements were obtained both in CHF and heat transfer coefficient. The enhancement of heat transfer coefficient was attributed to higher nucleation site density, and the enhancement of CHF was explained by the capillary pump effect of nanowires. Due to capillary force, the spacing between nanowires worked as capillary tubes pumping the water to interface, resulting in a capillary limited enhanced CHF. Lu *et al.*⁶⁴ further investigated the effect of nanowire height (ranging from 16 to 122 μm) and heater size on CHF. The results showed that the height of the nanowires did not affect CHF, but once the heater length was approximately smaller than eight times the capillary

length, the heater size effect caused by confined Helmholtz wavelength appeared. CHF increased with decreasing heater size. However, Yao *et al.*^{67,70} noted a linear dependence between the nanowire height and CHF. In their experiment, the height of nanowires varied from 2 to 20 μm for copper nanowires, and for silicon nanowires, two heights of 20 and 35 μm were examined. Different from the above two observations, Im *et al.*⁶⁸ found that for pool boiling of PF-5060, compared to flat surface, those samples with copper nanowire height of 1, 2, and 4 μm , the CHF was improved by 55% – 64%, but for 8 μm height nanowires, the enhancement was only 18%.

Table 2 - 2 shows the summary of HTC and CHF enhancement achieved by nanowires/nanotubes in the literature.

Table 2 - 2 Boiling enhancement by nanowires and CNTs

	Substrate	Liquid	HTC Enhancement	CHF Enhancement
Ahn <i>et al.</i> ^{62,63}	Silicon	PF-5060	N/A	1.25
Ujereh <i>et al.</i> ⁶⁵	Silicon	Water	5.5	1.4
	Copper		2	1.8
Chen <i>et al.</i> ⁶⁶	Silicon	Water	2	~2
Lu <i>et al.</i> ⁶⁴	Silicon	Water	N/A	~2
Yao <i>et al.</i> ⁶⁷	Copper	Water	N/A	~1.3
Yao <i>et al.</i> ⁷⁰	Silicon	Water	N/A	~2
Im <i>et al.</i> ⁶⁸	Silicon	PF-5060	N/A	~1.7
McHale <i>et al.</i> ⁷¹	Copper	HFE-7300	N/A	1.5
Dai <i>et al.</i> ⁶⁹	Copper	Water	1.5	1.6

2.1.5 Nanorods and Nanoparticles

A porous layer formed by metallic particles can be deposited using plasma and flame spraying techniques.^{72,73} Hsieh *et al.*⁷² achieved 1.5 – 2.6 times enhancement in HTC by coating Cu, Mo, Al, and Zn particles on heater rods with a 1 – 5 μm average pore diameter. As shown in Figure 2 - 4 (a), Chang *et al.*^{74,75} coated diamond particles with diameter varying from 2 μm to 70 μm using the DOA coating technique (D: diamond particles, O: Omegabond 101 epoxy, A: alcohol). Compared to reference surface, the authors obtained ~2 times enhancement in CHF.

Liter *et al.*⁷⁶ and Hwang *et al.*⁷⁷ coated spherical copper particles of 200 μm diameter on copper surfaces using the dry-phase diffusion sintering technique. The authors reported that the coating of modulated copper particles (Figure 2 - 4 (b) and (c)) could control the wavelength of Kelvin-Helmholtz instability and in turn, enhance CHF of boiling. Additionally, the other independent enhancement mechanism was that the space between these particles served as capillary pump, supplying more liquid to interface to evaporate. Roughly, 3 times and 1.8 times enhancement in CHF were obtained respectively.

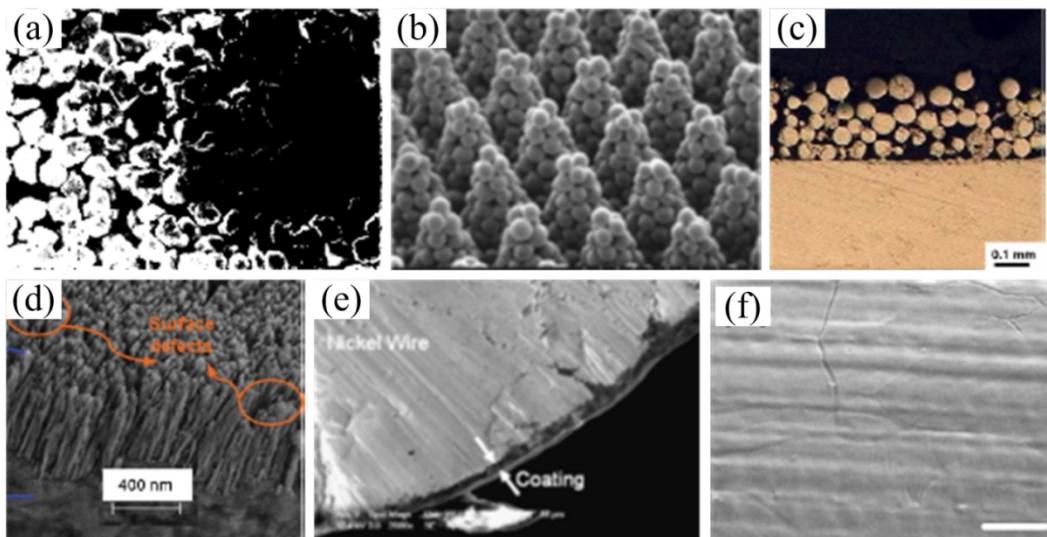


Figure 2 - 4 Nanorods and nanoparticles in the literatures: (a)⁷⁵ (b)⁷⁶ (c)⁷⁷ (d)⁷⁸ (e)⁷⁹ (f)⁸⁰

Li *et al.*⁷⁸ deposited Cu nanorods on a polished Cu substrate using an electron-beam evaporator for oblique-angle deposition. As shown in Figure 2 - 4 (d), the rods grew inclined at an angle of 60° if the substrate was tilted at a large angle (>85°). Although CHF was only enhanced by ~10%, HTC was improved by 63%. The enhancement was mostly attributed to the 30 times increased nucleation site density, as well as small departure bubble sizes and frequency.

Besides increased nucleation site density, improved wettability is another widely attributed enhancement mechanism.⁷⁹⁻⁸² With plasma-enhanced chemical vapor deposition (PECVD) and metal-organic chemical vapor deposition (MOCVD), Phan *et al.*⁸¹ controlled surface wettability by coating SiO_x, Pt, Fe₂O₃, SiOC, and Teflon particles on stainless steel substrate and conducted boiling experiments. The authors found that the improved wettability increased the bubble departure diameter and reduced the bubble departure frequency simultaneously. However, with an increased drop contact angle, HTC decreased initially and then increased. The lowest HTC was at 40° – 50° with respect to heat flux. Different from HTC, CHF firstly increased and then decreased with an increased drop contact angle. It reached its highest value at contact angle of ~18° according to Hendricks's observation.⁸² Forrest *et al.*⁷⁹ conducted an investigation of the boiling enhancement using the layer-by-layer (LBL) technique (Figure 2 - 4 (e)) to deposit polymer/SiO₂ nanoparticle multilayers on Ni wire. They achieved 2 times enhancement in both HTC and CHF. Feng *et al.*⁸⁰ fabricated Pt wires coated with alumina nano coatings by atomic layer deposition (ALD), as shown in Figure 2 - 4 (f). Compared to bare surface, the drop contact angle decreased from 68° to 0° with 20 nm thick deposited Al₂O₃ layer, resulting in 2 times CHF enhancement.

Table 2 - 3 summarizes the achievement in boiling heat transfer enhancement by nanorods and nanoparticles in the literature.

Table 2 - 3 Boiling enhancement by nanorods and nanoparticles

	Substrate	Liquid	HTC Enhancement	CHF Enhancement
Hsieh <i>et al.</i> ⁷²	Copper	R-134a	2.6	N/A
		R-407c	2.5	
Chang <i>et al.</i> ^{74,75}	Copper	FC-72	N/A	2
Liter <i>et al.</i> ⁷⁶	Copper	Pentane	N/A	3
Hwang <i>et al.</i> ⁷⁷	Copper	Pentane	N/A	1.8
Li <i>et al.</i> ⁷⁸	Copper	Water	1.6	1.1
Hendricks <i>et al.</i> ⁸²	Aluminum	Water	N/A	3.6
Forrest <i>et al.</i> ⁷⁹	Nickel	Water	~2	~2
Feng <i>et al.</i> ⁸⁰	Platinum	Water	~1	~2

2.2 Regular Structures

2.2.1 Fins, Pillars and Cavities

The fabrication of regular geometries such as fins, pillars, and cavities has also been done in literature. In 2002, Guglielmini *et al.*⁸³ conducted boiling experiments on a millimeter scale square-fin-structured surface, as shown in Figure 2 - 5 (a). Fins were 3 or 6 mm long and 0.4 to 1.0 mm wide. The researchers found that before reaching CHF, with an increased heat flux, HTC increased first and then decreased. For the surface with fins with a height of 3 mm, width of 1 mm and pitch of 2 – 4 mm, the peak value of HTC occurred in the heat flux range 2.5 – 5 W/cm². The peak value is about twice as high as the value at heat flux in the range of 5.5 – 10 W/cm². Rainey *et al.*⁸⁴ achieved 4.1 times enhancement in CHF with 8 mm high fins. ~4.3 times Enhancement was obtained under lower pressure at 60 kPa. Honda *et al.*^{85,86} investigated the

effect of square-fins in a micrometer scale ($50 \times 50 \times 60 \mu\text{m}^3$, width \times pitch \times height) on boiling. The authors observed ~ 2 times enhancement in CHF with these fins and obtained $\sim 11\%$ more enhancement with 32.4 nm high roughness. Wei *et al.*⁸⁷ further investigated the effect of fin geometry on heat transfer enhancement. The authors fabricated fins with width varying from 30 to 50 μm and height varying from 60 to 270 μm . The pitch was twice the fin width. They achieved ~ 2 times CHF enhancement for saturated liquid and ~ 4 times for 45 K subcooled liquid temperature with fins of 50 μm wide and 270 μm high.

Mori *et al.*⁸⁸ used a commercial honeycomb porous plate (Figure 2 - 5 (d)) achieving 2.5 times and 1.7 times enhancement in CHF and HTC respectively. The authors attributed the enhancement to increased liquid supply due to capillary pumping, and a reduction of the flow resistance for vapor escape due to the separation of liquid and vapor flow paths.

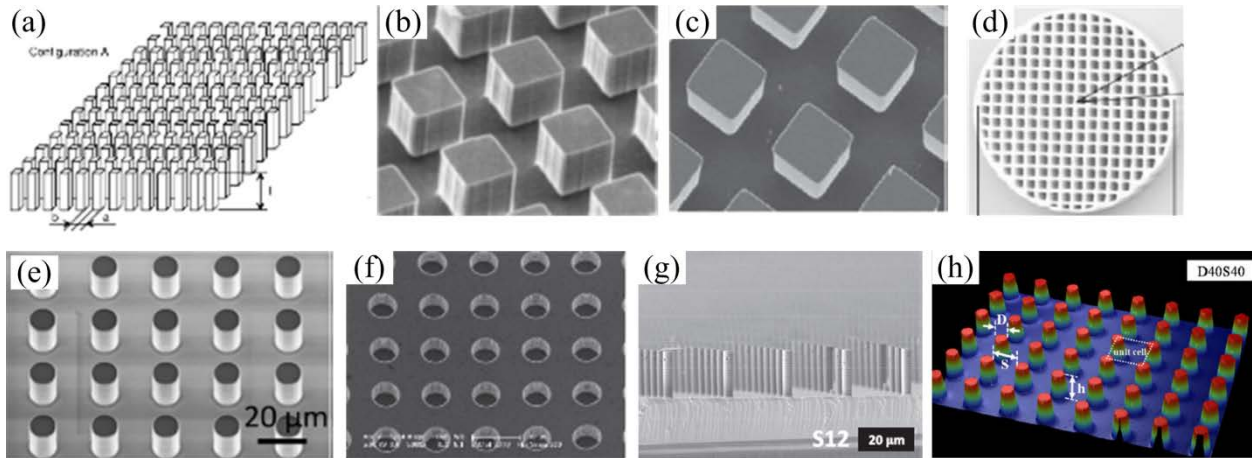


Figure 2 - 5 Fins, pillars, and cavities in the literatures: (a)⁸³ (b)⁸⁵ (c)⁸⁷ (d)⁸⁸ (e)³⁷ (f)⁸⁹ (g)⁹⁰ (h)⁹¹

Chu *et al.*³⁷ studied pool boiling on the silicon surface with micropillars. The heights of the pillars were 10 and 20 μm , the diameters were 5 and 10 μm , and the spacing varied from 5 to 15 μm , resulting in roughness variation between 1.79 and 5.94. Figure 2 - 5 (e) shows the surface with pillars of 10 μm in height, 10 μm in diameter and 15 μm in spacing. A maximum CHF of

about $200\text{W}/\text{cm}^2$ was obtained based on the projected area. Similar CHF values were observed with different pillar heights. The authors attributed the enhancement to elongated contact line length. More recently, Dong *et al.*⁸⁹ attained 1.4 times and 2.6 times enhancement in CHF and HTC of boiling ethanol respectively by fabricating micro cavities, as shown in Figure 2 - 5 (f). The authors attributed the enhancement to increased nucleate site density, reduced bubble departure diameter, and increased bubble departure frequency.

Kim *et al.*⁹⁰ formed pillars with several length scales (5 – 40 μm) on Si wafer by DRIE, which resulted in surface roughness ranging from 1 to 4.4, as shown in Figure 2 - 5 (g). The researchers achieved 3.5-fold and 3-fold enhancement in CHF and HTC respectively. They found a critical gap existed between pillars. A smaller gap size (10 – 20 μm) improved the capillary wicking rate due to larger capillary pressure and an increased liquid inflow rate. However, the permeable liquid inflow was reduced due to narrow gaps, jeopardizing rewetting situations. With similar pillars (Figure 2 - 5 (h)), Kim *et al.*⁹¹ proposed a new CHF triggering mechanism to explain CHF enhancement of micro structured surfaces. They observed that a number of small bubbles were generated and then merged into a large bubble. CHF was governed by a large coalesced bubble departure frequency. The microstructures on the surface changed the evaporative mass flow rate, and thereby affected coalesced bubble departure frequency. However, the microstructures increased the liquid flow resistance, which is responsible for the deterioration of CHF for the surface with high roughness, and was observed in their experiments.

Table 2 - 4 shows the summarization of work has been done to enhance boiling heat transfer by micro-scale fins, pillars, and cavities in the literature.

Table 2 - 4 Boiling enhancement by fins, pillars, and cavities

	Substrate	Liquid	HTC Enhancement	CHF Enhancement
Rainey <i>et al.</i> ⁸⁴	Silicon Oxide	FC-72	N/A	4.1
Honda <i>et al.</i> ^{85,86}	Silicon	FC-72	N/A	2.2
Wei <i>et al.</i> ⁸⁷	Silicon	FC-72	N/A	4.2
Mori <i>et al.</i> ⁸⁸	Copper	Water	1.7	2.5
Chu <i>et al.</i> ³⁷	Silicon Dioxide	Water	N/A	2.6
Dong <i>et al.</i> ⁸⁹	Silicon	Ethanol	2.6	1.4
Kim <i>et al.</i> ⁹⁰	Silicon	Water	3	3.5
Kim <i>et al.</i> ⁹¹	Silicon Dioxide	Water	N/A	1.9

2.2.2 Channels/Ridges

Chien *et al.*⁹²⁻⁹⁴ obtained buried channels by soldering a 0.05 mm thick copper foil with 0.18 – 0.23 mm diameter holes on a test tube surface with channels with width of several hundred micrometers (Figure 2 - 6 (a)). The authors postulated that liquid meniscus formed at the corner of the buried channel affected the evaporation behavior in a single bubble and, in turn, the bubble departure diameter, frequency and nucleation site density. The changed bubble dynamics resulted in ~ 2.7 times enhancement in HTC of boiling methanol at the heat flux of 5.5 W/cm².

Ramaswamy *et al.*⁹⁵ investigated bubble dynamics on enhanced structures, as shown in Figure 2 - 6 (b). The structures have an array of rectangular channels cut on either side of the Si substrate and aligned at an angle of 90° to each other. These interconnected channels also created pores with a diameter in the range 0.12 – 0.20 mm and pitch in 0.7 – 1.4 mm. Although pore pitch sizes in this investigation did not affect bubble departure diameter (which depended on pore

diameter), it influenced the bubble coalescence phenomenon. Thereby the heat transfer enhancement can be controlled by different pore pitch sizes. With similar structures (Figure 2 - 6 (c)), Ghiu *et al.*⁹⁶ achieved ~5 times enhancement in CHF of boiling PF 5060.

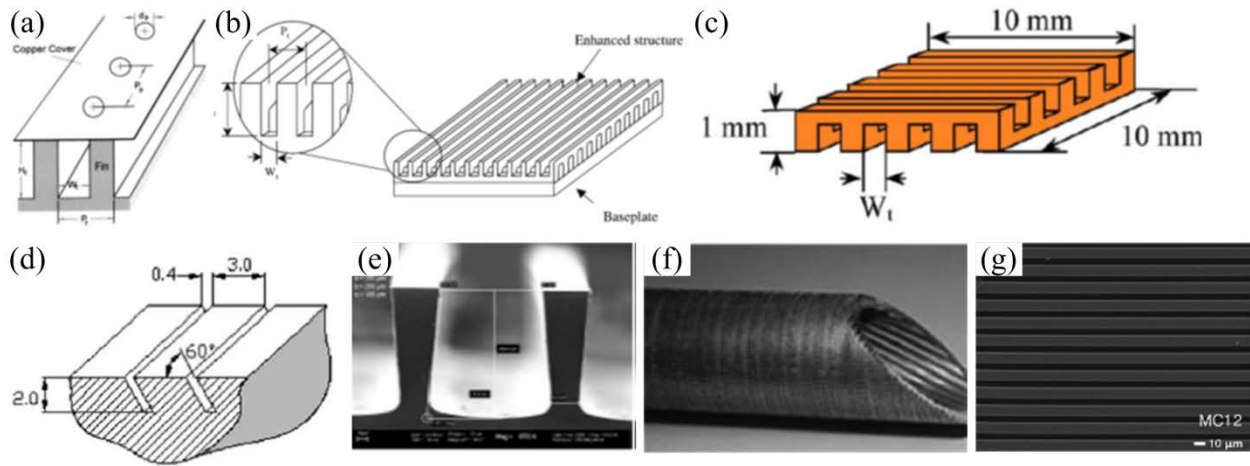


Figure 2 - 6 Channels and ridges in the literatures: (a)⁹³ (b)⁹⁵ (c)⁹⁶ (d)⁹⁷ (e)⁹⁸ (f)⁹⁹ (g)¹⁰⁰

Das *et al.*⁹⁷ fabricated grooves with varying shape and tilted angle on copper surfaces (Figure 2 - 6 (d)) using the wire-electro discharge machining technique. The authors achieved 3.4 times enhancement in HTC at a low heat flux (less than 25 W/cm²) of boiling water. They also found that more enhancement was attained with inclined channels compared to vertical channels.

Cooke *et al.*⁹⁸ investigated the role of channels with dimensions in a few hundred microns (Figure 2 - 6 (e)) in boiling heat transfer enhancements. CHF increased with the increase of channel depth. They achieved ~2.1 times CHF enhancement with 275 μm channels on Si surface. However, CHFs for all samples based on the wetting area were close to or less than that of the flat surface. It was found that the bubbles were formed at the bottom of the channel and then moved to the top of the fins where they attached and grew. The channels remained flooded and helped the liquid rewet the surface by offering pathways for it; due to this, dry out of the surface did not occur. They further reported a heat flux of 244 W/cm² without reaching CHF on Cu

surface, on which CHF was $\sim 125 \text{ W/cm}^2$.¹⁰¹ They attributed the enhancement to two aspects: a) the microchannels offered three sides for heating, and the liquid pushed away by the bubble growth was heated by the surface and channel walls; b) the cooler liquid at the bulk temperature was pulled into the channel after the bubble departed, and delayed the occurrence of CHF. With deeper channels, Kandlikar¹⁰² achieved 2.4 times enhancement in CHF and 8.4 times enhancement in HTC of boiling water on the copper surface. With open channels, other researchers also attained 6 – 10 times enhancement in HTC (Chen⁹⁹) and 1.5 times enhancement in CHF on SiO₂ surface (Kim *et al.*¹⁰⁰).

Table 2 - 5 summarizes the enhancement achieved by channels or ridges in literature.

Table 2 - 5 Boiling enhancement by channels and ridges

	Substrate	Liquid	HTC Enhancement	CHF Enhancement
Chien <i>et al.</i> ⁹²	Copper	Methanol	~ 2.7	N/A
Ghiu <i>et al.</i> ⁹⁶	Copper	PF 5060	N/A	~ 5
Das <i>et al.</i> ⁹⁷	Copper	Water	3.4	N/A
Cooke <i>et al.</i> ⁹⁸	Silicon	Water	N/A	2.1
Kandlikar ¹⁰²	Copper	Water	8.4	2.4
Chen ⁹⁹	Copper	Water	6 – 10	N/A
Kim <i>et al.</i> ¹⁰⁰	Silicon Oxide	Water	N/A	1.5

2.3 Hybrid Structures

Fabricating nanoscale structures, such as nanowires, CNTs, and nanorods, etc. on microscale structures, such as fins, channels, etc. is another way of surface modification to enhance boiling

heat transfer. Launay *et al.*¹⁰³ fabricated microscale fins using standard surface micromachining techniques and grew CNTs following Wei *et al.*'s process,¹⁰⁴ as shown in Figure 2 - 7 (a). It turned out that the combination of fins and CNTs deteriorated heat transfer. With fins only, the CHF was enhanced by 40%, while it remained similar to plain surface with CNT coated fins. With coated CNT only, the enhancement of CHF was not observed, either. The authors postulated that the changed nature of surface-fluid interactions, induced by CNT, caused this deterioration.

Kim *et al.*¹⁰⁵ formed microscale (M) nanoscale (N) and multiscale (NM) modified surfaces. M surface was obtained using wet etching of Si wafer with an tetramethyl ammonium hydroxide etchant, as shown in Figure 2 - 7 (b); N surface was covered by ZnO nanorods while NM used a combination of these two: nanorods covered microscale posts (Figure 2 - 7 (c)). The authors achieved 1.5, 1.8, and 2.1 times enhancement in CHF with M, N, and NM surface respectively; while HTC enhancement of 1.7 times was similar for these three types of surfaces. The enhancements were explained by the changes in the bubble nucleation behavior, augmentation in surface area, and the mechanism of bubble growth.

Yao *et al.*^{106,107} obtained silicon nanowires (SiNW) on the top, bottom, and side walls of channels, which were fabricated by using a deep reactive ion etching (DRIE) process, as shown in Figure 2 - 7 (d). The authors achieved 2.7 times enhancement in CHF and 4.1 times enhancement in HTC. Compared to channels without SiNW, the CHF enhancement was improved by 90%. Similarly, Jaikumar *et al.*¹⁰⁸ deposited nanoparticles with a mean size of 10 – 20 μm on channel-structured surfaces, followed by 800°C sinter for two hours to ensure substrate bonding. This fabrication yielded a pore size between 5 – 20 μm . Three types of surfaces were fabricated: sintered-throughout, sintered-fin-tops and sintered-channels. The researchers attained

a 2.4-fold enhancement in CHF and 6.5-fold enhancement in HTC. In these two studies, the researchers explained their enhancements with changed bubble dynamics induced by separated liquid vapor path.

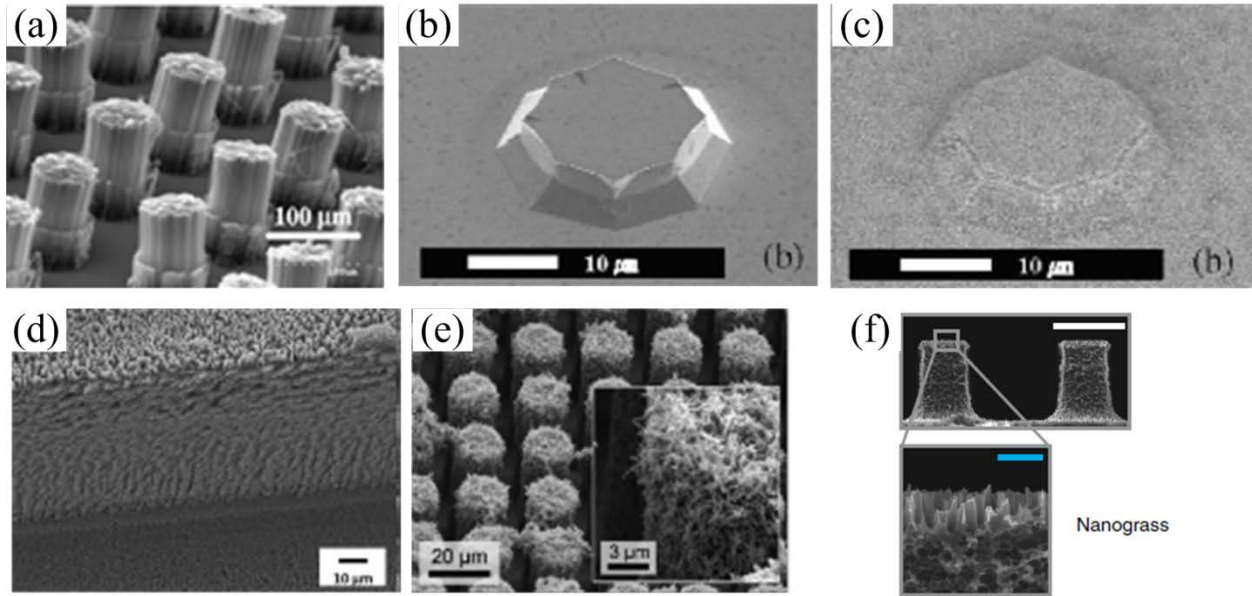


Figure 2 - 7 Hybrid structures in the literatures: (a)¹⁰³ (b)-(c)¹⁰⁵ (d) side wall of the channel¹⁰⁷ (d)¹⁰⁹ (f)¹¹⁰

In 2014, Rahman *et al.*¹⁰⁹ deposited tobacco mosaic virus (TMV) biotemplated (Figure 2 - 7 (e)) nanorods on Si surface fabricated with pillars and conducted boiling experiments of water. The authors achieved 3.4 times enhancement of CHF and they attributed the enhancement to the wicking effect: the space between structures works as a capillary pump to transport liquid to the evaporation interface.

Dhillon *et al.*¹¹⁰ fabricated nanograss on micropillars by DRIE on Si wafer, as shown in Figure 2 - 7 (f). The authors found that the dry spot heating timescale is of the same order as that of the dry spot rewetting timescale induced by gravity and liquid imbibition. This observation demonstrated that CHF could be enhanced if microstructures facilitated liquid to rewet the

heated surface. They observed gravity induced rewetting was dominant when gaps between pillars were larger than 200 μm . CHF increased with decreased gap sizes because the wicking effect came into the picture to facilitate liquid flow. Viscous pressure would overwhelm capillary pressure when pillar spacing went down to 10 – 20 μm and CHF enhancement was jeopardized.

Table 2 - 6 shows the summarization of the reported heat transfer enhancement by hybrid structures.

Table 2 - 6 Boiling enhancement by hybrid structures

	Substrate	Liquid	HTC Enhancement	CHF Enhancement
Launay <i>et al.</i> ¹⁰³	Silicon	PF-5060	~1	~1
Kim <i>et al.</i> ¹⁰⁵	Silicon	Water	1.7	2.1
Yao <i>et al.</i> ¹⁰⁷	Silicon	Water	4.1	2.7
Jaikumar <i>et al.</i> ¹⁰⁸	Copper	Water	6.5	2.4
Rahman <i>et al.</i> ¹⁰⁹	Silicon	Water	N/A	3.4
Dhillon <i>et al.</i> ¹¹⁰	Silicon	Water	N/A	1.8

2.4 Enhancement Mechanism

The CHF enhancements due to the presence of micro/nano structures have been widely attributed to the increased nucleation site density,^{69,70,78} improved wettability or wicking effect to facilitate liquid supply,^{66,90,91,100,109,111,112} providing separate pathways for liquid and vapor flow thus modifying bubble dynamics,^{98,101,102} and increased roughness.^{37,113}

2.4.1 Increased Nucleation Site Density

Eq. (1-1) dictates that with a certain superheat, the size of active nucleation site must be in a desired range so that the evaporation at the bottom part of the bubble dominates over the condensation at the upper part of the bubble. More specifically, at the superheat of 15 – 20°C, the range of active nucleation diameter is between ~1 μm and ~200 μm ,⁷⁸ which covers the size of most microscale structures, such as the pore diameter of the porous layer, the space between the particles, or nanorods, etc. A 30 – 40 fold increased nucleation site density was observed experimentally with a pore size in the order of 10 μm .^{69,78}

Boiling enhancement by increased nucleation site density is based on the fact that boiling is much more efficient than natural convection. During the boiling process, only a circular region with a diameter of twice the bubble departure diameter is affected by the boiling, while heat is transferred through natural convection in the surrounding region. Normally boiling heat flux represents the average heat flux through the whole surface, not only through the affected region. Thus, increasing the nucleation site density causes bubble formation to increase on the surface, thereby increasing the average heat flux on the whole surface.

2.4.2 Facilitated Liquid Supply

Both topological and chemical properties of the surfaces affect surface wettability. For the surfaces with hydrophilic structures, the contact angle decreases as the surface wettability is represented by Wenzel state.⁴ Many researchers observed that the drop contact angle decreased dramatically with micro/nano structures on the surface, or even reached 0°.^{66,100,109-111} Improved wettability decreases liquid viscous drag along its flow path, and thereby facilitates liquid flow to the heated region. The space between the structures, or the pores formed due to the structures, can provide a large capillary pumping force to bring liquid back to the heated surface. Chen *et*

*al.*⁶⁶ found agreement between their experimental results and the capillary limit model (Eq. (2-2)), which was proposed by Liter *et al.*⁷⁶ and was based on the balance between the capillary pumping force and the liquid viscous drag.

$$\frac{q_{CHF,c}''}{0.53(\rho_l \sigma h_{lv} / \mu_l) (K \phi_s)^{1/2} / D} = 1 - \frac{C_E}{0.53} \frac{D}{\sqrt{\phi_s}} \frac{q_{CHF,c}''^2}{\rho_l \sigma h_{lv}^2} \quad \text{Eq. (2-2)}$$

$$K = \frac{\phi_s d^2}{180(1-\phi_s)^2}, \quad C_E = \left(\frac{0.018}{\phi_s^3} \right)^{1/2}$$

In Eq. (2-2), it is difficult to identify porosity ϕ_s , liquid flow distance D , and characteristic length d . Rahman *et al.*¹⁰⁹ introduced a dimensionless wicking number Wi , which can be determined by experiments to account for the wicking effect on CHF. Wi represents the ratio of the liquid mass flux wicked into the heated surface to the critical mass flux of vapor leaving the surface, which is calculated by classical hydrodynamic instability analysis,⁶ as shown in Eq. (2-3). The CHF limited by wicking effect can be predicted by Eq. (2-4), in which $q_{CHF,Z}''$ is Eq. (1-15).

$$Wi = \frac{\rho_l \dot{V}_0''}{\rho_v^{1/2} [\sigma g (\rho_l - \rho_v)]^{1/4}} \quad \text{Eq. (2-3)}$$

where $\dot{V}_0'' = \left(\frac{D_C}{D_W} \right)^2 \left(\frac{dH}{dt} \right)_{t=0}$, in which D_C is the diameter of the capillary tube used to test wicking effect of the surface, and D_W is the diameter of the wetting area on the surface.

$$q_{CHF,W}'' = (1 + Wi) \cdot q_{CHF,Z}'' \quad \text{Eq. (2-4)}$$

Boiling enhancement by facilitated liquid supply is based on the idea that the CHF occurs when the liquid is not able to rewet the surface at the same rate as the generation of vapor. Improved wettability and the space between structures enable liquid flow by reducing drag and increasing capillary forces respectively. However, recent work^{90,91,110} shows that if the space between

structures is smaller than 10 – 20 μm, the flow resistance increases and jeopardizes rewetting, which is responsible for the deterioration of CHF.

2.4.3 Separated Liquid/Vapor Pathways

Another proposed CHF enhancement mechanism is to control bubble motion by using evaporation momentum force. The changed bubble dynamics increases microconvection heat transfer and provides separate pathways for liquid and vapor flow. Evaporation at the liquid-vapor interface of the bubble results in a force pulling the interface and contact line into the liquid. The bubble grows because this force exceeds the retaining force due to surface tension, and thus the bubble base expands in all directions due to symmetry, as shown in Figure 2 - 8 (a), in which the evaporation momentum forces act in the x-direction on its two sides. The momentum force F_m per unit length over a bubble height H_b can be given by Eq. (2-5).

$$F_m = \frac{q_l \times H_b \cdot 1}{h_{lv}} \times \frac{q_l \times H_b \cdot 1}{h_{lv}} \cdot \frac{1}{\rho_v} \cdot \frac{1}{H_b \cdot 1} \quad \text{Eq. (2-5)}$$

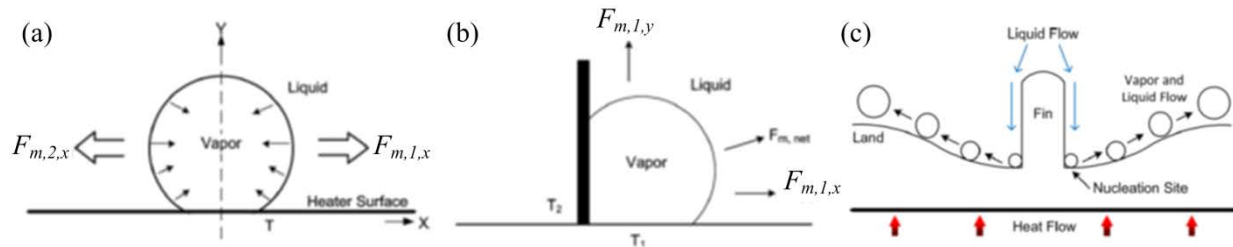


Figure 2 - 8 Evaporation momentum forces acting on a growing bubble (a) on plain surface (b) at the corner of the fin base and resulted separated liquid vapor flow pathways¹⁰²

Figure 2 - 8 (b) shows how a bubble forms and grows at the corner of the channel or fin base.

Force $F_{m,2,x}$ is absent due to the presence of the fin on the left side. The bubble trajectory is determined by the resultant of $F_{m,l,x}$ and $F_{m,l,y}$. The trajectory is designed to be 14.1° to the horizontal line based on an assumption that a 50% lower evaporation rate from the top interface causes $F_{m,l,y}$ to be one-fourth of $F_{m,l,x}$. Thus, the bubble follows a path away from the fin surface

sweeping over the heated surface as depicted in Figure 2 - 8 (c). Bubble motion induces bulk liquid to flow over the fins toward nucleation site. In this way, the liquid and vapor flow pathways are separated, avoiding blocking the liquid pathway due to the escape of the vapor. This modified bubble motion due to fins/channels was observed experimentally in the literature.^{98,101,102}

2.4.4 Increased Roughness

Boiling enhancement by increased roughness can be explained from three aspects: increased nucleation site density, increased liquid-solid contact area and the elongated contact line. Along with the roughness introduced by structures, there exist many cavities, holes, or bumps on the roughened surface. All of these formed structures provide more active nucleation sites to trigger boiling to occur at these locations. Also, compared to a plain surface, the fabricated structures enlarge solid surface area, and in turn increase solid-liquid contact area. Without considering the increased nucleation site density induced by roughness, the average heat flux maintains while the heat transfer area was enlarged. Heat flux is found to be improved if we use the projected area to calculate it.

In the contact line model (section 1.3.4), most heat transfer occurs through a triple phase contact line. Increased roughness elongates the contact line, which means the heat transfer is also enhanced. Based on this idea, Chu *et al.*³⁷ modified Kandlikar's model (Eq. (1-23)) to predict CHF on pillar-structured surface as Eq. (1-24).

2.4.5 Summary

Mechanisms behind boiling enhancements due to micro/nano structures are complicated. The mechanisms mentioned above are not independent most of the time. Two or more of them are

usually coupled to dominate the enhancement. Chen *et al.*¹¹⁴ found that even the fabrication process also affected working limits of boiling. The capillary limits of samples fabricated by milling are obviously larger than those fabricated by chemical etching. Thus, further investigation on enhancement mechanisms is necessary.

3. Critical Height of Micro/Nano Structures to Enhance CHF

3.1 Hypothesis

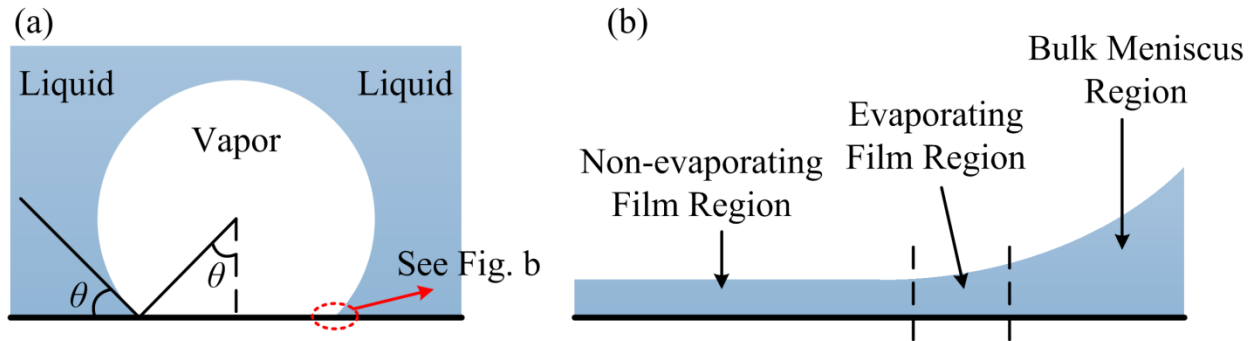


Figure 3 - 1 Schematic of the bubble base depicting the microlayer and its three regions

Microlayer evaporation is one of the most important heat transfer mechanisms of boiling. The microlayer is the thin liquid film underneath the bubble. As shown in Figure 3 - 1, it is widely accepted that the base of the bubble can be divided into three regions: the non-evaporating film region, the evaporating film region, and the bulk meniscus. Microlayer evaporation has been observed in experiments by many researchers.^{17,18,20-23} Figure 3 - 2 shows the typical microlayer profile underneath the bubble (blue dots) with a constant average heat flux. Compared to the outer region and center dryout region, the local heat flux is doubled and the local temperature is $\sim 5^{\circ}\text{C}$ lower in the microlayer region due to evaporation. With constant wall temperature, Chen *et al.*¹⁴ found that the heat flux decreased significantly during bubble growth due to the presence of a dry spot. Furthermore, Maroo *et al.*¹¹⁵⁻¹¹⁷ obtained a non-evaporating film in simulations of thin film evaporation due to the attraction between solid and liquid molecules. Although the pressure in this film can be reduced or even negative, no cavitation occurs because the film thickness is smaller than the critical cavitation radius. The authors further found that the film could be

ruptured and evaporated by the presence of nanoscale ridges, which increases heat flux from 350 MW/m² (smooth surface) to 600 MW/m² (ridge-structured surface).¹¹⁸

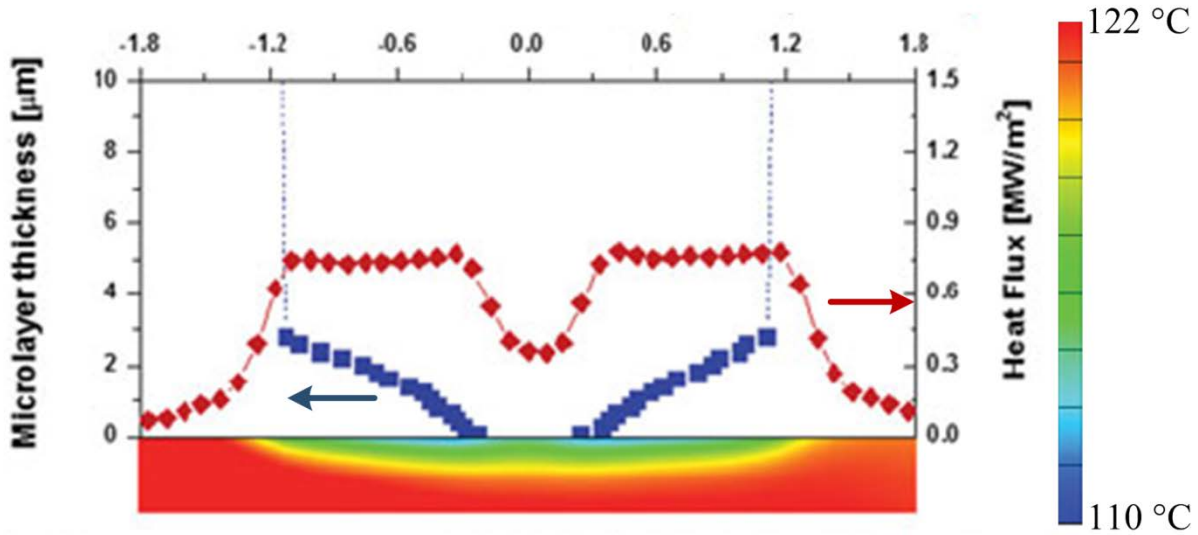


Figure 3 - 2 Distribution of local temperature and heat flux in microlayer region²³

Based on this knowledge, this chapter proposes the hypothesis that boiling heat transfer enhancement could be obtained by rupturing and evaporating the thin film underneath the bubble by using ridge-based geometry. Figure 3 - 3 shows a bubble on a ridge-structured surface. If the ridge height is larger than the local film thickness, the film is disconnected from bulk liquid and is broken to independent water slabs between the ridges. To evaporate the film, the input energy must overcome two energy barriers: liquid-liquid molecular attraction and solid-liquid attraction. Compared to the complete film on a flat surface, an extra solid-liquid interface is created by the side wall of ridges to replace the original liquid-liquid contact, and makes the water slabs evaporate as the solid-liquid attraction is weaker than the liquid-liquid attraction (demonstrated by the non-zero contact of a drop of water on SiO₂ surface). The evaporation of the thin film facilitates bubble growth, and thereby increases bubble departure frequency and boiling heat flux. However, if the ridge height is smaller than the thin film thickness, the film maintained

intact on the surface and is connected to the bulk liquid, similar to that on the plain surface. In this case, the film is not ruptured and the additional evaporation does not occur. Thus no enhancement is expected when the ridge height is smaller than the film thickness.

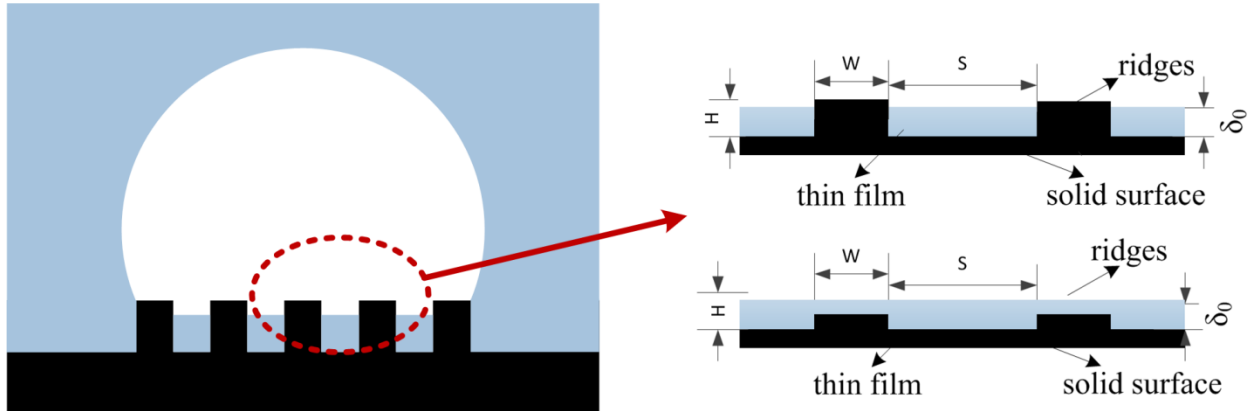


Figure 3 - 3 Hypothesis of thin film rupture and evaporation underneath the bubble on ridge-structured surface for pool boiling heat transfer enhancement

3.2 Experimental Methods

3.2.1 Sample Fabrication

Based on the hypothesis mentioned above, various samples with ridges were designed and fabricated. Figure 3 - 4 shows the sample design. It consists of ridges on the top and the heater on the bottom. The sample is diced into $2\text{ cm} \times 2\text{ cm}$ square. The ridges are obtained by etching a Si wafer. The heater is made of indium tin oxide (ITO), which is deposited on the whole back side of the wafer. The Cu layer ($1.25\text{ cm} \times 0.625\text{ cm} \times 500\text{ nm}$) is patterned and used as electrodes for connecting the ITO to electrical wires. The heating area is the region between two Cu electrodes, which is $1.25\text{ cm} \times 0.75\text{ cm}$. With a direct current (DC) power supply of $150\text{ V} \times 5\text{ A}$, a heat flux as high as 375 W/cm^2 can be obtained.

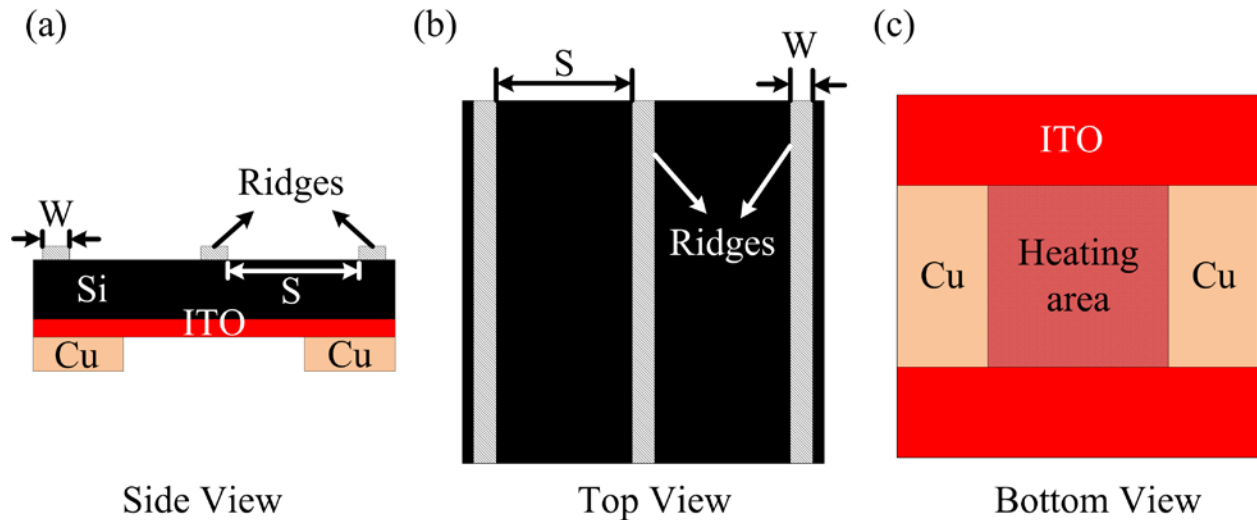


Figure 3 - 4 Sample design (a) side view (b) top view (c) bottom view (sizes are not scaled)

The ridges were fabricated on the Si wafer. Figure 3 - 5 shows the fabrication procedure. It consists of photolithography, plasma etching, thermal growth of the oxidation layer, and film (ITO and Cu) deposition.

(a) *Wafer Cleaning.* Before fabrication, the wafers were cleaned to make sure there was no dust or other contamination left on the wafer. The wafers were cleaned in a hot bath of Remover 1165 in two tanks, 10 minutes for each tank. The wafers were then washed in a DI water tank to remove any chemical residue. After that, the wafers were further cleaned in Glen 1000 oxygen plasma at a power of 400 W for 5 minutes to remove any possible polymer residue. After the oxygen plasma cleaning, the water drop contact angle was 0° and recovered to between 30° and 40° in ~ 3 hours.

(b) *Photoresist Deposition.* A 60 nm thick layer of AR3 was used as anti-reflectant, and the photoresist was a 410 nm thick layer of UV210. After photoresist deposition, soft bake was done at 135°C for 60 seconds.

(c) *Exposure*. In order to expose the photoresist to laser and get the patterns, ASML 300 was chosen as the stepper. The energy-controlled mode was used; the optimum energy was 12.5 mJ/cm² and optimum focus was 0 μm. After the exposure, the exposed wafers were hard baked at 135 °C for 90 seconds.

(d) *Development*. To develop the patterns, the wafer was immersed in the solution of 760 MIF for 30 seconds and washed with DI water to remove chemical residue.

(e) *Plasma Etching*. After development, the wafers were etched to get ridges. Unaxis 770 deep silicon etcher was used; the etching rate was 100 nm per minute.

(f) *Removal of Photoresist*. To remove the remaining photoresist, step (a) was repeated and Si ridges were obtained by this step.

(g) *Thermal Growth of SiO₂ layer*. In order to obtain SiO₂ ridges, a 125 nm thick oxidation layer was thermally grown on Si ridges in a wet/dry oxide furnace at 900 °C for an hour. For the fabrication of Si ridges, this step was skipped.

(h) *ITO deposition*. PVD 75 sputter was used for ITO deposition. The operation temperature was set as 200 °C and the oxygen concentration was 2%, by which the resistance of the heater was about 15 Ω with thickness of 90 nm.

(i) *Cu deposition*. The CVC sputter was used for Cu deposition. The deposition rate was about 33 nm per minute. The deposition was processed for 15 minutes to get ~500 nm thick Cu electrodes.

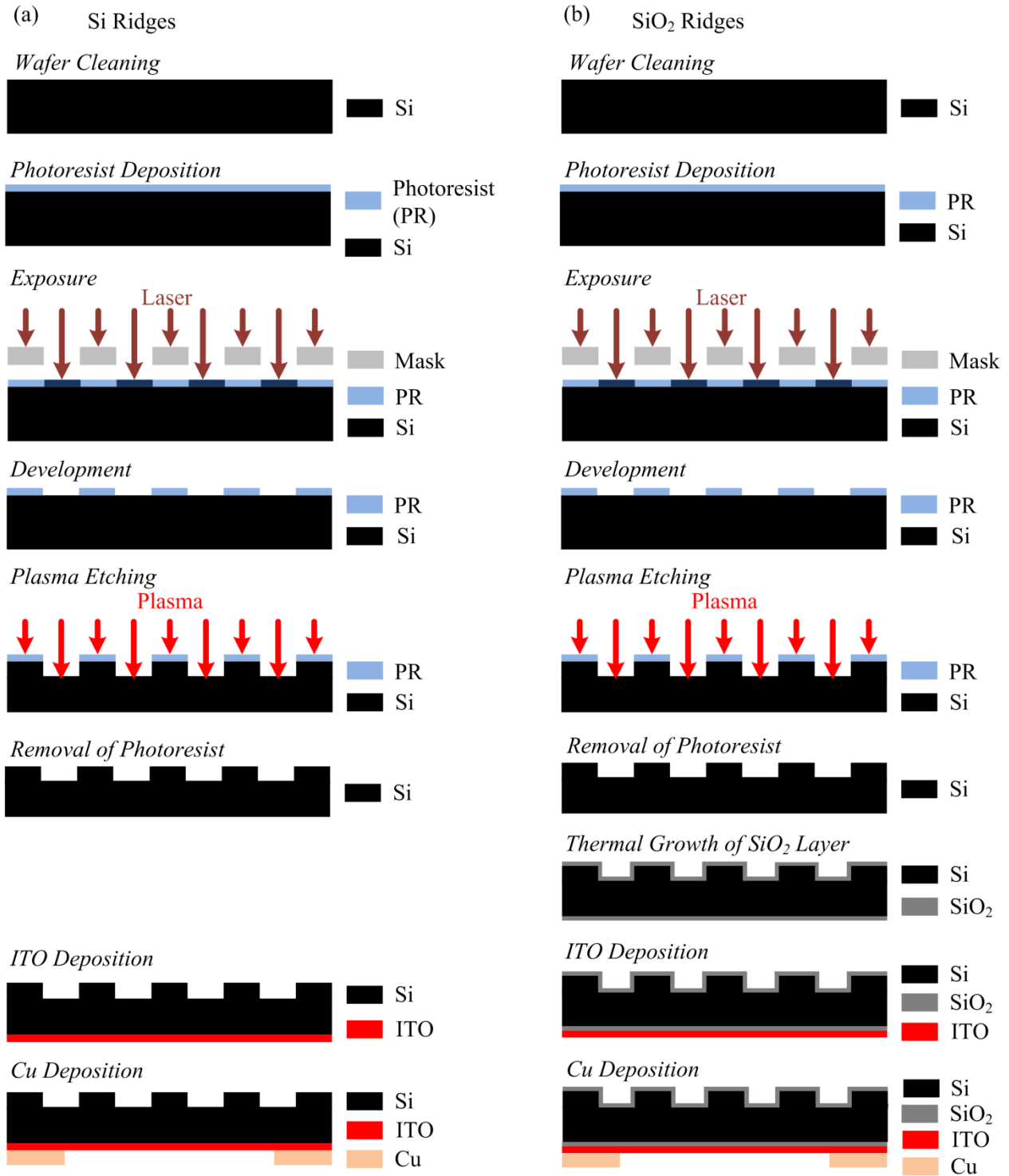


Figure 3 - 5 Fabrication procedure of Si and SiO₂ ridges (not scaled)

Following the procedure mentioned above, Si and SiO₂ ridges were fabricated with varying heights from ~300 nm to 1.5 μm. The ridge space was ~5 μm and ridge width was ~500nm

(Figure 3 - 6). The resulting roughness was from 1.11 to 1.55. The roughness of each sample was calculated as the ratio of wetted surface area (sum of projected area and additional surface area due to the ridges) to the projected area (Eq. (3-1)). Table 3 - 1 summarizes ridge geometries fabricated to investigate the effect of height on CHF enhancement.

$$r = 1 + \frac{2H}{S+W} \quad \text{Eq. (3-1)}$$

Table 3 - 1 Geometry of fabricated ridges

Sample	Height H (nm)	Width W (nm)	Spacing S (μm)	Roughness r
Si #1	300	520	4.95	1.11
Si #2	585	460	5.00	1.21
Si #3	610	745	7.50	1.15
Si #4	1270	460	5.00	1.46
SiO ₂ #1	585	595	4.90	1.21
SiO ₂ #2	665	660	4.80	1.24
SiO ₂ #3	1060	595	4.90	1.39
SiO ₂ #4	1530	555	5.00	1.55

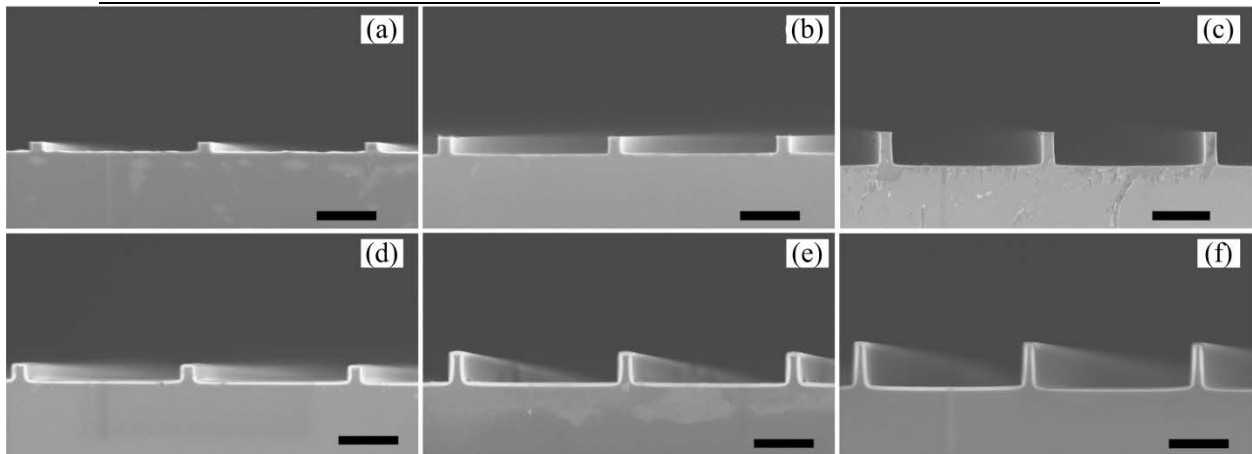
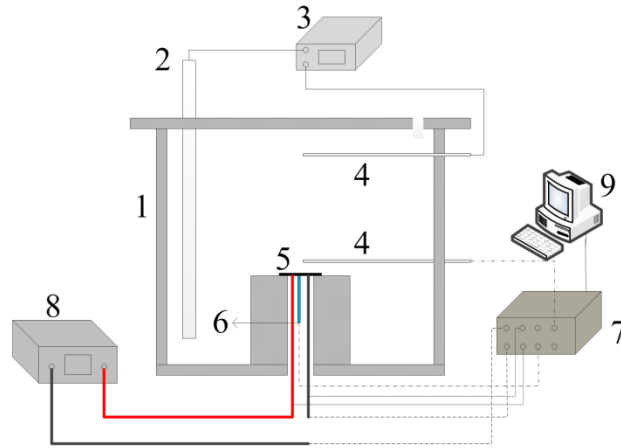


Figure 3 - 6 SEM images of side view of Si ridges with height (a) 300 nm, (b) 585 nm, and (c) 1.27 μm ; SiO₂ ridges with height (d) 585 nm, (e) 1.06 μm , and (f) 1.53 μm

3.2.2 Boiling Rig and Experiment Procedure

Figure 3 - 7 shows the schematic of the pool boiling setup. The setup consists of a liquid chamber, sample holder, bulk liquid heating loop, sample heating loop, and data acquisition. The chamber and sample holder are made of half-inch thick polycarbonate. A 1 cm diameter hole was drilled through the lid of the chamber to maintain the pressure as atmospheric pressure. The bulk liquid heating loop includes an immersion heater, a proportional-integral-derivative (PID) controller and a resistance temperature detector (RTD). With appropriate setting of PID controller, this loop maintains the bulk liquid at the saturation temperature (97~100°C). Sample heating loop includes a DC power supply, voltage and current measurement, and sample temperature measurement. The wires connecting the sample and power supply were soldered onto the Cu electrode and buried in epoxy, which was used to glue the sample on its holder. The epoxy was cured into a cylinder with diameter of 1.25 cm and thickness of 1.25 cm. The epoxy was also used as a thermal insulator as its thermal conductivity is ~1.2 W/m·K. The sample temperature was measured by a T-type thermocouple, which was also buried in the epoxy. The data acquisition included Keithley digital multimeter to record voltage and National Instruments (NI) modules to record current, liquid temperature, and sample temperature.



1 chamber; 2 immersion heater; 3 PID controller;
 4 RTD; 5 sample; 6 thermocouple; 7 DAQ; 8
 power supply; 9 PC

Figure 3 - 7 Boiling rig setup

The sample was cleaned by oxygen plasma immediately after fabrication. Before running experiments, it was cleaned again to make sure no contamination was left which can potentially affect its boiling performance. The sample was first wiped using cleanroom swab wetted with acetone, followed by an immersion in isopropanol and ethanol for 5 minutes respectively; finally, the sample was cleaned by ultrasonic cleaner for 3 minutes and dried by air.

Before heating up the sample to achieve boiling, the deionized (DI) water was degassed by boiling it for one hour and then maintained at saturation temperature. The boiling curve was obtained by incremental increase in the power supplied to the sample. The data were recorded after reaching the steady state, which was determined when the heater temperature change measured by the thermocouple was less than 0.5°C in a one minute period. Typically, the steady state was reached around ten minutes after increasing the power. CHF was identified when an incremental increase in the power supplied resulted in a sudden and dramatic increase of the sample temperature.

3.2.3 Uncertainty Analysis

The analysis of experimental uncertainty is based on propagation of uncertainties.¹¹⁹ From the experimental data, the general formula for heat flux calculation is Eq. (3-2). The uncertainty analysis expression becomes Eq. (3-3).

$$q'' = \frac{UI}{A_{boiling}} = \frac{UI}{a \times b} \quad \text{Eq. (3-2)}$$

$$E_{q''} = \sqrt{\left(\frac{\partial q''}{\partial U}\right)^2 E_U^2 + \left(\frac{\partial q''}{\partial I}\right)^2 E_I^2 + \left(\frac{\partial q''}{\partial a}\right)^2 E_a^2 + \left(\frac{\partial q''}{\partial b}\right)^2 E_b^2} \quad \text{Eq. (3-3)}$$

where U and I are voltage and current applied on the sample respectively. a and b are length and width of the rectangular heating area. $E_{q''}$, E_U , E_I , and E_b are the uncertainties in q'' , U , I , a , and b respectively.

The uncertainties of U and I are obtained from the standard deviation of the measurement for each point in boiling curve. The uncertainties of a and b are obtained from standard deviation of the measurement of heating area for each sample. The wall temperature is measured directly by burying a T-type thermocouple. The uncertainty of temperature is obtained by standard deviation of the measurement for each point. Accounting for all instrument errors, in current work, the maximum uncertainties of heat flux and wall temperature are 1.69 W/cm² and 1.24 °C respectively. The uncertainty in temperature includes an estimate of the contact resistance present between the thermocouple and the wafer bottom surface (= 0.3 °C).

3.3 Experimental Results

3.3.1 Heat Loss from the Sample

As shown in Figure 3 - 8, in the steady state, the input energy to the sample was Joule heating which was calculated as $E_{in} = UI$, where U and I are measured voltage load and current across the ITO heater, respectively. There are three ways to dissipate this input energy: 1) boiling heat transfer $E_b = q_b'' \times A_1$, where A_1 is the actual boiling area of the sample, 2) natural convection to air underneath the sample, $E_a = q_a'' \times A_2$, where A_2 is the area of the sample exposed to air, and 3) natural convection to water beyond the boiling area on the sample, $E_w = q_w'' \times A_3$, where A_3 is the area which equals the difference of total sample area and actual boiling area. From energy conservation in steady state, Eq. (3-4) was obtained.

$$UI = q_b'' \times A_1 + q_a'' \times A_2 + q_w'' \times A_3 \quad \text{Eq. (3-4)}$$

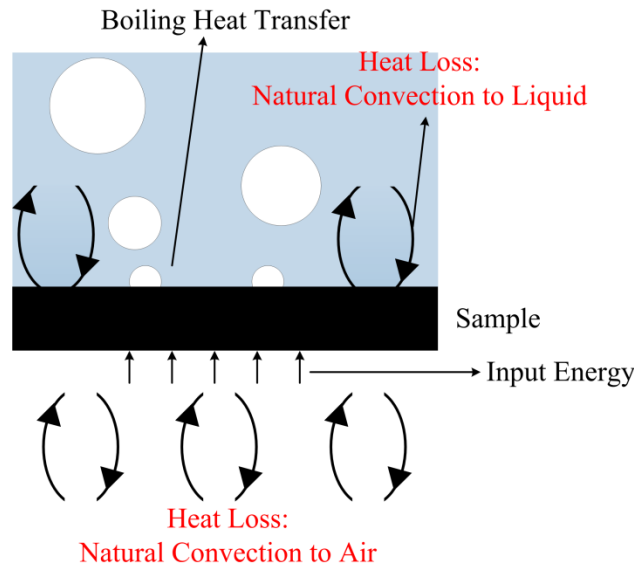


Figure 3 - 8 Heat loss from the sample

In order to calculate q_a'' and q_w'' , the heat transfer coefficient h was obtained from $\overline{Nu}_L = 3.092Ra_L^{0.272}$.¹²⁰ This equation was used to calculate the heat transfer coefficient of natural

convection from top surface of heated sample, and thus, the heat loss from underneath the sample (in the range of 2 to 3 W/cm²) was overestimated. Also, the temperature measured from thermocouple is that of the back side of the sample, which is not exactly the top surface temperature we need. The top surface temperature of the sample was determined as: $T_w = T_R - \frac{q_b \delta}{k}$, where T_w is the wall temperature of the sample's top surface; T_R is the temperature reading from thermocouple; q_b is the boiling heat flux.

3.3.2 Effect of Heat Conduction

As shown in Figure 3 - 9, the sample is heated by the ITO heater on the backside, while boiling occurs on the top side. The heat is not only conducted upward but also laterally due to heat conduction within the Si substrate; hence the actual boiling area is larger than the ITO heater area and it is necessary to calibrate the actual boiling area to achieve exact boiling heat flux.

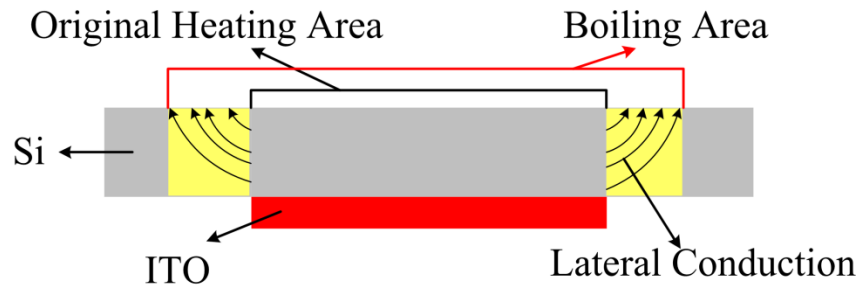


Figure 3 - 9 Effect of heat conduction in the fabricated samples

Figure 3 - 10 shows that the boiling area expands to $(a + 2L)$ cm \times $(b + 2L)$ cm. The expanded area is $2L[(a + b) + 2L]$ cm². The heat dissipated by boiling can be expressed as Eq. (3-5), in which wall superheat was measured in experiments.

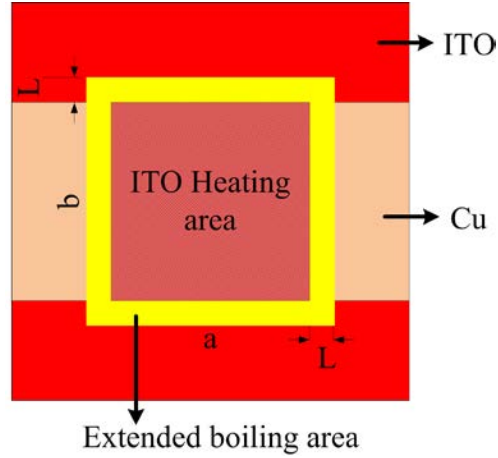


Figure 3 - 10 Actual boiling area calibration

$$E_b = h \cdot ab \cdot \Delta T + h \cdot 2L[(a + b) + 2L] \cdot \frac{\Delta T + \Delta T_{OSB}}{2} \quad \text{Eq. (3-5)}$$

From the energy balance, the heat dissipated through the expanded area is from lateral conduction in Si substrate, as shown in Eq. (3-6).

$$h \cdot 2L \cdot \frac{\Delta T + \Delta T_{OSB}}{2} = 2k \cdot \frac{\Delta T - \Delta T_{OSB}}{L} \cdot t \quad \text{Eq. (3-6)}$$

where k is thermal conductivity of Si (149 W/m·K), and t is the thickness of the wafer (500 μm).

Thus, Eq. (3-5) and Eq. (3-6) are iteratively solved to determine L and the actual boiling area.

We also investigated use of COMSOL simulations to estimate 2D heat conduction within the sample; however, the unknown values of two parameters (h and L) led to mismatch between simulation and experimental result of temperature (hence, a parametric sweep would have to be performed in COMSOL). Based on the orders of magnitude variation between thermal resistance of boiling (on the surface) and conduction (in the surface), we concluded that the 1D model is sufficient to estimate the actual boiling area.

3.3.3 Boiling Curves

In order to evaluate the boiling performance on ridge-structured surface, flat Si and SiO₂ surfaces are used as the baseline case. CHF values measured are $88.97 \pm 2.02 \text{ W/cm}^2$ and $78.79 \pm 1.64 \text{ W/cm}^2$ with the measured static contact angle of 44.5° and 36.3° for plain Si and SiO₂ surfaces, respectively, which are in good agreement with the reported values in the literature.^{37,39,66,109}

Figure 3 - 11 shows the boiling curves of Si ridges. The highest CHF attained is $158.8 \pm 3.26 \text{ W/cm}^2$, which is obtained by the Si #4 ridges with 1270 nm in height and 460 nm in width. Similar enhancements are also shown for Si #2 ($151.4 \pm 2.06 \text{ W/cm}^2$) and Si #3 ($147.8 \pm 1.96 \text{ W/cm}^2$) ridges which are 585 nm and 610 nm in height, and 460 nm and 745 nm in width respectively. However, no obvious enhancement is observed for Si #1 ridges ($98.3 \pm 1.23 \text{ W/cm}^2$) with 300 nm in height and 520 nm in width. In short, the height of ridges plays an important role in the enhancement of boiling. Thus, there exists a critical height below which no CHF enhancement is obtained, and above which similar enhancements are obtained irrespective of the ridge height. For Si surface, this critical height is in the range of 300 nm to 585 nm.

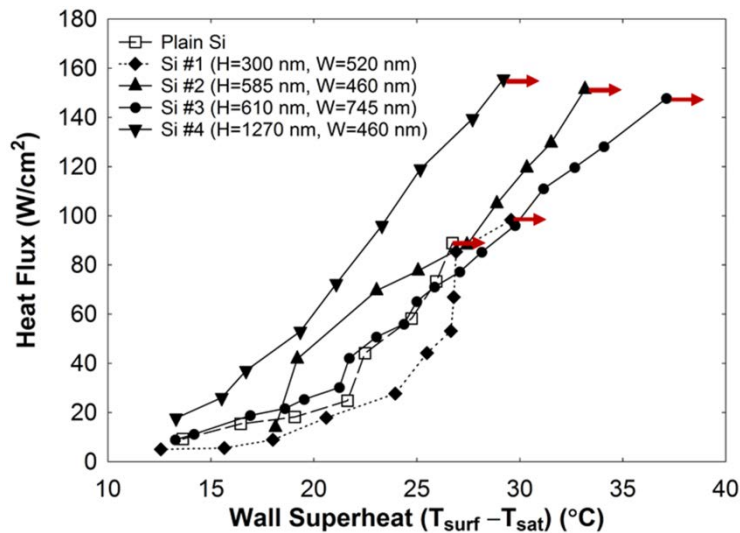


Figure 3 - 11 Boiling curves based on projected area for Si samples

Similarly, the same phenomenon is observed for SiO₂ ridges, as shown in Figure 3 - 12. The maximum CHF is $177.2 \pm 3.29 \text{ W/cm}^2$ obtained by SiO₂ #3 ridges which is 1060 nm in height. Similar CHF, $173.4 \pm 3.22 \text{ W/cm}^2$, is observed by SiO₂ #4 ridges (1530 nm in height). Equivalent CHFs to plain surface are obtained by SiO₂ #1 ($79.8 \pm 2.24 \text{ W/cm}^2$) and #2 ($74.8 \pm 0.94 \text{ W/cm}^2$) ridges with 585 nm and 665 nm in height respectively. Thus, for SiO₂ surface, the critical height for enhancement is in the range from 665 nm to 1060 nm.

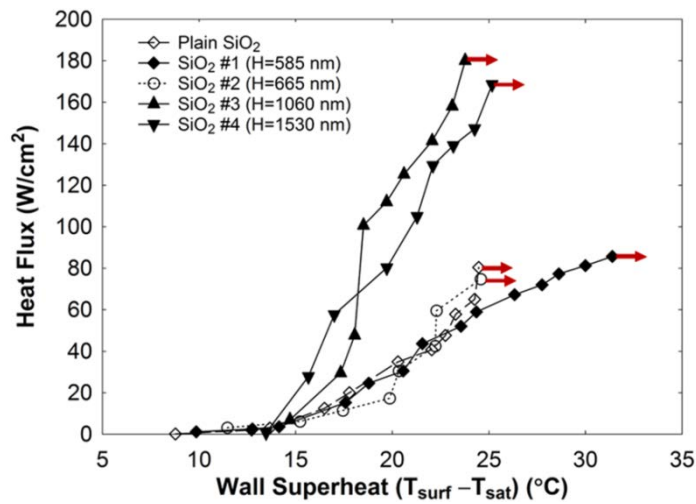


Figure 3 - 12 Boiling curves based on projected area for SiO₂ samples

The CHFs mentioned above are based on the projected area. However, the presence of ridges increases the solid-liquid contact area (the wetting area), which will also lead to improvement in CHF. Figure 3 - 13 and Figure 3 - 14 show the boiling curves based on the wetting area for Si and SiO₂ ridges. Maximum CHF is observed as $128.8 \pm 1.71 \text{ W/cm}^2$ (enhanced by 44.8%) and $127.8 \pm 2.37 \text{ W/cm}^2$ (enhanced by 62.2%) for Si and SiO₂ ridges respectively. In other words, ~125% CHF enhancement is obtained with just ~40% increase in surface area.

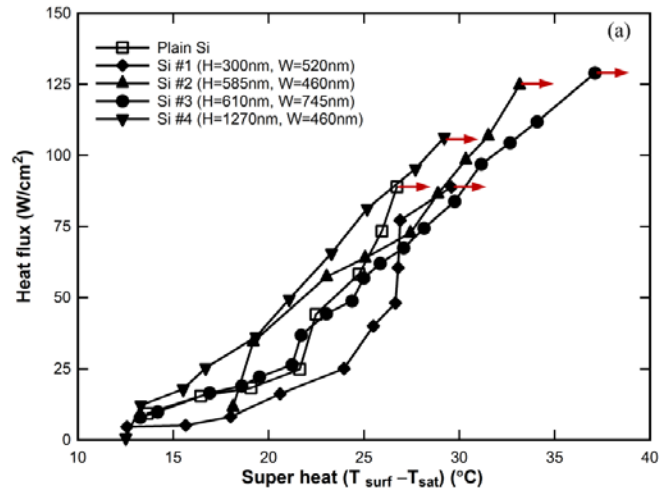


Figure 3 - 13 Boiling curves based on the wetting area for Si samples

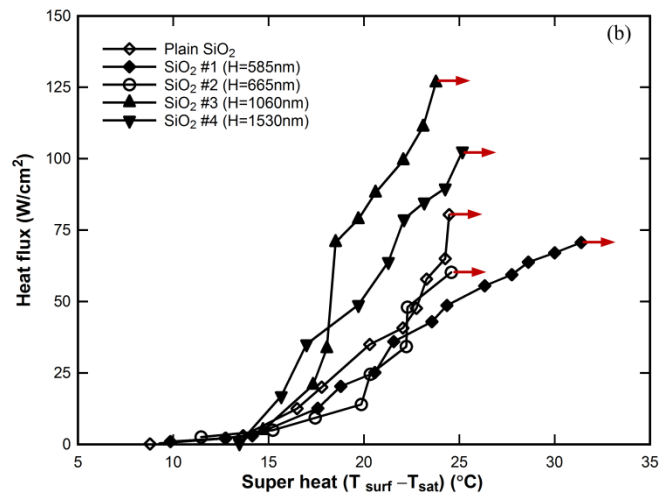


Figure 3 - 14 Boiling curves based on the wetting area for SiO₂ samples

3.4 CHF Enhancement Mechanisms

In the literature, the enhancement of boiling heat transfer due to micro/nano structures are normally attributed to increased nucleation site density,^{69,70,78} improved wettability or wicking effect to facilitate liquid supply,^{66,90,91,100,109,111,112} provided separate pathways for liquid and vapor flow to modify bubble dynamics,^{98,101,102} and increased roughness.^{37,113}

Firstly, the diameter of an active site is in the range from several microns to ~200 microns when the superheat is 10 – 20 K.^{6,78} In current work, the ridges were fabricated on the entire surface. Although the width of the ridge space is ~5 μm , its length is in centimeter scale along the ridges. Thus, the space between ridges is not considered as an active nucleation site.

Secondly, the enhancement of CHF on open-channel-structured surfaces is attributed to the provided separate pathways for liquid and vapor flow and the resulted modified bubble dynamics.^{98,101,102} This mechanism is based on the fact that the bubble nucleation occurs at the corner of the ridge wall due to the temperature difference between the top of the channel wall and the bottom of the channel. However, in current work, the largest ridge height is 1.5 μm . The temperature difference between the top and bottom surfaces can be obtained from Fourier's law (Eq. (3-7)).

$$\Delta T = \frac{q'' \cdot H}{k_s} \quad \text{Eq. (3-7)}$$

Considering the CHF as 200 W/cm^2 , the thermal conductivity of Si as 105 $\text{W}/\text{m}\cdot\text{K}$ at 120 $^\circ\text{C}$,¹²¹ the temperature difference corresponding to a 1.5 μm high ridge is 0.03 K, which is ~1% of the temperature difference (2.67 K) in the literature.^{98,101,102}

In the current section, the effects of possible enhancement mechanisms in the literature, such as improved wettability, facilitated liquid supply and increased roughness, are discussed first, and then a new enhancement mechanism, additional evaporation of thin film is proposed, as well as a corresponding analytical model.

3.4.1 Effect of Wettability

Surface wettability can be characterized by the contact angle which a liquid droplet makes on that surface. Compared to a plain surface, liquid droplets on nanostructured surfaces are in either of Wenzel or Cassie-Baxter states,⁴ as shown in Figure 3 - 15. In the Wenzel state, the liquid fills the space between the nanostructures and wets the entire solid surface. In this case, the actual solid-liquid contact area (wetting area) is larger than the projected area, and the contact angle can be expressed as Eq. (3-8).

$$\cos \theta_w = r \cdot \cos \theta \quad \text{Eq. (3-8)}$$

where r is roughness and θ is static contact angle on flat surface, which can be obtained by

$$\cos \theta = (\sigma_{sv} - \sigma_{sl}) / \sigma_{lv}.$$

While in the Cassie-Baxter state, the space between nanostructures is filled with air and the wetting area is smaller than the projected area. The contact angle becomes Eq. (3-9).

$$\cos \theta_{CB} = 1 - \phi_s(\cos \theta - 1) \quad \text{Eq. (3-9)}$$

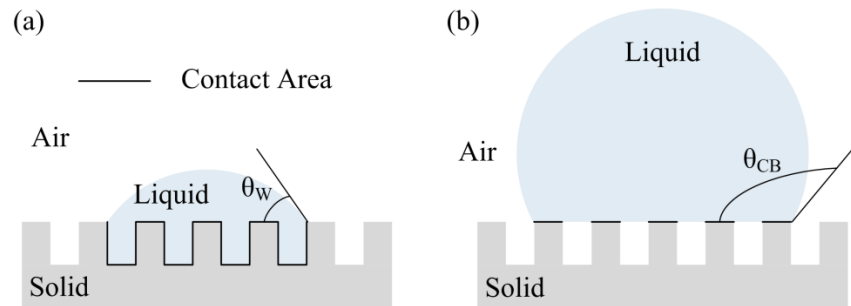


Figure 3 - 15 Liquid droplets on a structured surface in (a) Wenzel state and (b) Cassie-Baxter state

For ridge-structured surfaces in the present study, the droplet is stretched (based on side-view optical images; no top-view camera) along the ridges due to contact line pinning and capillary pressure, as shown in Figure 3 - 16, instead of forming a circular contact line on the surface. The

space between ridges acts as open capillary channels (explained in next section 3.4.2) to drive the liquid flow along the ridges for some distance, which stretches the droplet to a rectangular-like shape. Compared to the contact angle on a flat surface, the value is smaller in Y direction (along the ridges) and larger in X direction (across the ridges). Table 3 - 2 shows the contact angles of all samples in both X and Y directions.

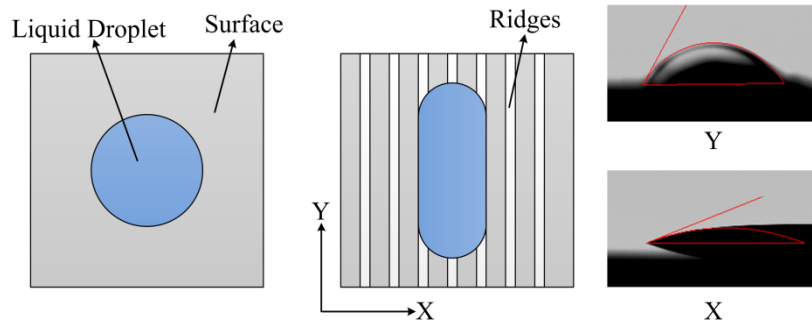


Figure 3 - 16 Stretched droplet along ridges and different contact angles in two directions

Table 3 - 2 Contact angles in two directions for all samples

Surfaces	X direction (deg)	Y direction (deg)
Si #1	19.15	47.45
Si #2	13.9	58.3
Si #3	14.75	57.45
Si #4	19.15	42.75
SiO ₂ #1	16.9	64.63
SiO ₂ #2	23.75	54.1
SiO ₂ #3	21	62.15
SiO ₂ #4	15.95	66.65

To determine the effect of wettability on CHF in the current study, Dhir's model¹²² and Kandlikar's model³⁴-which are widely used-are plotted with CHF of all tested samples in Figure 3 - 17. Neither Dhir's nor Kandlikar's model can predict the obtained enhancement, as the contact angles for all samples in either direction are similar to each other. Thus, for all samples, the wettability cannot differentiate the samples into ones which can enhance the CHF and the others which cannot. Also, as the contact angle changes due to geometry of ridges, the intrinsic contact angle (the contact angles measured on the flat surface) is used from here onwards.

$$q_{CHF}'' = h_l(1 - \alpha_w)\Delta T + h_v\alpha_w\Delta T \quad \text{Eq. (3-10)}$$

where h_l and h_v are average heat transfer coefficients in wetted area and dry region respectively; α_w is fraction of dry region on the wall.

$h_l = \frac{k_l \sum_{n=1}^{\infty} \frac{2 \sin^2(\lambda_n b)}{\lambda_n b + \sin(\lambda_n b) \cos(\lambda_n b)}}{b}$; $h_v = 0.37 \left[\frac{k_v^3 \rho_v (\rho_l - \rho_v) g h_{lv}}{\mu \Delta T \sqrt{\sigma / g (\rho_l - \rho_v)}} \right]^{1/4}$; where λ_n is eigenvalue, b is width of thermal boundary layer; contact angle affects α_w and b .

$$q_{CHF}'' = h_{lv} \rho_v^{1/2} \left(\frac{1 + \cos\theta}{16} \right) \left[\frac{2}{\pi} + \frac{\pi}{4} (1 + \cos\theta) \cos\phi \right]^{1/2} [\sigma g (\rho_l - \rho_v)]^{1/4} \quad \text{Eq. (3-11)}$$

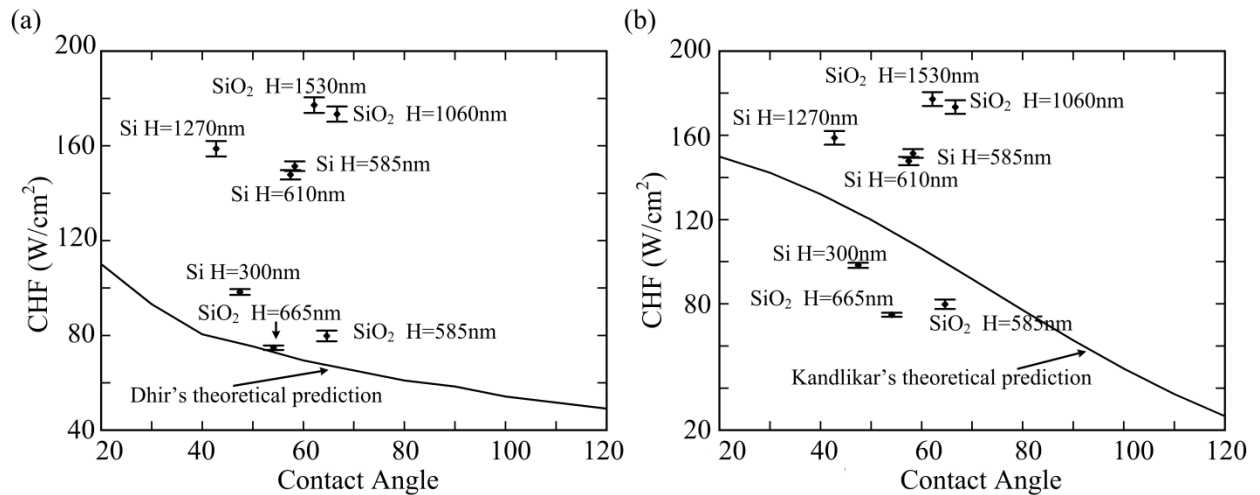


Figure 3 - 17 Comparison of CHF in current work to (a) Dhir's model¹²² and (b) Kandlikar's model³⁴

3.4.2 Effect of Liquid Supply

Another CHF enhancement mechanism of micro/nano structures is improved liquid supply. The space between structures provides a large capillary pumping force to bring liquid back to the dry spot, rewetting the surface. The space between ridges can act as open capillary channels pulling liquid to the dry area. Compared to plain surfaces, the liquid is brought to the center of the bubble base for a certain distance d , as shown in Figure 3 - 18. Hence, the contact line moves toward the center of the bubble base in the space between ridges. The movement of the contact line reduces the dry area underneath the bubble; in other words, it increases the liquid-solid contact area, resulting in CHF enhancement.

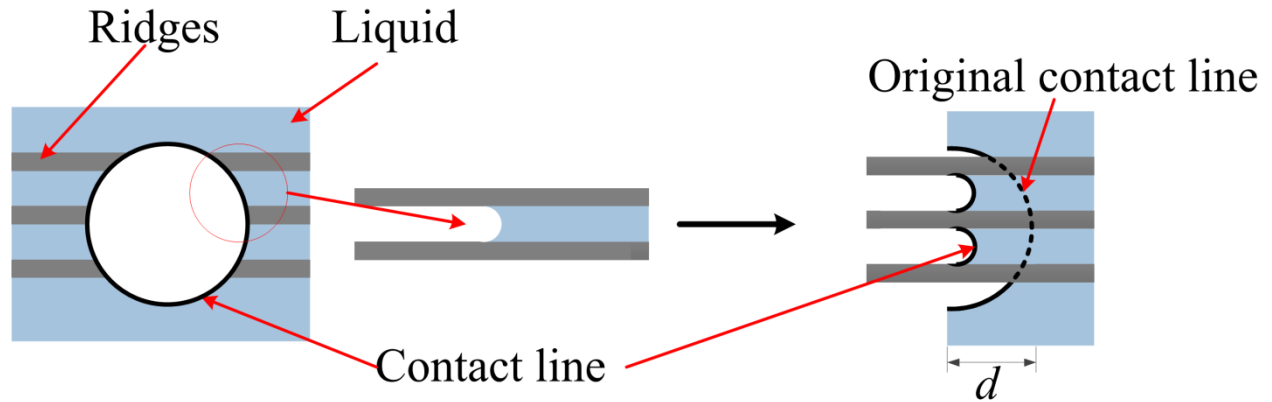


Figure 3 - 18 Pumping effect of spacing between ridges

Distance d is determined by both the evaporation rate and capillary pumping flow rate. In the equilibrium state, the local evaporation rate cancels the capillary flow rate. The capillary flow velocity v in an open channel can be obtained by Eq. (3-12).¹²³

$$v = \sqrt{\frac{2\sigma H[2\cos\theta - (1 - \cos\theta)p]16}{\mu p^2} \frac{1}{\pi^5} \sum_{n \geq 0, \text{ odd}} \frac{1}{n^5} \left[\frac{n\pi}{2} p - \tanh\left(\frac{n\pi}{2} p\right) \right]} \quad \text{Eq. (3-12)}$$

where $p = S/H$ denotes the aspect ratio of the channel and n is odd integer.

The liquid flow distance can be expressed by Eq. (3-13) from mass balance between liquid supply rate and evaporation rate.

$$d = \frac{v \cdot S \cdot H h_{lv} \rho}{h(S+2H)\Delta T} \quad \text{Eq. (3-13)}$$

where h is adopted from the literature¹²⁴ as 57944 W/m²K. As shown in Table 3 - 3, d is in the range from 6 to 60 μm depending on ridge heights. Thus, the majority of the area underneath the bubble would remain dry after the evaporation of the thin film when the contact line recedes, and the rewetting will only happen when the contact line advances during bubble departure. Based on the assumption³⁴ that the influence area of a bubble is a circle with diameter $2D_b$, the CHF enhancement contributed by capillary pumping E_c is obtained by Eq. (3-14), which is the ratio of extra solid-liquid contact area due to capillary pumping to total bubble affected area.

$$E_c = \frac{d \sin \theta}{D_b} \cdot \frac{S}{S+W} \quad \text{Eq. (3-14)}$$

Table 3 - 3 Effect of capillary pumping flow

Surfaces	v (m/s)	d (μm)	E_c (%)
Si #2	0.011	5.9	0.3
Si #3	0	0	0
Si #4	0.036	45.6	2.6
SiO ₂ #3	0.020	22.7	1.3
SiO ₂ #4	0.041	58.4	3.3

Table 3 - 3 shows the maximum contribution of capillary pumping flow to CHF enhancement is only 3.3%, and is thus negligible.

The effect of the improved liquid supply is further investigated by measuring the wickability¹⁰⁹ (wicked volume flux) for ridge-structured surface. A hydrophobic material coated capillary tube with a 500 μm inner diameter is filled up to a height of ~ 1 cm with DI water. The tested surface is raised with a translation stage until it touches the pendant droplet at the end of the tube. Due to the wicking effect of the ridges, the liquid spreads on the surface and thus the liquid height in the tube decreases. A high speed camera was used to record the height change, from which the liquid flow rate is determined. With a measured wetted area, the wicked volume flux can be obtained and the wicking number (Eq. (2-3)) can be calculated. For the sample SiO_2 #4, the wicking number is in the order of 10^{-6} . According to Eq. (2-4), the CHF enhancement is also in the order of 10^{-6} , which is ignorable.

3.4.3 Effect of Roughness

The reason that increased roughness is one of the CHF enhancement mechanisms is that the solid-liquid contact area is augmented and the three-phase contact line is elongated. The effect of augmented area is eliminated by considering the CHF based on actual wetting area, as shown in Figure 3 - 13 and Figure 3 - 14 where 44.8% and 62.2% enhancements were obtained. This enhancement is not contributed by the augmented area.

The effect of the elongated contact line is predicted by Chu's model.³⁷ As shown in Table 3 - 4 and Figure 3 - 19, the experimental results do not match the prediction, as the errors vary from 11.2% to 64.2%. Thus, the CHF enhancement in current work cannot be explained by increased roughness.

Table 3 - 4 Comparison between experimental data and Chu's model³⁷

Surfaces	Experimental CHF (W/cm ²)	Model (W/cm ²)	Error
Si#1	98.3±1.23	123.2	-20.3%
Si#2	151.4±2.06	98.7	53.4%
Si#3	147.8±1.96	95.6	54.6%
Si#4	158.8±3.26	142.8	11.2%
SiO ₂ #1	79.8±2.24	100.7	-20.8%
SiO ₂ #2	74.8±0.94	114.4	-34.6%
SiO ₂ #3	177.2±3.29	107.9	64.2%
SiO ₂ #4	173.4±3.22	142.4	21.8%

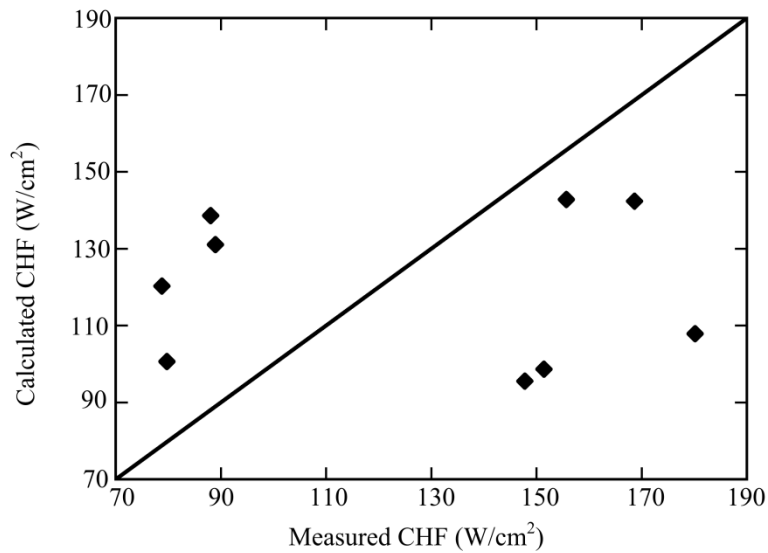


Figure 3 - 19 Comparison between experimental data and Chu's model³⁷

3.4.4 Additional Evaporation of the Thin Film

As discussed in section 3.1, a hypothesis was proposed where the CHF can be enhanced by the additional evaporation of the thin film present underneath the bubble. There are two cases

depending on ridge height. If the ridge height is larger than the film thickness, the film is disconnected from the bulk liquid and is broken into independent water slabs which evaporate. The additional evaporation occurs to facilitate bubble growth, and thereby the CHF. The enhancement that can be achieved depends on the film thickness. The thicker the film, the more liquid evaporates in additional evaporation and thus the bubble grows faster. If the ridge height is smaller than the thin film thickness, the film remained intact on the whole surface and is connected to the bulk liquid, as on the plain surface. The film is not ruptured and the additional evaporation does not occur, thereby providing no enhancement.

Based on this hypothesis, an analytical model is developed as follows. The boiling heat flux (q'') is contributed by three mechanisms: (a) the latent heat of evaporation to form the bubble (q_e''); (b) the heat required to form the thermal boundary layer after the bubble departure, namely the quenching heat flux (q_q''); (c) the natural convection occurring outside the zone of influence of the bubble (q_c''). From Gerardi and Buongiorno's work,¹⁵ quenching heat flux dominates the boiling heat flux for water and it can be given by Mikic's model (Eq. (3-15)).¹³

$$q_q'' = \frac{2\pi k_l (T_w - T_{sat})}{\sqrt{\pi \alpha_l}} \cdot N_a \cdot [D_b^2 (\sqrt{f_b})] \quad \text{Eq. (3-15)}$$

where the active nucleation site density can be obtained from Eq. (3-16).

$$\sqrt{N_a} = 25 \times 10^{-8} \left(\frac{h_{fg} \rho_g \Delta T}{T_s \sigma} \right)^{1.5} \quad \text{Eq. (3-16)}$$

In order to predict the CHF on a ridge-structured surface, two constants were introduced to Mikic's model: C_f and f_{ne} , as shown in Eq. (3-17).

$$q_{CHF}'' = C_f \frac{2\pi k_l (T_w - T_{sat})}{\sqrt{\pi \alpha_l}} \cdot N_a \cdot [D_b^2 (\sqrt{f_{ne} f_b})] \quad \text{Eq. (3-17)}$$

C_f accounts for the difference in the quenching heat flux (where nucleate boiling is still dominant) and CHF (where vapor slugs form). According to experimental data,¹⁵ the value of C_f is taken to be 1.35. f_{ne} is an additional evaporation factor, which represents the increased bubble departure frequency due to additional evaporation. It should be noted that the additional evaporation improves bubble departure frequency only. The bubble departure diameter depends on the forces exerted on the bubble. The main forces include buoyancy to lift the bubble, and surface tension holding the bubble on the surface. These two forces would not change due to the presence of ridges. Thus, the bubble departure diameter on the ridge-structured surface is assumed to be the same as that on the plain surface. The relation between bubble departure diameter and frequency on plain surface is described by Zuber's correlation (Eq. (3-18)),¹⁰ which is substituted to Eq. (3-15) to estimate the bubble departure diameter on the plain Si/SiO₂ surface; this turns out to be ~1.6 mm for both. This bubble departure diameter matches the experimental data from the literature.¹²⁵

$$f_b D_b = 0.59 \left[\frac{\sigma g (\rho_l - \rho_v)}{\rho_l^2} \right]^{1/4} \quad \text{Eq. (3-18)}$$

To identify the value of additional evaporation factor f_{ne} , two cases are considered, as shown in Figure 3 - 3. If the ridge height is larger than the film thickness, the volume of liquid water stored in the thin film underneath a bubble is calculated as in Eq. (3-19).

$$V = \pi (r_{dryout})^2 \delta_0 \quad \text{Eq. (3-19)}$$

The contact line moves outward from the center as the bubble grows. The bubble volume contributed by the additional evaporation of this amount of water is obtained as Eq. (3-20).

$$V_{e,1} = \frac{\rho_l \pi (r_{dryout})^2 \delta_0}{M_{H_2O}} \cdot \frac{S}{S+W} \cdot \frac{RT}{P_l + \frac{2\sigma}{r}} \quad \text{Eq. (3-20)}$$

It should be noted that r_{dryout} is the difference between $r_b \cdot \sin\theta$ (bubble base radius) and liquid flow distance d (Eq. (3-13)) due to liquid spreading, not simply the same as bubble base radius. For all samples, the values of r_{dryout} are about 0.5 mm, which also matches the experimental observation¹²⁵ very well.

The contact line moves back to rewet the solid surface as the bubble departs from the surface,^{125,126} causing additional evaporation to occur again. Thus, during the complete bubble ebullition cycle, the total contribution of additional evaporation becomes Eq. (3-21).

$$V_e = \frac{2\rho_l \pi (r_{dryout})^2 \delta_0}{M_{H_2O}} \cdot \frac{S}{S+W} \cdot \frac{RT}{P_l + \frac{2\sigma}{r}} \quad \text{Eq. (3-21)}$$

By assuming that the shape of the bubble which is starting to depart from surface is partial sphere (image of a bubble on ridge-structured surface will be shown in section 4.3.4), the volume of the bubble can be expressed as Eq. (3-22).

$$V_b = \frac{\pi}{6} (r + r \cos\theta) [3r^2 \sin^2\theta + (r + r \cos\theta)^2] \quad \text{Eq. (3-22)}$$

f_{ne} represents the increased bubble departure frequency due to the additional evaporation. Thus, it can be expressed as the function of V_b and V_{ne} as Eq. (3-23).

$$f_{ne} = \frac{V_b}{V_b - V_e} \quad \text{Eq. (3-23)}$$

By substituting Eq. (3-21) and Eq. (3-22) to Eq. (3-23), f_{ne} can finally be obtained as Eq. (3-24).

$$f_{ne} = \frac{\frac{\pi}{6} (r + r \cos\theta) [3r^2 \sin^2\theta + (r + r \cos\theta)^2]}{\frac{\pi}{6} (r + r \cos\theta) [3r^2 \sin^2\theta + (r + r \cos\theta)^2] - \frac{2\rho_l \pi (r_{dryout})^2 \delta_0}{M_{H_2O}} \cdot \frac{S}{S+W} \cdot \frac{RT}{P_l + \frac{2\sigma}{r}}} \quad \text{Eq. (3-24)}$$

If the ridge height is smaller than the film thickness, the film remains intact on the entire surface and is connected to the bulk liquid. The additional evaporation does not occur and thus $V_{ne} = 0$ and $f_{ne} = 1$. From Eq. (3-17) and Eq. (3-24), the CHF on the ridge-structured surface can be predicted by adjusting the average film thickness. Thus, this thickness serves as the critical height for micro/nano structures for pool boiling heat transfer enhancement. As shown in Figure 3 - 20, a good match between the experimental CHF results and those predicted by the analytical model (Eq. (3-17)) is achieved by estimating thin film thickness δ_0 as 450 nm and 900 nm for Si and SiO₂ surfaces, respectively. These values of the film thickness are further substantiated by the fact that samples with ridge height smaller than δ_0 do not show CHF enhancements. The samples with ridge heights greater than δ_0 have similar CHF enhancements irrespective of the ridge height since V_{ne} remains constant.

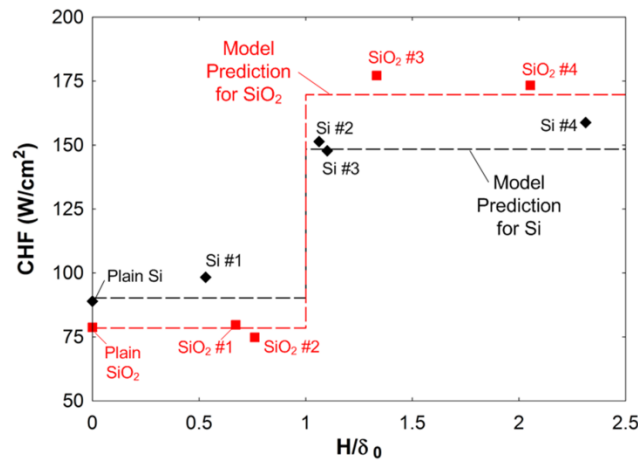


Figure 3 - 20 Comparison of experimental CHF with the analytical model

3.5 Summary

In this chapter, a fundamental study is conducted on pool boiling CHF enhancement by additional evaporation of the thin film underneath the bubble in contact line region. A new mechanism for enhancing pool boiling heat transfer is proposed. Significant enhancement in

CHF is attained: ~120% enhancement is achieved with only 40% augmentation in surface area. CHF predictions from the proposed analytical model are in good agreement with the experimental results and validate the hypothesis. CHF enhancement occurs only when the ridge heights are greater than the thin film thickness, thus defining the film thickness as the critical height for micro/nano structures for pool boiling enhancement. For Si and SiO₂ surfaces, this critical height is determined to be ~ 450 nm and ~900 nm, respectively.

4. Early Evaporation of Microlayer to Enhance CHF

4.1 Hypothesis

Chapter 3 introduced the significant role ridge height plays in CHF enhancement. The film thickness serves as the critical height below which no enhancement can be obtained; while above that, similar enhancements can be achieved. However, the effect of ridge spacing was not considered.

The ridge spacing can possibly affect CHF enhancement in two ways. First, from the analytical model (Eq. (4-1)), the ratio of space to width ($S / (S + W)$) determines the amount of the liquid between ridges that can evaporate to facilitate bubble growth, and thereby the level of CHF enhancement that can be attained.

$$q_{CHF}'' = C_f \frac{2\pi k_l (T_w - T_{sat})}{\sqrt{\pi \alpha_l}} \cdot N_a \cdot [D_b^2 (\sqrt{f_{ne} f_b})] \quad \text{Eq. (4-1)}$$

$$\text{where } f_{ne} = \frac{\frac{\pi}{6}(r+r\cos\theta)[3r^2\sin^2\theta+(r+r\cos\theta)^2]}{\frac{\pi}{6}(r+r\cos\theta)[3r^2\sin^2\theta+(r+r\cos\theta)^2] - \frac{2\rho_l\pi(r\text{dryout})^2\delta_0}{M_{H_2O}} \cdot \frac{S}{S+W} \cdot \frac{RT}{P_l + \frac{2\gamma}{r}}}$$

On the other hand, as shown in Figure 4 - 1, although the right height is larger than the thin film thickness, the microlayer in region II still connects to bulk liquid due to its curvature. It is not broken into water slabs and thus additional evaporation would not occur in this region. CHF enhancement can probably deteriorate in such a case.

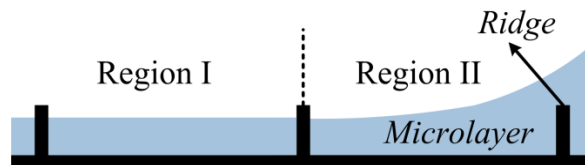


Figure 4 - 1 Microlayer connected to bulk liquid with large ridge space

Based on these two postulates, a hypothesis of early evaporation of microlayer is proposed, as shown in Figure 4 - 2. According to recent experimental observations from the literature,²³ on the plain surface, the microlayer forms when the bubble nucleates ($t = t_1$). As the bubble grows, the microlayer evaporates, becomes thinner ($t = t_2$), and finally forming a dry spot ($t = t_3$). With the presence of ridges, the disconnected microlayer can evaporate immediately to facilitate bubble growth (this will be discussed in section 4.3), and the microlayer evaporation occurs earlier compared to that on a plain surface. This early evaporation accelerates bubble growth and departure to enhance boiling heat transfer. In order to disconnect the microlayer from the bulk liquid, the required ridge height is expected to increase with the increased ridge space due to the microlayer curvature. By defining CHF values predicted from Eq. (4-1) as 'full enhancement', and CHF values between those on a plain surface and the full enhancement value as 'partial enhancement', ridges can be divided into four types (Figure 4 - 2).

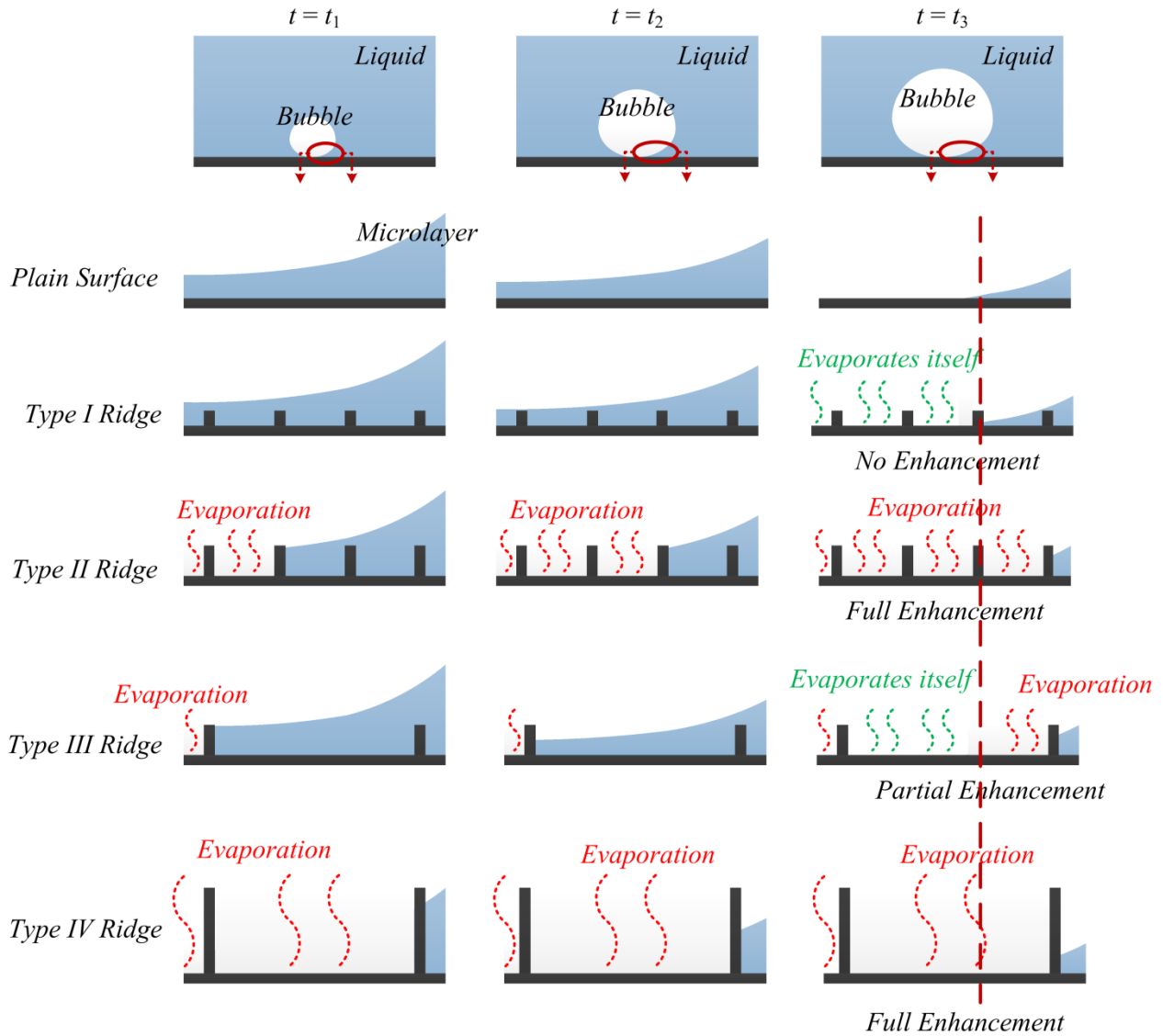


Figure 4 - 2 Early evaporation and four types of ridges

For type I ridges, as with those in chapter 3 without any enhancement, the microlayer thickness is larger than ridge height. Water slabs do not form and early evaporation does not occur.

Although a dry spot forms at $t = t_3$, there is no difference compared to the plain surface. No enhancements are expected.

For type II ridges, at the early stage of bubble growth, only a small part of the microlayer close to the center is lower than the ridge height, and it is disconnected from the bulk liquid. Thus,

early evaporation occurs in this region only at the early stage of the bubble growth ($t = t_1$). The microlayer in the outer region evaporates and becomes thinner and thinner as the bubble grows. Once its thickness is less than the ridge height, the disconnected microlayer evaporates immediately and the dry spot forms. Compared to the plain surface, the dry spot forms earlier and it is larger on ridge-structured surfaces. This early evaporation promotes bubble growth and thereby bubble departure frequency, resulting in full enhancement of CHF.

In type III ridges, the ridge space increases and early evaporation occurs as type II ridges at the center at $t = t_1$. However, the microlayer in the outer region remains connected to the bulk liquid due to the increased thickness in radial direction. At $t = t_3$, a dry spots forms as on the plain surface. Compared to the plain surface, only a part of region dries out because of the presence of ridges (the red region); the other part (the green region) dries out due to the evaporation as it would on a plain surface (without the effect of ridges). In this case, the bubble growth rate will increase, but not as much as in the type II ridges, resulting in the partially enhanced CHF.

However, with the same ridge space, if the height is increased to values large enough to disconnect the microlayer from bulk liquid, as depicted in type IV ridges, early evaporation would occur as in type II ridges resulting in a full enhancement of CHF.

Based on this hypothesis, increased ridge spacing can deteriorate CHF enhancement because the outer region of microlayer can still remain connected to the bulk liquid; however, increase in height at such increased spacing can lead to full CHF enhancement. Further, the shape of ridges is not expected to significantly affect CHF enhancement because the microlayer disconnection from the bulk liquid is the essential trigger mechanism which causes early evaporation.

4.2 Experimental Results

4.2.1 Sample Fabrication

To validate the hypothesis that the early evaporation of the microlayer enhances CHF, ridges with varied spacing and height were fabricated in the same way as described in section 3.2.1.

Table 4 - 1 lists the dimensions of all samples, which can be divided into four categories: 5-micron spacing, 9-micron spacing, 20-micron spacing, and 48-micron spacing ridges. The height varies from 1.2 μm to 4.4 μm . There are two kinds of ridge shape: rectangle and trapezoid.

Figure 4 - 3 shows SEM images of the side view of ridges.

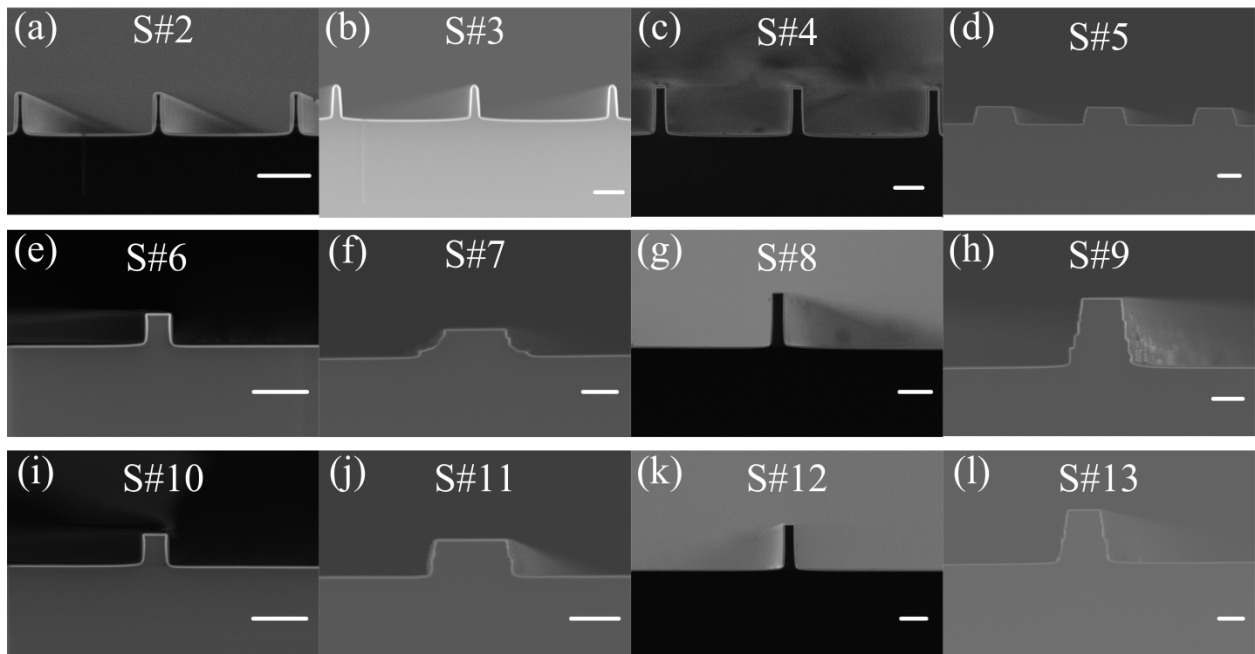


Figure 4 - 3 SEM images of fabricated ridges

Table 4 - 1 Geometry of fabricated ridges

	Height H (μm)	Width W (μm)	Spacing S (μm)	Shape
S #1	1.06	0.59	4.89	Rectangle
S #2	1.53	0.55	5.00	Rectangle
S #3	1.52	4.17	5.81	Trapezoid
S #4	2.44	1.00	9.09	Rectangle
S #5	3.38	0.97	8.99	Rectangle
S #6	1.17	1.13	23.62	Rectangle
S #7	1.59	4.24	20.86	Trapezoid
S #8	3.41	0.86	23.80	Rectangle
S #9	4.38	3.46	21.53	Trapezoid
S #10	1.18	1.17	48.29	Rectangle
S #11	1.52	4.51	45.27	Trapezoid
S #12	3.40	1.08	48.03	Rectangle
S #13	4.33	3.35	45.89	Trapezoid

4.2.2 Boiling Curves

Figure 4 - 4, Figure 4 - 5, and Figure 4 - 6 show boiling curves for ridges with spacing of 5 μm , 9 μm , 20 μm , and 48 μm respectively. In the plots, the blue dotted line represents the prediction from Eq. (4-1) and the dark green dashed line represents the CHF value on the plain SiO_2 surface, which is $80.9 \pm 0.39 \text{ W/cm}^2$. The highest CHF was achieved by S #1 ($W = 0.6 \mu\text{m}$, $S = 4.89 \mu\text{m}$, $H = 1.1 \mu\text{m}$) as $177.8 \pm 0.90 \text{ W/cm}^2$ and S #13 ($W = 3.4 \mu\text{m}$, $S = 45.9 \mu\text{m}$, $H = 4.3 \mu\text{m}$) as $177.0 \pm 1.14 \text{ W/cm}^2$. 120% enhancement was achieved with only 40% and 18% increase in

surface area for S #1 and S #13 respectively. If considering the actual wetting area, 86% enhancement was achieved by S #13 as $150.5 \pm 0.98 \text{ W/cm}^2$. This enhancement is among the highest reported for structured surfaces in the literatures (Figure 4 - 7).^{21,37,83,84,87,88,96,98,101,102,127} On the other hand, partial enhancements were observed for ridges with spacing of $9 \mu\text{m}$, $20 \mu\text{m}$, and $48 \mu\text{m}$, as expected from the hypothesis. In order to achieve full enhancement for the ridges with the spacing of $9 \mu\text{m}$, ridge height of $3.4 \mu\text{m}$ was required. The full enhancement height increased to $4.4 \mu\text{m}$ for ridges with spacing of $20 \mu\text{m}$ and $48 \mu\text{m}$.

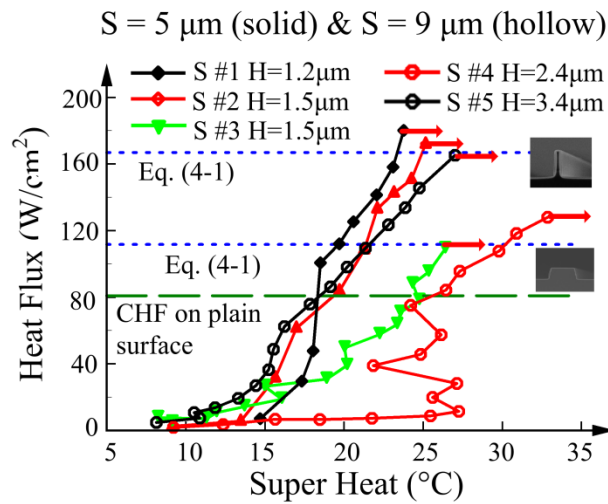


Figure 4 - 4 Boiling curves of samples with the ridge spacing of $5 \mu\text{m}$ and $9 \mu\text{m}$

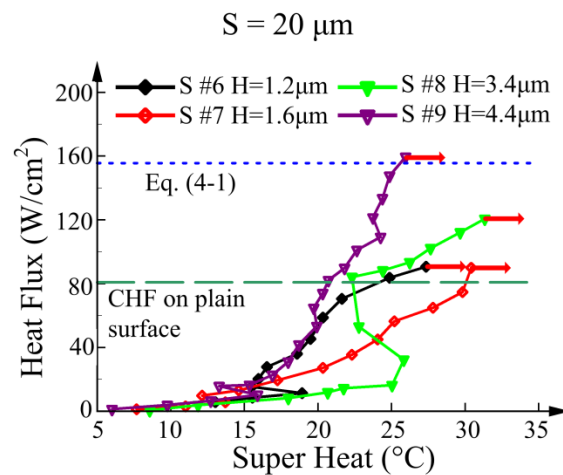


Figure 4 - 5 Boiling curves of samples with the ridge spacing of $20 \mu\text{m}$

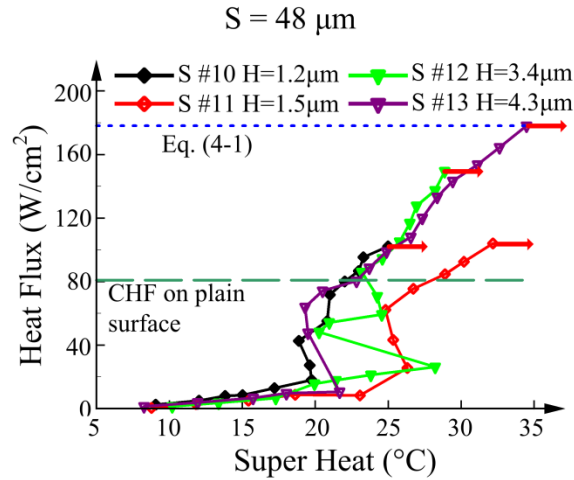


Figure 4 - 6 Boiling curves of samples with the ridge spacing of 48 μm

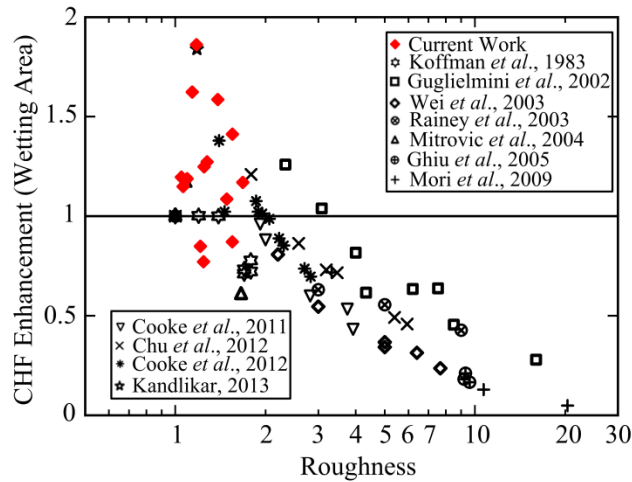


Figure 4 - 7 Comparison of CHF enhancements in current work with literatures^{21,35,81,82,85,86,94,96-98,124}

4.2.3 Effect of Ridge Shape

Figure 4 - 4 shows the effect of the ridge shape on CHF enhancement. The ridge spacing is 5 μm and the heights are 1.5 μm for both S #2 (rectangular ridge) and S #3 (trapezoidal ridge).

Although CHF is much lower with the trapezoidal ridges (S #3, $109.1 \pm 1.14 \text{ W/cm}^2$), compared to rectangular ridges (S #2, $177.1 \pm 0.94 \text{ W/cm}^2$), it matches the prediction from Eq. (4-1) within 5% error. The CHF difference is due to the ratio of ridge space to width ($S / (S + W)$), which is

0.582 and 0.900 for trapezoidal and rectangular ridges respectively. Full enhancement can be reached regardless of the ridge shape. The irrelevance between CHF enhancement and ridge shape is a validation of the hypothesis that the disconnection of microlayer from the bulk liquid is essential to reach CHF enhancement.

4.2.4 Effect of Ridge Spacing

As shown in Figure 4 - 4, Figure 4 - 5, and Figure 4 - 6, CHF enhancement depends on the coupled effect of the ridge height and spacing. As expected, enhancements were obtained by ridges with heights larger than the critical height (H_{cr}); the full enhancement height (H_f) increased from 1.1 μm to 3.4 μm to 4.4 μm as the ridge space increased from 5 μm to 20 μm to 48 μm . For those ridges with heights between H_{cr} and H_f , only partial enhancements were obtained. The enhancements are divided into three regions depending on ridge height and spacing (Figure 4 - 8): region I as the full enhancement region ($H > H_f$), region II as the partial enhancement region ($H_{cr} < H < H_f$), and region III as the no enhancement region ($H < H_{cr}$).

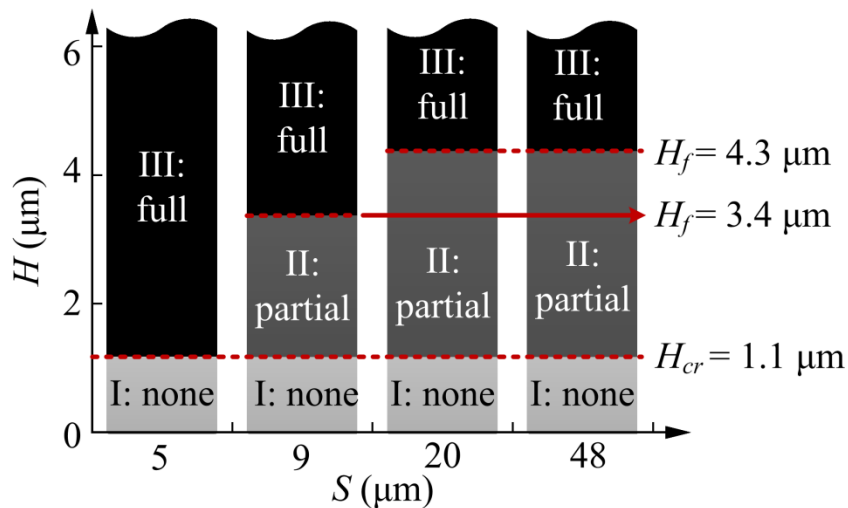


Figure 4 - 8 Three regions of CHF enhancement

In order to discuss the coupled effect of height and spacing, a dimensionless enhancement variable η (Eq. (4-2)) is defined as the ratio of experimental CHF to predicted CHF from Eq. (4-1). Full enhancement is achieved when $\eta = 1$, while $\eta < 1$ indicates the partial enhancement and its value represents the fraction of the full enhancement that has been achieved.

$$\eta = \frac{\text{CHF}_{exp}}{\text{CHF}_{mp}} \quad \text{Eq. (4-2)}$$

In region I, the CHF on the ridge-structured surface is similar to the plain surface. The ridge height is smaller than H_{cr} , which corresponds to type I ridge, thus the microlayer remains connected to the bulk liquid and covers the entire surface. The early evaporation of microlayer does not occur and thus no enhancement was obtained.

In region II, only partial enhancement was obtained by type III ridges. The CHF enhancement is affected by ridge height and spacing simultaneously. The ratio of the ridge height to H_f determines the percentage of full enhancement that can be achieved, while ridge spacing determines H_f , which will be discussed later. Figure 4 - 9 shows that the dimensionless enhancement variable η is proportional to the ratio of ridge height to full enhancement height. The relationship between η and H/H_f follows curve fitting Eq. (4-3) obtained from experimental results and the error is less than 10%.

$$\eta = 0.281 \frac{H}{H_f} + 0.501 \quad \text{Eq. (4-3)}$$

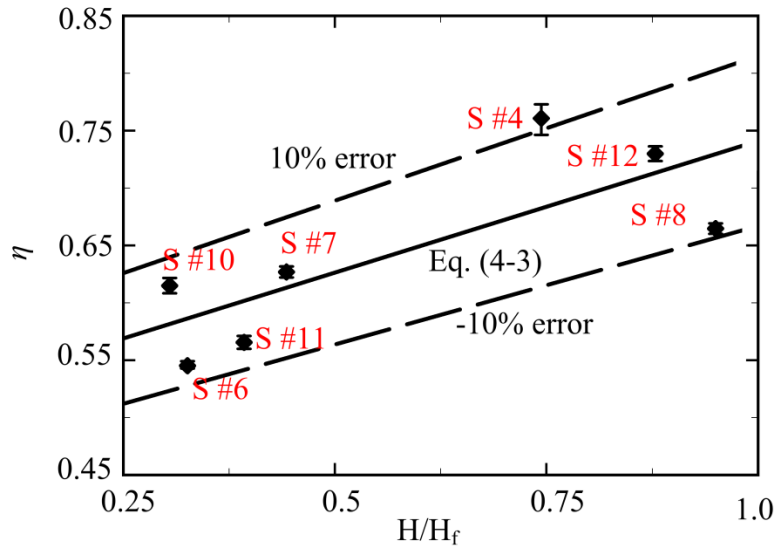


Figure 4 - 9 Relation between enhancement variable and H/H_f

In region III, fully enhanced CHF was achieved with type II and type IV ridges and can be predicted by Eq. (4-1). It is determined by the ratio of ridge spacing to width ($S / (S + W)$), which specifies the quantity of liquid between ridges for an equivalent projected surface area. As shown in Figure 4 - 10, the error between experimental results of the fully enhanced CHF and the prediction of the analytical model (Eq. (4-1)) is less than 10%.

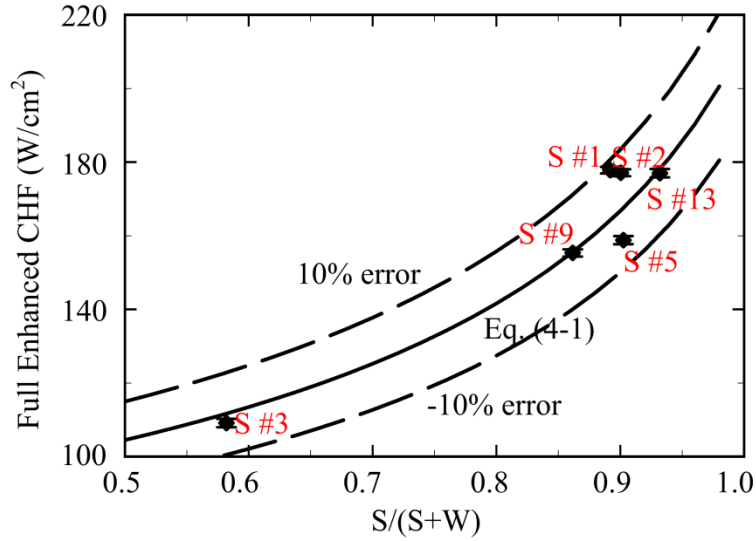


Figure 4 - 10 Relation between the full enhancement variable and the ratio of ridge spacing to width

Thus, full enhancement can be achieved with ridges with increasing height. Full enhancement height H_f increases with increasing spacing. From current experimental results, H_f can be predicted by curve fitting as Eq. (4-4).

$$H_f = \begin{cases} 1.1 & S = 5 \\ 2.9(S - 5)^{0.1055} & S > 5 \end{cases} \quad \text{Eq. (4-4)}$$

The maximum H_f is around $3.9 \mu\text{m}$, which is similar to the thickness of the outermost microlayer in the literature ($\sim 3.3 \mu\text{m}$) in which the ITO was used as heater surface.²³ The interaction between water and ITO is weaker than SiO_2 because the drop contact angle is $\sim 65^\circ$, which is larger than that on the SiO_2 surface ($30^\circ \sim 40^\circ$). Hence, the thicker microlayer is expected on SiO_2 surfaces under the same conditions.

Thus, there exists a coupled effect of ridge spacing and height on CHF enhancement. The ratio of space to width ($S / (S + W)$) determines the full enhancement that can be reached by ridge-structured surface, while the ratio of ridge height to full enhancement height (H / H_f) determines

the percentage of the full enhancement that can be achieved. Full enhancement height is determined by ridge spacing. Qualitatively speaking, larger spacing requires larger height to achieve full enhancement (Eq. (4-4)).

4.2.5 Enhancement Map

As mentioned earlier, there are three CHF enhancement regions based on the ridge dimensions. Eq. (4-5) shows the enhancement map in which the x axis represents ridge spacing while the y axis represents ridge height. For a certain ridge spacing, the three regions depending on ridge height are: no enhancement region ($H < H_{cr}$), partial enhancement region ($H_{cr} \leq H < H_f$), and full enhancement region ($H \geq H_f$). CHF on ridge-structured surface can be predicted by Eq. (4-5).

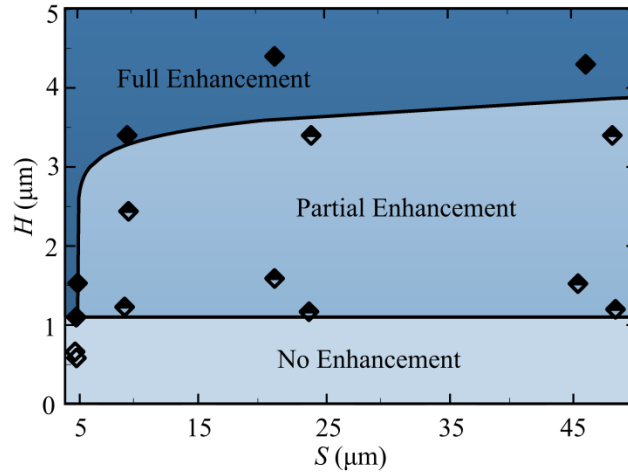


Figure 4 - 11 CHF enhancement map

$$q_{CHF}'' = \begin{cases} C_f \frac{2\pi k_l (T_w - T_{sat})}{\sqrt{\pi \alpha_l}} \cdot N_a \cdot [D_b^2 (\sqrt{f_{ne} f_b})] & H \geq H_f \\ \left(0.281 \frac{H}{H_f} + 0.501\right) \cdot C_f \frac{2\pi k_l (T_w - T_{sat})}{\sqrt{\pi \alpha_l}} \cdot N_a \cdot [D_b^2 (\sqrt{f_{ne} f_b})] & H_{cr} \leq H < H_f \\ C_f \frac{2\pi k_l (T_w - T_{sat})}{\sqrt{\pi \alpha_l}} \cdot N_a \cdot [D_b^2 (\sqrt{f_b})] & H < H_{cr} \end{cases} \quad \text{Eq. (4-5)}$$

where

$$f_{ne} = \frac{V_b}{V_b - V_e}$$

$$V_b = \frac{\pi}{6} (r + r \cos \theta) [3r^2 \sin^2 \theta + (r + r \cos \theta)^2]; V_{ne} = \frac{2\rho_l \pi (r_{dryout})^2 \delta_0}{M_{H_2O}} \cdot \frac{S}{S+W} \cdot \frac{RT}{P_l + \frac{2\gamma}{r}}$$

$$H_f = \begin{cases} 1.1 & S = 5 \\ 2.9(S - 5)^{0.1055} & S > 5 \end{cases}$$

The existence of three CHF enhancement regions validates the hypothesis that the CHF enhancement is achieved by the early evaporation of microlayer. It is essential that the ridge height is large enough to disconnect the microlayer from the bulk liquid and trigger its early evaporation. However, the microlayer is thicker in the outer region due to its curvature, which makes it possible that the larger ridge spacing leaves a region in which the microlayer remains connected to the bulk liquid (type III ridge in Figure 4 - 2).

4.3 Early Evaporation of Microlayer

CHF enhancement by disconnecting the microlayer from the bulk liquid is based on the assumption that the microlayer evaporates quickly once the separation is achieved. This assumption is validated from the literature data,²³ where for an average boiling heat flux of 5.3 W/cm², the maximum microlayer thickness of water was found to be around 3 μm spreading over a region with a width of several hundred microns. The maximum wall heat flux underneath the microlayer was in the order of 100 W/cm². The microlayer will evaporate completely without liquid being replenished in ~57 ns with a wall heat flux of 30 W/cm², which is the smallest value underneath the microlayer during a bubble ebullition cycle. Compared to a whole bubble ebullition cycle time scale (9.17 ms) under the same average boiling heat flux, the time required for evaporating the microlayer completely is extremely short and it can completely evaporate before the bubble departs. Considering the water slabs between ridges, the outermost part of the

microlayer for a 48 μm ridge space, which is the thickest and widest water slab in current work, will evaporate, and the dry spot will form in ~ 12 ns. Thus, once the water slab forms and is disconnected from the bulk liquid, it will evaporate immediately.

The early evaporation of the microlayer is further validated by comparison of the growth rate of a laser-created bubble on a ridge-structured surface and a plain surface. The bubble was created by heating the surface using a femtosecond laser source. The bubble formation process was recorded by a high-speed camera and the bubble growth rate was analyzed.

4.3.1 Experimental Setup and Sample Fabrication

As shown in Figure 4 - 12, a Ti:Sapphire ultrafast laser was used to generate high power laser pulses with an average peak power of 2.7 W at 800 nm. The laser pulses were then passed through Second Harmonic Generation setup, which generated 400 nm pulses with an average peak power of 450 mW. The power of the pulses were controlled/attenuated using a mountable continuously variable neutral density (ND) filter, which was then directed into the inverted microscope. These laser pulses were reflected to the sample, through the objective, using a reflector module, a 30:70 beam splitter. A 100x objective lens was used to focus the laser beam to ~ 10 μm beam spot size at the focus. The laser pulses are absorbed by the 40 nm gold thin-film deposited on silica glass slide, which creates a highly localized heating area corresponding to the beam size. A 6 cm glass tube had been mounted on the sample that holds the degassed DI water. When the heat flux was increased using the ND filter, a bubble was generated and reached the steady state after growing to a certain size at which equilibrium state was reached between evaporation at the bottom of the bubble and condensation at the upper part of the bubble. The length of the tube is sufficient to prevent the diffusion of gasses back into the degassed water to the sample bottom where the bubbles are generated. The bubble was imaged using the white light

Halogen lamp source or 632 nm HeNe laser placed at the top for illumination, through the same objective lens. The image of the bubble was transmitted to a high speed camera (Phantom V611), with which the frame rate can be as high as 1M frames per second (fps). To prevent the 400 nm laser light (reflected by the sample) from disrupting the image, a 425 nm Long Pass Filter was placed after the beam splitter that allows a majority of white light to be transmitted through to camera while reflecting back the 400 nm light from the laser.

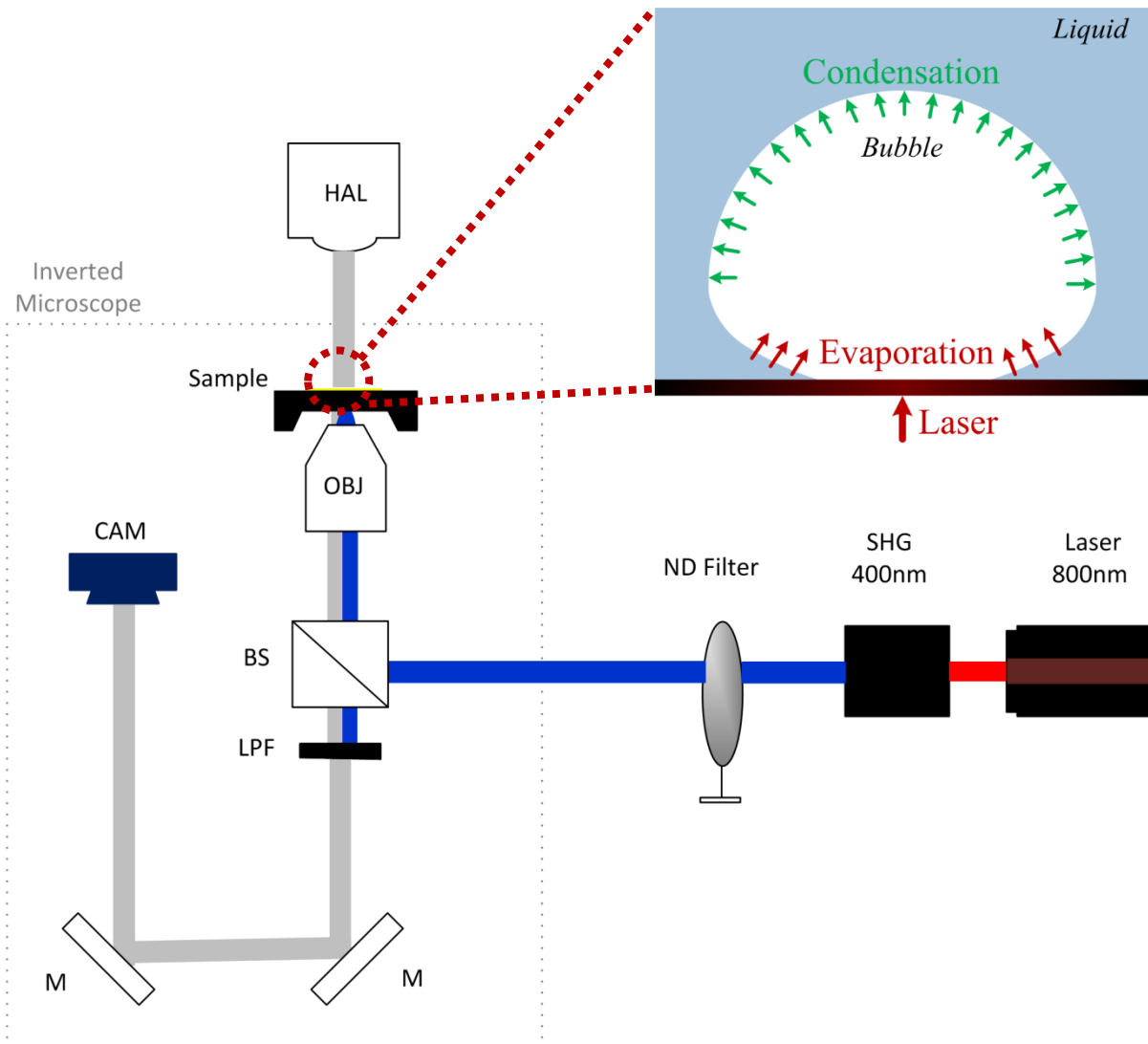


Figure 4 - 12 Schematic of the experiment setup for bubble growth rate comparison

Figure 4 - 13 shows the schematic of the samples used for performing the bubble growth rate experiments. The plain surface was fabricated by sandwiching a 40 nm thick Au layer (deposited by thermal evaporation) to absorb the laser between a glass slide and a 300 nm thick deposited SiO₂ layer (deposited by sputtering). Between Au and SiO₂, a 10 nm thick film of Cr (deposited by thermal evaporation) was used as an adhesion layer.

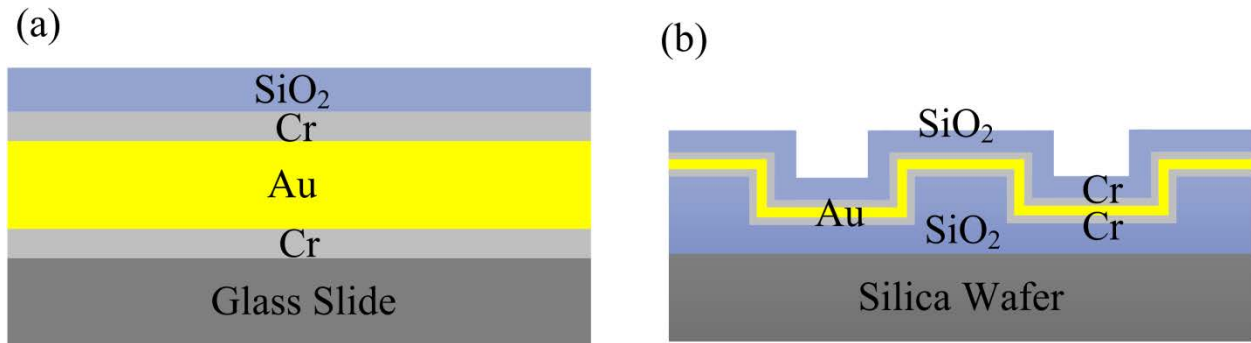


Figure 4 - 13 Schematic of the samples for bubble growth rate comparison (a) plain surface (b) ridge-structured surface

In order to fabricate the sample for the ridge-structured surface, a 3 μm thick SiO₂ layer was deposited first on a silica wafer using plasma enhanced chemical vapor deposition (PECVD). The ridges ($W = 0.5 \mu\text{m}$, $S = 4.8 \mu\text{m}$, $H = 1.5 \mu\text{m}$) were then attained by following a similar procedure as described in section 3.2.1. After that, similar to the plain surface, a 40 nm thick Au layer was deposited on ridge-structured surface, and then was covered by a 300 nm SiO₂ layer by sputtering. A thermal evaporation deposited 10 nm thick Cr layer was used as the adhesion layer between Au and SiO₂.

4.3.2 Experimental Procedure

After fabrication, the samples were cleaned with acetone, ethanol, and IPA successively. The chemical residue was washed away using DI water. Next, the sample was cleaned using oxygen plasma for 5 min. The sample was then washed and cleaned using DI water again before the

experiments. A 6 cm long and 1.4 cm inner diameter glass tube was bonded on the surface by epoxy. It was filled with DI water which was degassed by boiling it for an hour. The water was then cooled down to room temperature in a sealed bottle. In the tests, the laser was aligned to pass through the sample perpendicularly. Before filling the tube, the tested liquid was passed through a filter with the pore size of 220 nm to eliminate the particles suspended in the liquid. The laser was aligned to be normal to the surface. A bubble was created and reached steady state in a few seconds (evaporation occurring at the base of the bubble equaled condensation at the upper liquid-vapor interface of the bubble). A high-speed camera was then used to record the bubble formation process, and the growth rate was obtained from the analysis of the bubble volume.

4.3.3 Bubble Volume

Figure 4 - 14 (a) shows a schematic of the bubble image. The illumination (a white halogen lamp or a 632 nm HeNe laser) is from the top vertically downward and the camera is located under the sample. The images provide a bottom view of the bubble, which has a dark annulus region as light has to pass through multiple liquid-vapor interfaces in that region. The inner diameter represents bubble base diameter D_{bb} while the outer diameter is bubble diameter D_{bd} . In Figure 4 - 14, (b1) and (b2) show a typical image of the bubble on the plain surface with white and red illumination respectively, (c1) and (c2) show the bubble on the ridge-structured surface with white and red illumination respectively. By assuming bubble shape as partial sphere, the bubble volume can be calculated from measured D_{bb} and D_{bd} by Eq. (4-6).

$$V = \frac{\pi}{6} \left(\frac{D_{bd}}{2} \right)^3 - \frac{\pi}{6} c \left(3 \left(\frac{D_{bb}}{2} \right)^2 + c^2 \right) \quad \text{Eq. (4-6)}$$

$$\text{where } c = \frac{D_{bd}}{2} - \sqrt{\left(\frac{D_{bd}}{2} \right)^2 - \left(\frac{D_{bb}}{2} \right)^2}$$

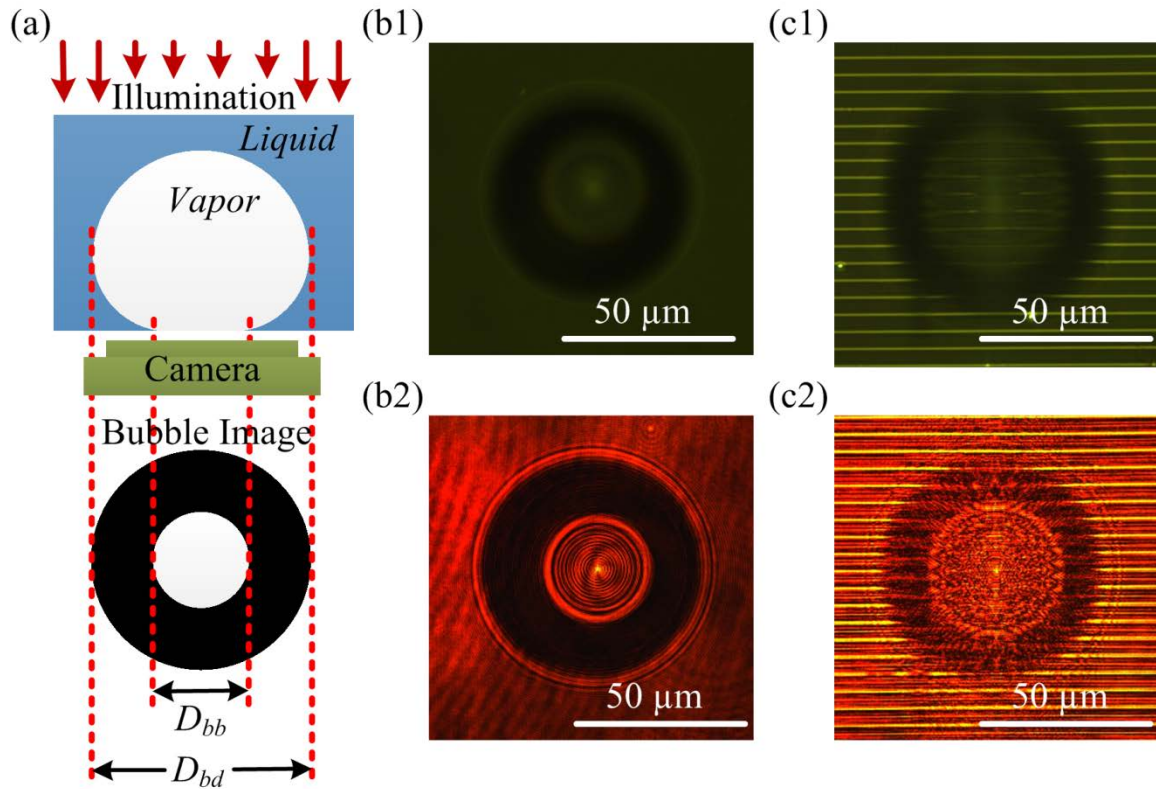


Figure 4 - 14 (a) schematic of bubble image; typical bubble image on plain surface (b1) white (b2) red illumination and on ridge-structured surface (c1) white (c2) red illumination

4.3.4 Validation of Early Evaporation of Microlayer

Video from the high-speed camera was used to capture 1000 frames per second, which allows for a 1 ms of temporal resolution. Figure 4 - 15 and Figure 4 - 16 show selected images of a growing bubble on plain surface and ridge-structured surface at time of 10 ms, 100 ms, 1000 ms, 2000 ms, and 5000 ms, respectively. The bubble volume was calculated at each 50 ms during the early growth stage and the time step was increased to 500 ms after the bubble was found to grow linearly.

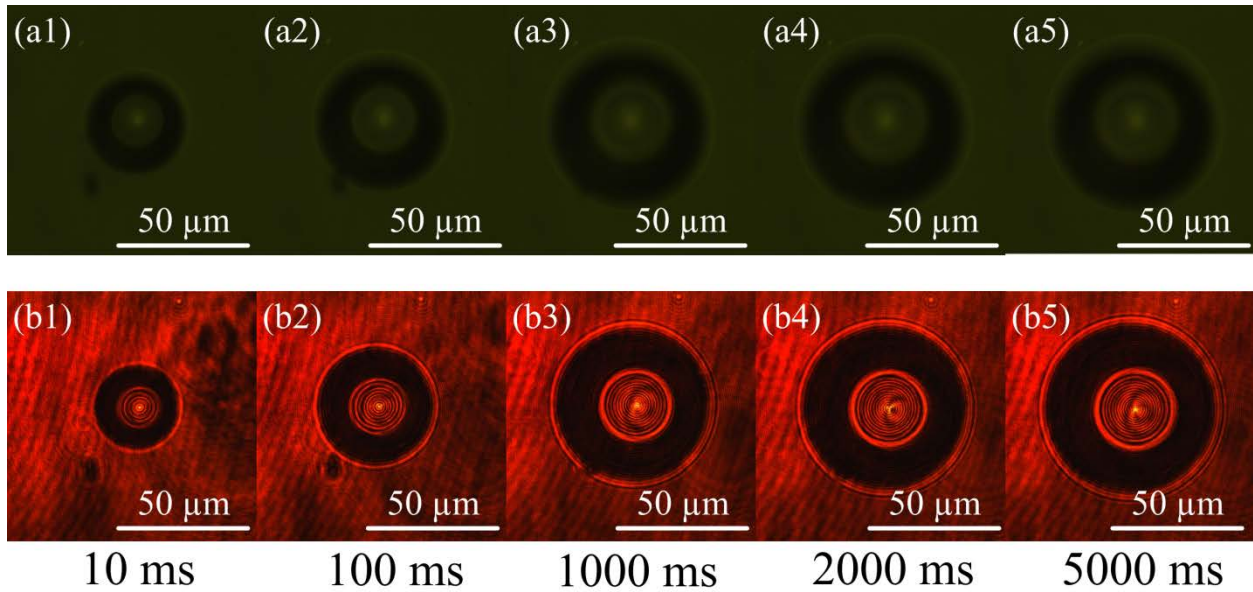


Figure 4 - 15 Bubble growth on plain surface with (a) white and (b) red illumination

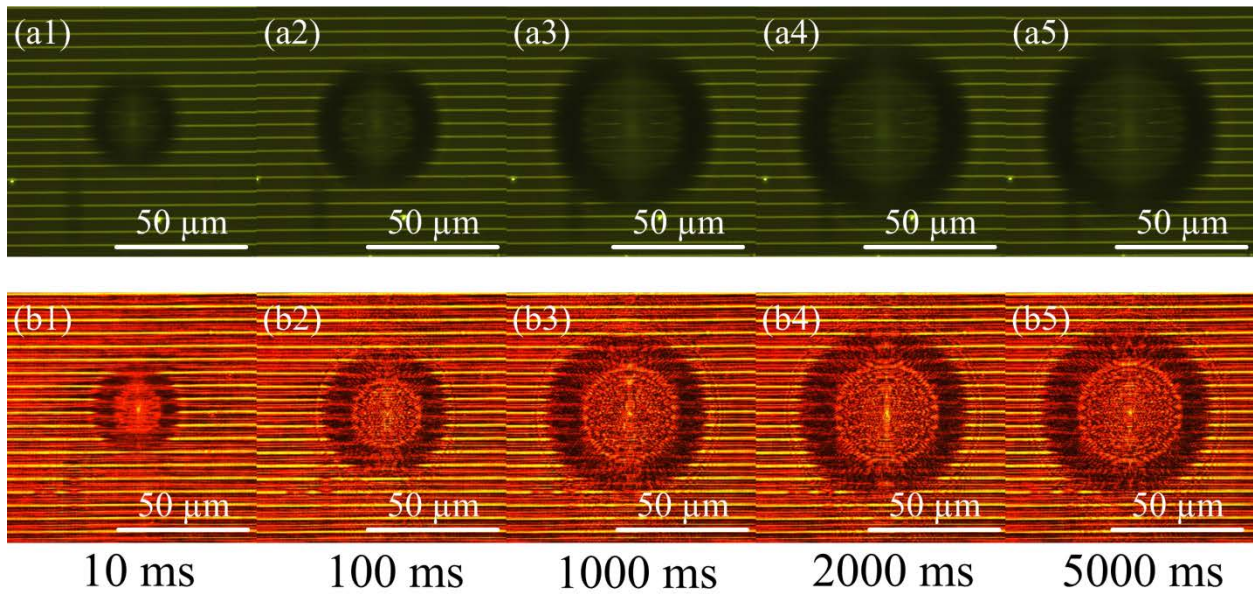


Figure 4 - 16 Bubble growth on ridge-structured surface with (a) white and (b) red illumination

The bubble growth rate was obtained by plotting bubble volume versus time and from the slope of the linear regression curve, as shown in Figure 4 - 17. The growth rate was found to be $(0.441 \pm 0.017) \times 10^5 \mu\text{m}^3/\text{s}$ on the ridge-structured surface, 5.25 times as fast as on the plain surface $((0.084 \pm 0.008) \times 10^5 \mu\text{m}^3/\text{s})$. The bubble growth rate depends on liquid property and wall

temperature,⁸ which are the same in both cases. This growth rate difference originates from the early evaporation of the microlayer. Thus the microlayer profile, especially the thickness, determines the quantity of liquid water that can evaporate and enhance the bubble growth rate. From the literature,^{21,23} the thickness of the outermost microlayer is $\sim 3 \mu\text{m}$ over a wide range of heat flux (5.3 W/cm^2 to 20.4 W/cm^2), with the bulk temperature varying from 78.3°C to 97°C ; thus, the microlayer thickness is not expected to change significantly over various sub-cooling levels. Based on these experimental observations, the comparison of the growth rate of a laser-created bubble is related to the CHF enhancement obtained in boiling with ridges.

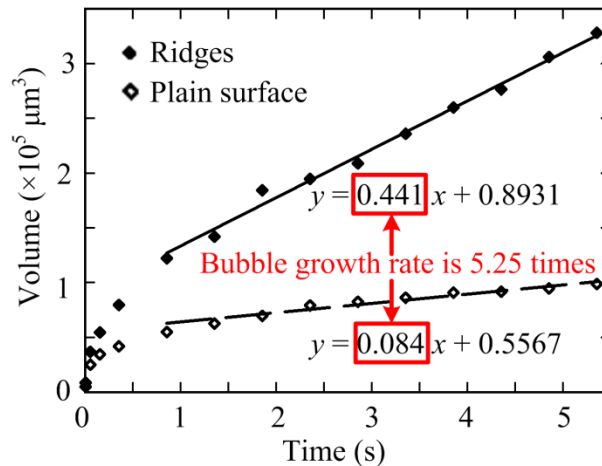


Figure 4 - 17 Comparison of bubble growth rate on plain surface and ridge-structured surface

From Eq. (4-1), CHF is proportional to the square root of the bubble departure frequency, which is determined by bubble growth time and waiting period time. The waiting period is the time during which the fresh liquid rewets the surface and is superheated to form the thermal boundary layer before nucleation occurs. Thus, early evaporation will affect bubble growth rate after nucleation occurs. However, the waiting period time close to CHF (super heat is 30°C) is ~ 0.09 ms, which is $\sim 10\%$ of a total bubble ebullition time of ~ 1 ms. This calculation matches the experimental observation¹⁵ in which the waiting period occupies 15% of the complete bubble

ebullition cycle. Taking into account the waiting period time, the expected CHF on this ridge-structured surface can be calculated from Eq. (4-7) as 1.92 times that on the plain surface. As shown in Figure 4 - 18, CHF on the same dimension of the ridge-structured surface is enhanced to 2.19 times, which matches the above estimation based on increase in bubble growth rate within an error of 14%.

$$\frac{q''_{CHF-ridges}}{q''_{CHF-plain}} = \frac{1}{\sqrt{\frac{t_w}{t_w+t_g} \times 1 + \frac{t_g/(t_w+t_g)}{E_{bg}}}} \quad \text{Eq. (4-7)}$$

where t_w is the waiting time, t_g is the bubble growth time and E_{bg} is the increased bubble growth rate, which is 5.25 for this ridge-structured surface.

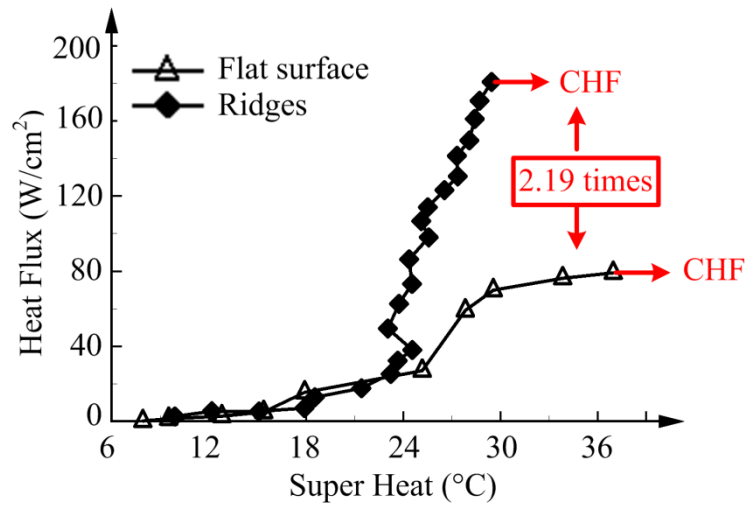


Figure 4 - 18 Comparison of CHF on plain surface and ridge-structured surface

Figure 4-1

Thus, the hypothesis that CHF enhancement occurs on ridge-structured surfaces due to increased bubble growth rate is verified through independent experiments. This work has proposed and validated a new CHF enhancement mechanism based on the early evaporation of microlayer present at the base of the bubble.

4.4 Summary

This chapter introduced a fundamental study on pool boiling CHF enhancement by early evaporation of the microlayer, which is achieved by fabricating ridges with height and width of a few microns to disconnect the microlayer from the bulk liquid. A ~120% enhancement was obtained with only 18% augmentation in surface area, which is among the highest reported value in literature. There exist three enhancement regions depending on ridge spacing and height: full enhancement region, partial enhancement region, and no enhancement region. Ridge spacing determined the full enhancement height (H_f): larger spacing requires a higher H_f . The ratio of space to width ($S/(S+W)$) determined the full enhancement that can be reached, while the ratio of height to full enhancement height (H/H_f) determined the percentage of the full enhancement that can be achieved. An empirical model was proposed to predict the CHF based on the dimensions of ridge spacing, width, and height. Further, the hypothesis was independently verified by the comparison of growth rates of a laser created bubble on ridge-structured surface and plain surface.

5. Steady Vapor Bubble in Pool Boiling

5.1 Introduction

Contact line evaporation models,^{24,29} as well as transient conduction,¹³ microconvection,¹⁶ and microlayer evaporation,^{17,19} have been widely accepted as the basic heat-transfer mechanisms in boiling. The dynamics of contact line region and the microlayer dictate bubble growth and departure, and are of significant importance in understanding the fundamental behavior of the boiling phenomenon.⁴ Visualization of the boiling process and the contact line region has recently been pursued by researchers^{15,20-23,128} and has had a tremendous impact in providing a realistic depiction of the boiling process; however, the unsteady nature and short time-span of the bubble ebullition cycle (~1ms) has made *in-situ* imaging of a single bubble very challenging, especially for a bubble in its early growth stage.

On the other hand, the contact line region is incorporated into predictive boiling models through contact angle values.^{34,122} The intricacies involving the shape of an interface and the behavior of the contact line are implicitly accounted for in the contact angle, thus making the bubble contact angle parameter of significant importance in boiling models. However, while static or advancing/receding contact angles of a liquid droplet on the surface at room temperature are often used for boiling models,^{34,37} it is difficult to relate the boiling process to the droplet wetting characteristics due to the highly transient conditions associated with liquid-vapor phase change.^{12,28,129}

There are three types of techniques that have been commonly used to measure bubble contact angle: the captive-bubble technique, the flotometric method, and bubble imaging.

(a) *Captive – Bubble Technique*. It is widely used to measure the bubble contact angle,¹³⁰⁻¹³² in which the solid sample is placed in a chamber filled with liquid, and an air bubble is made by using a microsyringe and attached underneath the surface. Drelich^{130,131} measured the bubble contact angle in air/water/methylated quartz system. The results showed that the advancing contact angle of the drop and the bubble are similar, while the receding contact angle of the bubble is around 10° larger than that of drop. When using captive-bubble technique, the gravity and buoyancy play opposite roles compared to the boiling process. It is doubtful that the bubble contact angle values can be adopted in boiling process directly.

(b) *The Flotometric Method*. This technique is based on flotation.¹³³⁻¹³⁷ A tube was filled with a mixture of distilled water and solid particles. A bubble was introduced from the bottom of the tube. Some particles adhere to the bubble forming a particle-air aggregate which is lighter than water and travel upwards to the water surface. The particle size for which the recovery (percentage of floating particle) of flotation is equal to 50% is defined as maximum size of floating particles, which is a function of the bubble contact angle and liquid surface tension. The bubble contact angle can be determined because the liquid surface tension is easy to measure. However, the particle surface is not smooth in this measurement while the contact angle is highly dependent on surface topological properties,⁴ and the temperature effect is not included, neither.

(c) *Bubble Imaging*. Rapid evaporation affects the drop contact angle,¹³⁸ which implies the measurement of the bubble contact angle must simulate the surrounding condition of a bubble in boiling, in order to use its values in boiling models. Some researchers have made their efforts to investigate bubble contact angle in boiling process.¹³⁹⁻¹⁴¹ Serret *et al.*¹³⁹ obtained the bubble contact angle of FC-72 on Al surface experimentally. In their setup, the cover and bottom of the boiling chamber were made of Al. The upper Al block was heated underneath which boiling

occurs and the lower one was used to maintain the bulk liquid at the desired sub-cooling level. The results showed that the bubble contact angle was independent from heat flux and sub-cooling but the comparison between the contact angles of the bubble and the drop were not provided. Van der Geld¹⁴⁰ numerically obtained the dynamic contact angle histories of a truncated spherical bubble growing at the wall. To mimic the physics of actual vapor bubble growth, the expansion of the bubble was given as a function of initial radius R , which is not what actually happened during boiling and is believed to affect the contact angle. The results showed that the bubble contact angle was constant during bubble growth in the case of constant content of air, while in the case of constant bubble pressure, it kept decreasing to zero due to the imposing of the shape of the truncated sphere. Ramanujapu¹⁴¹ obtained the bubble contact angle during boiling on a silicon surface using high speed photography of the side view of the bubble. Compared to drop contact angle (54°), the bubble contact angles were $\sim 5^\circ$ less in bubble growth but $\sim 7^\circ$ more in bubble departure. The overall average in a whole life cycle is 55° , similar to the drop contact angle.

Thus, the contact angle of a vapor bubble in pool boiling has yet to be directly measured due to the dynamic nature of the bubble ebullition cycle; making it all the more necessary to image the contact line region to advance the understanding of the boiling process and enhance boiling heat transfer efficiency.

Here, a quasi-steady bubble is created by heating the surface, submerged in a pool of sub-cooled water, using a laser source. Using a constant laser power, the bubble reaches its steady state as evaporation rate in the microlayer present at the base of the bubble equals condensation rate on the cooler liquid-vapor interface. The transient bubble growth process is thus “frozen in time”

making it possible to do *in-situ* measurement of contact angle and investigate the heat transfer characteristics of a bubble in its early growth stage.

5.2 Experimental Methods

5.2.1 Sample Fabrication

Figure 5 - 1 shows the schematic of the sample used in experiments. Both hydrophilic (SiO_2) and hydrophobic (tridecafluoro-1,1,2,2-tetrahydrooctyl-trichlorosilane (FOTS)) surfaces are tested. To absorb the laser power to heat the sample, a 40 nm thick Au layer was sandwiched between the glass slide and a 300 nm thick deposited SiO_2 layer. An adhesion layer of 10 nm thick Cr was used between the Au and SiO_2 . The fabrication process consists of slide cleaning and a series of thin film deposition, such as thermal evaporation, sputtering, and molecular vapor deposition.

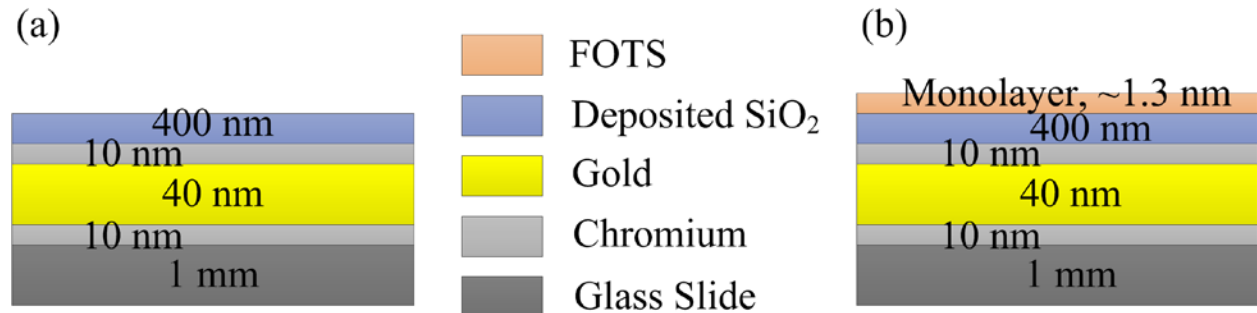


Figure 5 - 1 Description of fabricated sample for (a) SiO_2 surface (b) FOTS surface (not scaled)

(a) *Slide Cleaning*. Before film deposition, the slides were cleaned to make sure there was no dust or other contamination present. The slides were cleaned in a hot bath of Remover 1165 in two tanks, 10 minutes for each tank. The slides were then washed using DI water tank and were dried by blowing compressed nitrogen. After that, the wafers were further cleaned in Glen 1000 oxygen plasma at a power of 400 W for 5 minutes to remove any possible polymer residue.

(b) *Cr Deposition*. The first adhesion layer of a 10 nm thick Cr was deposited by thermal evaporation. A crystal sensor was used to monitor the thickness.




(c) *Au Deposition*. The laser absorption layer was 40 nm thick Au film. Similar to Cr deposition, it was deposited by thermal evaporation for ~30 min. The thickness was monitored using a crystal sensor.

(d) *Cr Deposition*. The second adhesion layer was deposited as in step (b).

(e) *SiO₂ deposition*. The hydrophilic surface on which the bubble will be generated was a 400 nm thick SiO₂ layer. It was deposited by RF sputtering at a power of 1.75 kW for 200 min.

(f) *FOTS deposition*. The hydrophobic surface was obtained by depositing a monolayer of FOTS on SiO₂. It was deposited using molecular vapor deposition (MVD). The thickness of this monolayer is expected to be around 1.3 nm, resulting in a drop contact angle of 105°.

Table 5 - 1 Sample surfaces and liquids used for experiments

Sample Surface	Drop Contact Angle	Liquid Tested	Experimental Image of Drop
Hydrophilic SiO ₂	0°	regular DI water	
Normal SiO ₂	33.4° ± 2.7°	regular & degassed DI water	
Trichlorosilane (FOTS)	109.8° ± 2.9°	degassed DI water	

Experiments were performed in both regular deionized (DI) water with dissolved air and degassed DI water on three types of surfaces: superhydrophilic SiO₂, normal SiO₂, and FOTS surfaces. The experiments on superhydrophilic SiO₂ surface were conducted immediately after a 5-min oxygen plasma cleaning of a normal SiO₂ sample. Table 5 - 1 lists the drop contact angle on these surfaces and the tested liquid on each.

5.2.2 Experimental Setup and Sample Preparation

The experimental setup is similar to that described in section 4.3.1 (Figure 4 - 12). A 5x/50x objective lens was then used to focus the laser beam to a 170 μm/20 μm circular spot. Different z-planes of the sample can be focused with the resolution of 10nm using the motorized control for z-position of the objective. Thus the bubble base and maximum bubble size was precisely imaged (with error of 100nm). The difference between the two z-planes was also measured to determine the bubble contact angle.

After the fabrication, the sample was cleaned with acetone, ethanol, and IPA successively, and the chemical residual was washed away by DI water. After this solvent cleaning, the hydrophilic sample was cleaned by the oxygen plasma for 5 min. The sample was washed and cleaned by DI water again before the experiments. In the experiments, the laser was aligned perpendicularly to the sample. The water was degassed by boiling it for an hour using a hot plate and then cooled to room temperature in a sealed bottle. The tested liquid (regular or degassed water) was passed through a filter with pore sizes of 220 nm to eliminate the particles suspended in the liquid. A pool of water was formed in a 6 cm long 1.4 cm inner diameter glass tube, which was bonded on the SiO₂ or FOTS surface to achieve boiling. The laser power was increased incrementally until the bubble formed. The length of the tube is sufficient to prevent the diffusion of gases back into

the degassed water to the surface where the bubbles are generated. The diffusion of air can be simplified as a 1-D problem (Eq. (5-1)).

$$\frac{\partial C}{\partial t} = D \frac{\partial^2 C}{\partial x^2} \quad \text{Eq. (5-1)}$$

Initial condition: $C(x, 0) = 0$; Boundary condition: $C(0, t) = C_0$, where C_0 is the saturation concentration of air in water

The solution of Eq. (5-1) is Eq. (5-2) and shows the concentration profile developed with time.

$$C(x, t) = C_0 \operatorname{erfc}\left(\frac{x}{\sqrt{4Dt}}\right) \quad \text{Eq. (5-2)}$$

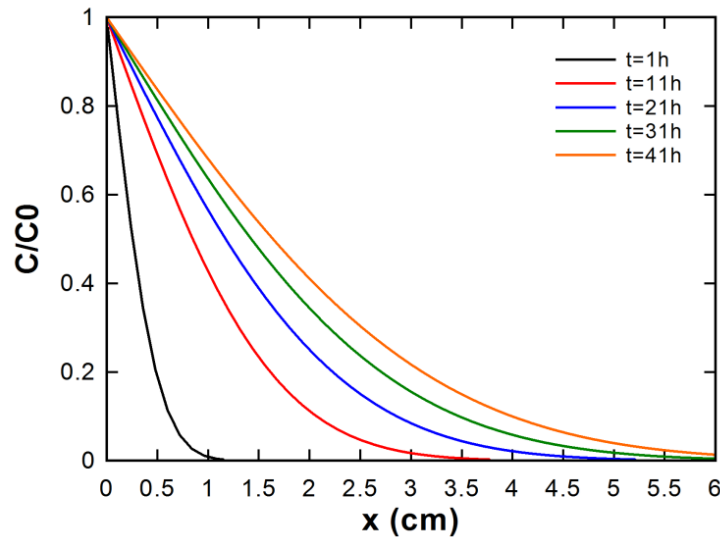


Figure 5 - 2 Diffusion profile of air in degassed water with time

Thus, it would take more than 24 hours for the air to diffuse to the bottom of the 6 cm long tube whereas each experimental measurement lasted for less than 2 hours. Convection currents due to bubble formation can increase diffusion of gases in water; however, experimental observations show that water remained degassed near the surface as the vapor bubble condensed and disappeared when the laser was turned off.

5.3 Bubble Contact Angle

5.3.1 Bubble Contact Angle Measurement

In order to measure the bubble contact angle, the laser power was increased incrementally until the bubble was formed. By placing a white light Halogen lamp source at the top for illumination, the bubble was imaged and transmitted to a digital camera. Figure 5 - 3 shows a typical bubble image and the schematic of calculation of bubble contact angle.

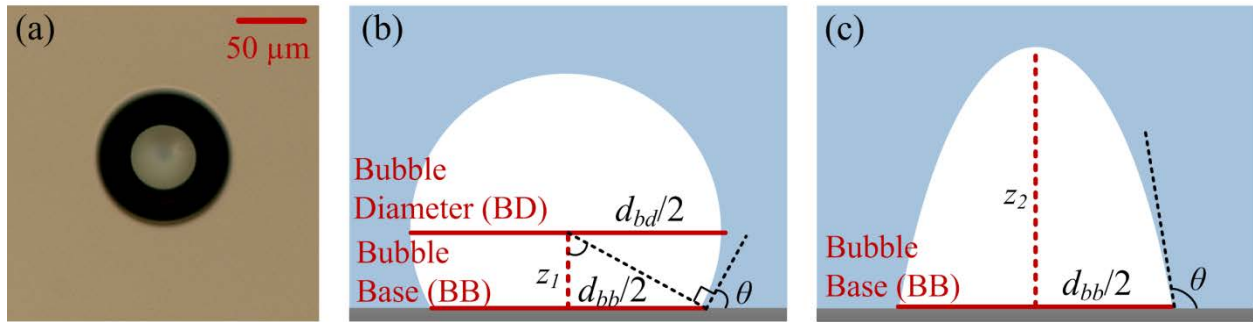


Figure 5 - 3 (a) Typical bubble image. Bubble shape and contact angle estimation on (b) hydrophilic SiO₂ and (c) hydrophobic FOTS surface

After a bubble is formed and reaches steady state on the SiO₂ surface, the bubble base diameter, d_{bb} , bubble diameter, d_{bd} , were read from the images. While the first reading of z position was taken by focusing on the surface, the second reading of z position was taken by focusing on the bubble middle plain. z_1 was the difference between these two z position. The laser power was then increased by 20 mW per reading and the measurements were repeated. The experiment was stopped immediately after the surface was burned by the laser which happened at an average power \approx 240 mW. As shown in Figure 5 - 3 (b), the bubble contact angle was calculated by Eq. (5-3).

$$\theta = \arctan\left(\frac{d_{bb}}{2z_1}\right) \quad \text{Eq. (5-3)}$$

For the measurements on FOTS surface, the first reading of z position was the same as on SiO₂ surface. The second reading of z position was taken by focusing on the top of the bubble. z_2 is the difference between these two readings. The increments of laser power were fixed as 20 mW and the measurements were only taken before the surface was damaged by the laser. The bubble contact angle can be calculated by the first-order derivative of the parabolic curve of the interface as Eq. (5-4).

$$\theta = \pi + \arctan\left(\frac{-4z_2}{d_{bb}}\right) \quad \text{Eq. (5-4)}$$

The measurements for the bubble contact angles are repeated five times for each laser power on each surface and in each tested liquid. The bubble base diameter, bubble diameter, and z positions are average values of five readings.

5.3.2 Uncertainty Analysis

The analysis of experimental uncertainty is based on the propagation of uncertainties.¹¹⁹ The uncertainty analysis expression is Eq. (5-5).

$$E_{\theta} = \sqrt{\left(\frac{\partial\theta}{\partial d_{bb}}\right)^2 E_{d_{bb}}^2 + \left(\frac{\partial\theta}{\partial z}\right)^2 E_z^2} \quad \text{Eq. (5-5)}$$

where $E_{d_{bb}}$ and E_z are the uncertainties d_{bb} and z in respectively.

The uncertainties of $E_{d_{bb}}$ and E_z are obtained from the standard deviation of five readings. Accounting for all instrument errors, in current work, the maximum uncertainties of bubble base diameter, bubble diameter, and z position are 10 μm, 30 μm, and 3 μm in regular water and are 13 μm, 23 μm, and 9 μm in degassed water respectively, translating to a maximum uncertainty of 2.4° (out of ~33°) and 5.2° (out of ~73°) in regular and degassed water respectively.

5.3.3 Experimental Results

Figure 5 - 4, Figure 5 - 5, and Figure 5 - 6 show the bottom view, obtained using an inverted optical microscope, of a single bubble formed on hydrophilic SiO₂ in regular water, on normal SiO₂ in degassed water and on FOTS in degassed water, respectively, with increasing laser heating power. The vapor bubble achieves steady-state in degassed DI water in a few seconds as the heat transfer from the surface leads to continuous evaporation of water in the microlayer which is balanced by the continuous condensation of vapor at the liquid-vapor interface away from the surface due to the sub-cooled pool of water (temperature of water was ≈ 75 °C lower than the saturation temperature ≈ 100 °C).

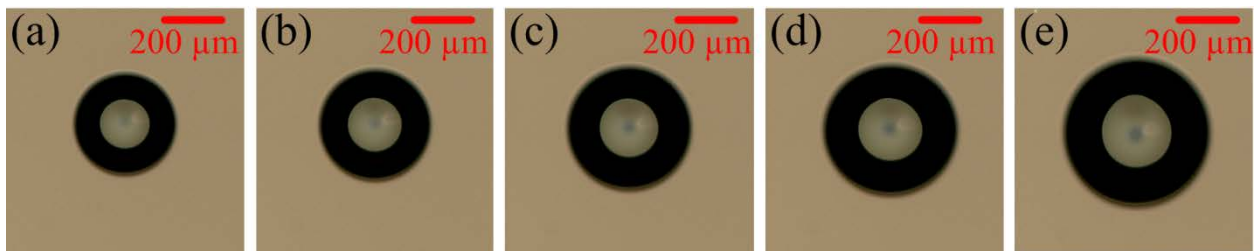


Figure 5 - 4 Images of a bubble on normal SiO₂ in regular water at different laser power (a) 120 mW (b) 140 mW (c) 160 mW (d) 180 mW (e) 200 mW

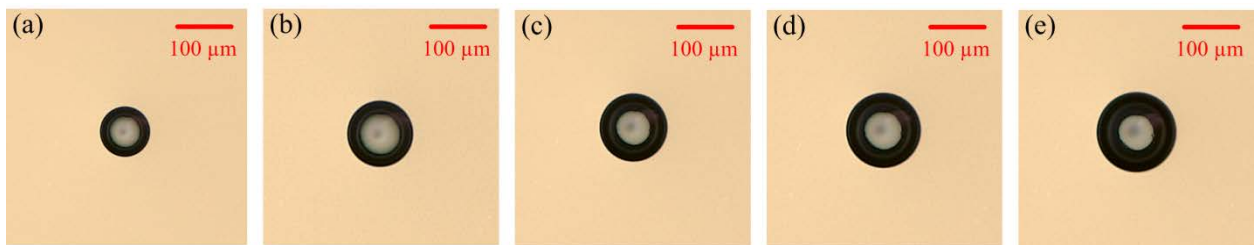


Figure 5 - 5 Images of a bubble on normal SiO₂ in degassed water at different laser power (a) 120 mW (b) 140 mW (c) 160 mW (d) 180 mW (e) 200 mW

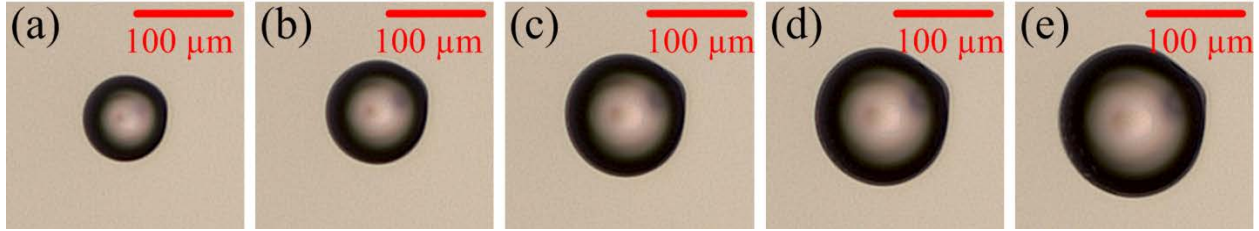


Figure 5 - 6 Images of a bubble on FOTS in degassed water at different laser power (a) 120 mW (b) 140 mW (c) 160 mW (d) 180 mW (e) 200 mW

Figure 5 - 7 shows the variation in the bubble base/bubble diameter with increasing laser power for the various cases studied. The bubble sizes were consistently smaller in degassed DI (D) water when compared to regular DI (R) water due to the contribution of dissolved air in the bubble growth phenomenon in regular water. This effect was further confirmed by turning the laser off; the bubble in degassed DI water disappeared quickly (due to condensation of vapor) while the bubble in regular DI water decreased in diameter slightly but stayed on the surface for days. It is also consistent with recent investigations¹⁴²⁻¹⁴⁶ where air nanobubbles were found to be stable for days due to the slow-rate of dissolution of air into an already saturated surrounding liquid.

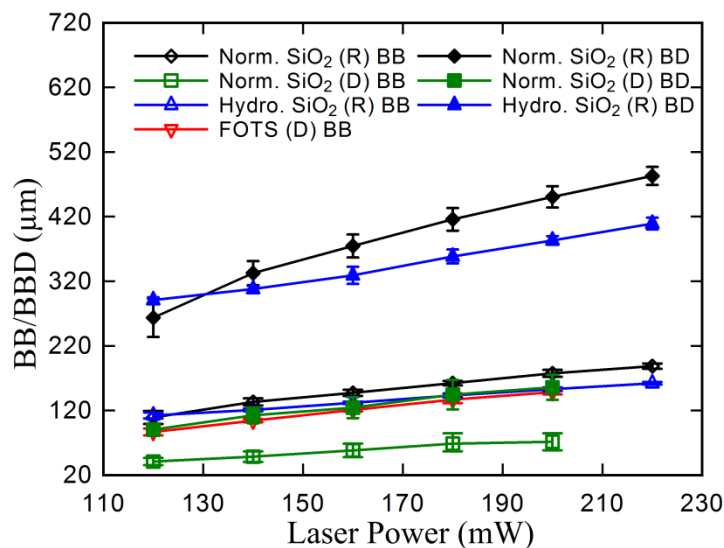


Figure 5 - 7 Bubble base diameter and bubble diameter

Figure 5 - 8 and Figure 5 - 9 show the results of the bubble contact angle on various surfaces in regular water and degassed water respectively. For the normal SiO₂ surface with degassed water, the bubble contact angle decreased with increasing laser power (from 73.6° ± 3.9° at 120 mW to 45.3° ± 5.2° at 200 mW). In all the other cases, the bubble contact angle was found to be independent of the laser power studied. The average bubble contact angle in regular water was determined to be 31.9° ± 0.5° on normal SiO₂ surface, which is similar to the drop contact angle (Table 5 - 1), and consistent³⁷ with the drop receding contact angle after boiling experiments (32.3° ± 0.4°). The average contact angle was 29.3° ± 0.4° on the hydrophilic SiO₂ surface which is slightly smaller than the bubble contact angle on the normal SiO₂ surface. The contact angle of the bubble on the FOTS surface was 96.8° ± 0.2° which is also similar to the measured drop contact angle. These variations in contact angles, especially between degassed and regular water on the same surface, depend on the dynamics of the microlayer and contact line region as studied and explained in section 5.4.3.

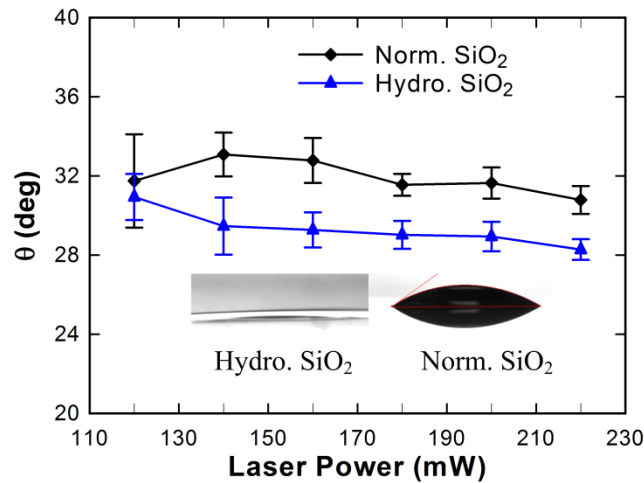


Figure 5 - 8 Bubble contact angles on the hydrophilic surface

Figure 5-1

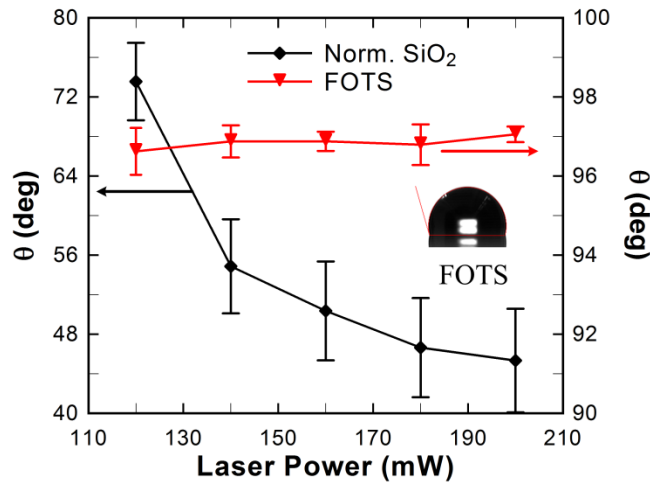


Figure 5 - 9 Bubble contact angle on the hydrophobic surface

5.4 Microlayer underneath the Steady Bubble

5.4.1 Fringe Patterns

A stable bubble enables *in-situ* imaging of the contact line region present at the base of the bubble. The bubble was formed using a femtosecond laser illumination through a 50× microscope objective. When a coherent light source (such as laser) goes through a wedged thin liquid layer, as shown in Figure 5 - 10, interference patterns (alternate bright and dark rings) would appear due the refraction and reflection at the upper surface of the liquid layer, which is the microlayer in this case.

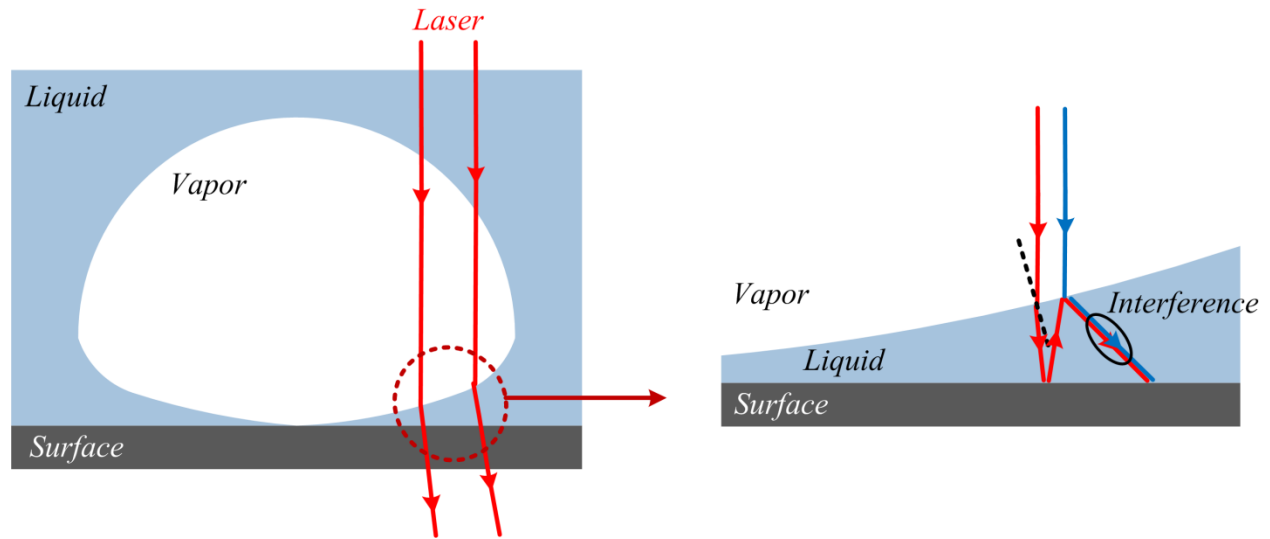


Figure 5 - 10 Optical paths for laser interferometry

Under coherent HeNe laser illumination, two sets of fringes were observed in the images that are a result of thin-film interference associated with the interaction between regions of different refractive index. The first set of fringes, F-1 (dark thick partial rings), have fringe-gaps decreasing in the outward radial direction and are associated with interference resulting from the top curved interface of the bubble (and not due to the contact line region). The second set of fringes, F-2, are relatively closely packed and the fringe-gap for these set of fringes increase in the outward radial direction. These fringes are the result of thin-film interference of incident light with the partially reflected light within the thin liquid microlayer, which is present at the base of the bubble.²¹ The increase in fringe-gap was attributed to the increase in radius-of-curvature of the microlayer in the outward radial direction.

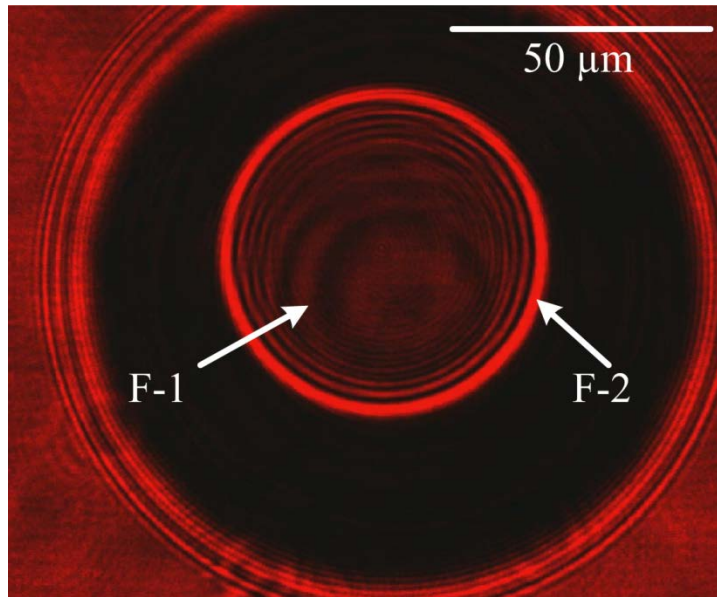


Figure 5 - 11 Typical fringe patterns

5.4.2 Microlayer Profile

To obtain *in-situ* images of the contact line region, bubbles were formed on a normal SiO_2 (Figure 5 - 12 (a)) surface with regular water, a normal SiO_2 surface with degassed water (Figure 5 - 12 (b)), and a FOTS surface with degassed water (Figure 5 - 12 (c)). The contact line region is imaged (Figure 5 - 12) using the inverted optical microscope under illumination from both a white halogen lamp source (Figure 5 - 12 (a1), (b1), and (c1)) and a 632 nm HeNe laser (Figure 5 - 12 (a2), (b2), and (c2)). The microlayer shapes obtained for a bubble on the normal SiO_2 in regular water and degassed water, and on FOTS surface in degassed water is plotted in Figure 5 - 12 (a3), (b3), and (c3) respectively. As the interference of the monochromatic light source generates dark and bright fringes corresponding to constructive and destructive interference respectively, these fringes are separated by an optical path difference equal to the effective half wavelength, $n\lambda_0/2$, where n is the refractive of the medium, λ_0 is the free-space wavelength of light. The position of these fringes is used to construct the shape of the microlayer, where the

difference in local thickness at the adjacent bright/dark fringe location t_{m+1} and t_m is given by Eq. (5-6) for the light refracted at angle θ into the microlayer.

$$t_{m+1} - t_m = \frac{\lambda_0}{2n\cos(\theta)} \quad \text{Eq. (5-6)}$$

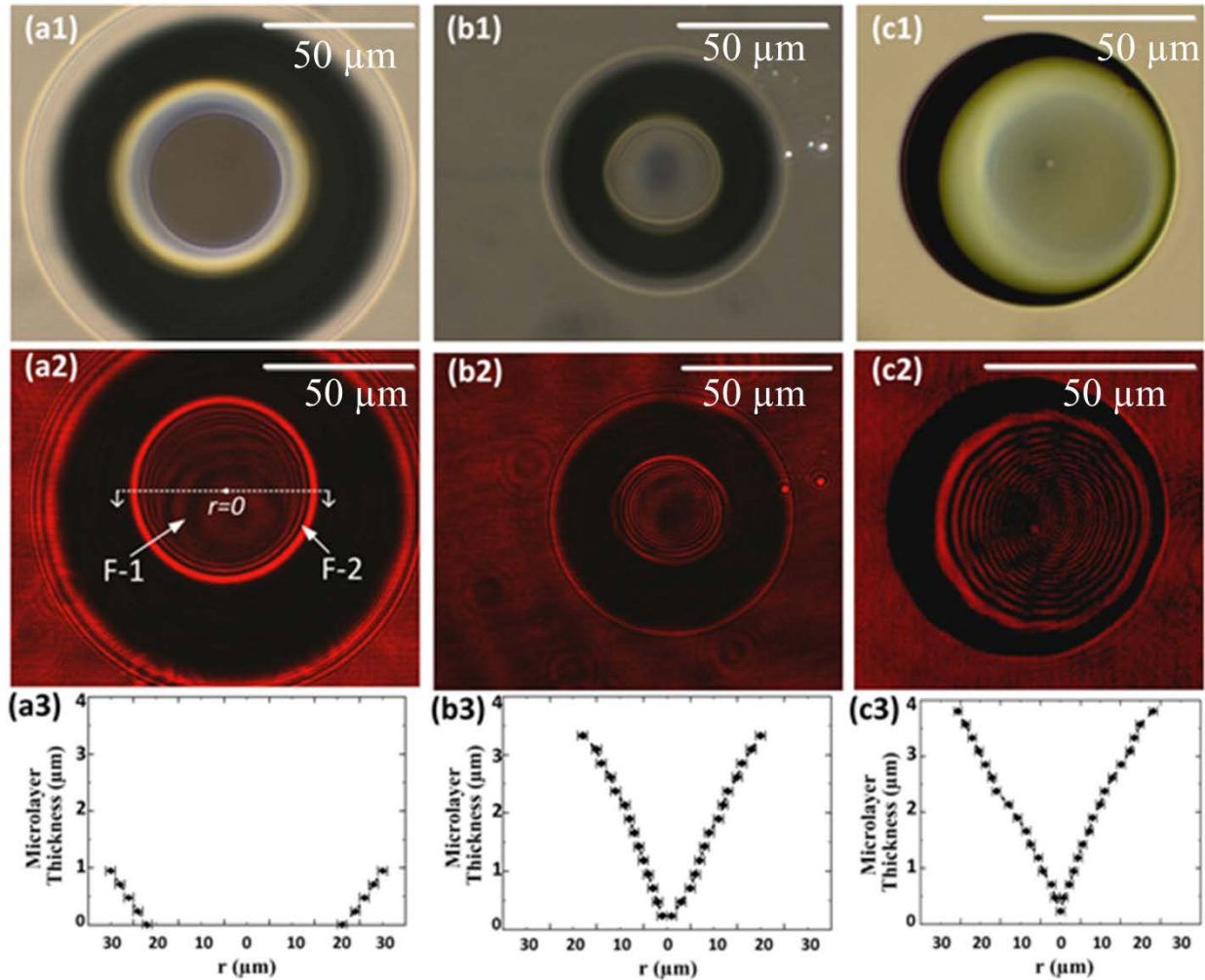


Figure 5 - 12 Optical images of the bubble with 50× magnification under white-light and HeNe laser illumination and microlayer profile (a) bubble on normal SiO₂ surface in regular water (b) bubble on normal SiO₂ surface in degassed water and (c) FOTS surface in degassed water

The second set of fringes is clearly evident in degassed DI water (Figure 5 - 12 (b2) and (c2)) showing the presence of a liquid microlayer over the entire bubble base. However, in regular DI water (Figure 5 - 12 (a2)), the fringes are absent from the center of the bubble base and are only

present in the equivalent bright regions of Figure 5 - 12 (a1). This observation implies the presence of a dry-spot region at the center of the bubble base and the formation of the three-phase contact line region (liquid-vapor-solid) interfacing with the SiO₂ surface, with a significantly reduced microlayer.

The bubble formation in regular water was recorded by a high speed camera. Figure 5 - 13 shows the dynamic process of evolution of the microlayer. When the bubble is small, the microlayer covers the entire bubble base (Figure 5 - 13 (a) and (b)). As the bubble increases in size, the microlayer decreases in thickness until a central dry spot and three-phase contact line form (Figure 5 - 13 (c)).

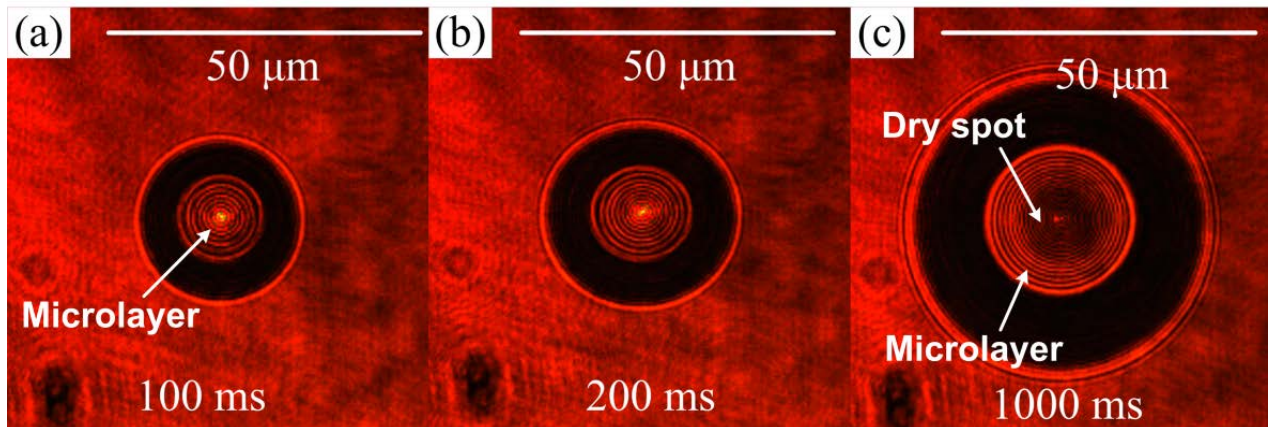


Figure 5 - 13 Evolution of the microlayer with bubble growth

5.4.3 Effect of Microlayer on Bubble Contact Angle

The fringes observed in the contact line region are also used to explain the experimentally measured contact angle values. In the regular DI water on the normal SiO₂ surface, the larger size of the bubble (due to contribution of dissolved air) at low laser power creates a dry spot at the center causing the creation of a three-phase contact line; hence, the bubble contact angle is similar to the drop contact angle (where a similar three-phase contact line is present). However,

with degassed DI water on the normal SiO₂ surface, the microlayer covers the entire bubble base preventing the formation of the three-phase contact line, and the contact angle is governed by the microlayer curvature relative to the bubble curvature. Hence, the contact angle decreases with increasing laser power as the radius of the curvature of the microlayer increases significantly faster compared to the radius of curvature of the bubble. Similarly, in FOTS, the larger radius of the curvature microlayer along with the parabolic bubble shape, results in large contact angle values. The parabolic shape of bubble is attributed to the larger bubble base diameter as the reduced wettability of the hydrophobic surface requires a larger microlayer to remove the same amount of heat from the surface. However, for degassed DI water on both normal SiO₂ and FOTS surfaces, it is expected that after a critical bubble size is reached, – the microlayer would reduce in thickness and form the three-phase contact line; the bubble contact angle would also be expected to converge to that of the drop contact angle.

5.4.4 Steady Bubble with Completely Wetted Base

Two kinds of bubbles were observed with laser heating. As shown in Figure 5 - 14, the microlayer covers the entire bubble base area initially. Increasing heating temperature and bubble size forms a three-phase contact line with the reduced microlayer, showing the non-evaporating region (R3), the evaporating film region (R2), the bulk meniscus region (R1) and the dry spot (R4); the microlayer comprises regions R1, R2 and R3. Further, bubbles with the microlayer wetting the entire bubble base will not depart the surface as the capillary suction force (due to reduced liquid pressure in microlayer) is orders of magnitude larger than the buoyancy force. From Figure 5 - 12 (b2), the vapor bubble volume is estimated to be $3.30 \times 10^{-13} \text{ m}^3$, resulting in a buoyancy force of $3.23 \times 10^{-9} \text{ N}$. The curvature of the microlayer can be approximated to be $0.02 \text{ } \mu\text{m}^{-1}$ from Figure 5 - 12 (b3), resulting in a reduction in microlayer

liquid pressure of 2880 Pa. Estimating the bubble base radius to be 40 μm , the capillary suction force equals 3.62×10^{-6} N. Disjoining pressure will also further reduce the liquid pressure of the microlayer, thus enhancing this effect.

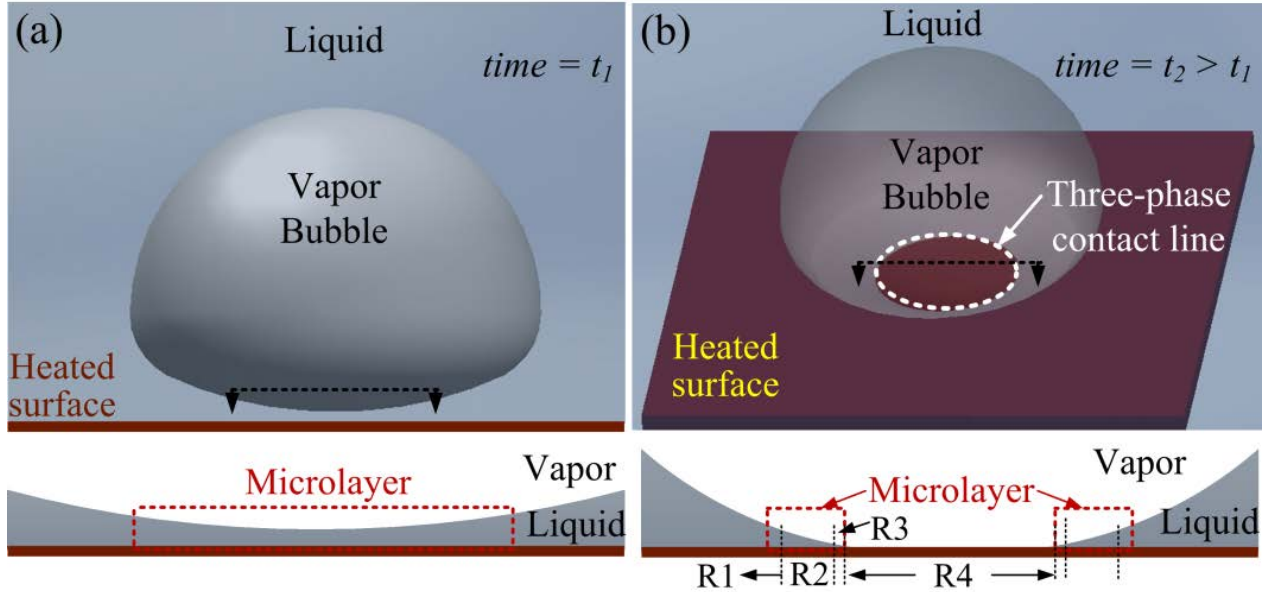


Figure 5 - 14 Two types of bubble (a) a bubble with a microlayer wetting the entire bubble base (b) a bubble with three-phase contact line: non-evaporating region (R3), evaporating film region (R2), bulk meniscus region (R1) and the dry spot (R4)

5.5 Heat Transfer Characteristics in Evaporating Region

5.5.1 Bubble Growth Rate in Regular Water

When forming a bubble in regular DI water on the normal SiO_2 surface, it was found that the bubble grew gradually with a constant laser power. In order to obtain the bubble volumetric rate, it is divided into two parts (Figure 5 - 15): top part I is a hemisphere; the curve of lower part II is a partial parabolic curve, the equation of which can be found by bubble base diameter d_{bb} and corresponding height z of bubble middle plane as Eq. (5-7).

$$y = \frac{1}{4z}x^2 - \frac{d_{bb}^2}{16z}, \quad x \in \left(-\frac{d_{bd}}{2}, -\frac{d_{bb}}{2}\right) \cup \left(\frac{d_{bb}}{2}, \frac{d_{bd}}{2}\right) \quad \text{Eq. (5-7)}$$

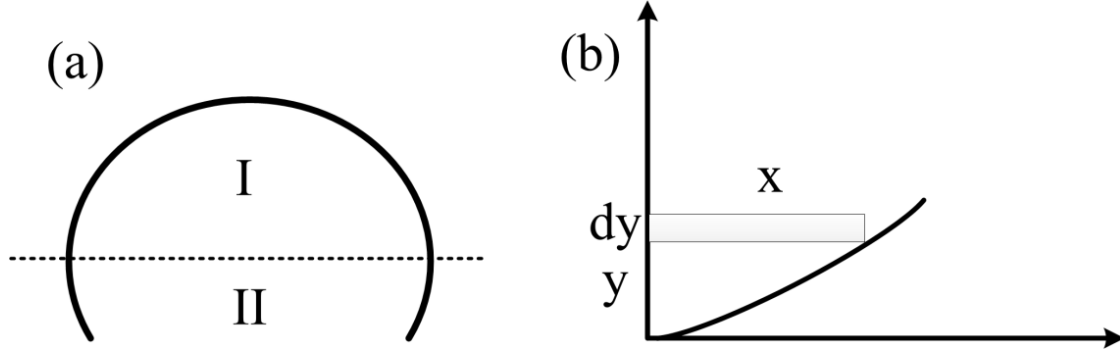


Figure 5 - 15 Calculation of bubble volume

The volume of top part I is Eq. (5-8).

$$V_I = \frac{1}{12} \pi d_{bd}^3 \quad \text{Eq. (5-8)}$$

For an infinite element in lower part II, the volume is $\pi x^2 \cdot dy$. Thus, the volume of part II is Eq. (5-9).

$$V_{II} = \int_0^z \pi(4zy + \frac{d_{bb}^2}{4}) dy = \pi z(2z^2 + \frac{d_{bb}^2}{4}) \quad \text{Eq. (5-9)}$$

Finally, the bubble volume is the sum of part I and part II as Eq. (5-10).

$$V = \frac{1}{12} \pi d_{bd}^3 + \pi z(2z^2 + \frac{d_{bb}^2}{4}) \quad \text{Eq. (5-10)}$$

The volumetric rate was obtained by plotting the bubble volume verses time and is adopted from the linear regression. The bubble grew steadily at a volumetric rate of $(5.60 \pm 0.06) \times 10^{-3}$ mm³/min (Figure 5 - 16) and the contact line region at the bubble base grew radially outward at a speed of (1.9 ± 0.1) μm/min during the initial 40 min, but stopped after it reached a diameter of ≈ 270 μm (Figure 5 - 17); this limiting diameter approximately corresponds to the measured laser beam diameter (≈ 170 μm) with additional radial heat conduction in the Au layer. The uncertainty in the measurements of the bubble growth rate and bubble base is standard deviation of the fit parameter. The contact angle of the bubble (Figure 5 - 18) decreased with time as the

bubble base remained nearly constant while the bubble diameter grew uninhibited. Similar to Figure 5 - 12 (a1), the central dry spot diameter was identified from *in-situ* imaging of the contact line region.

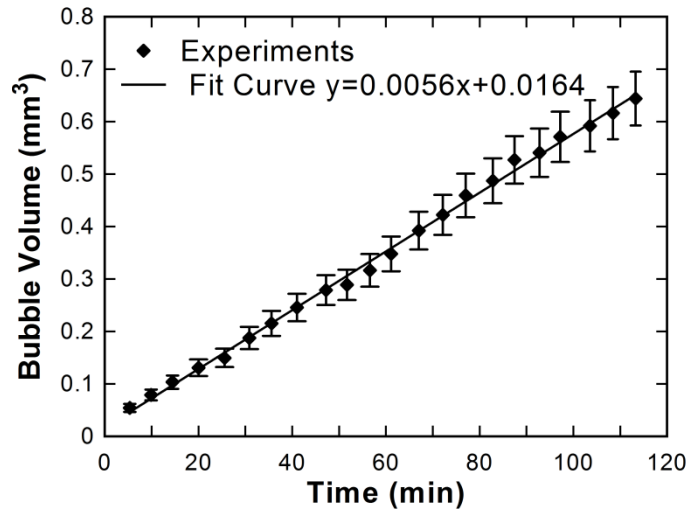


Figure 5 - 16 Bubble volume growth with constant laser power

Figure 5-2

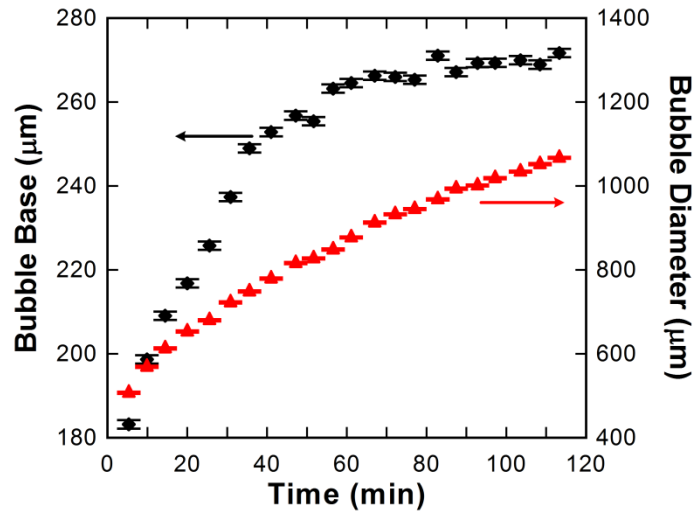


Figure 5 - 17 Bubble diameter and base growth with constant laser power

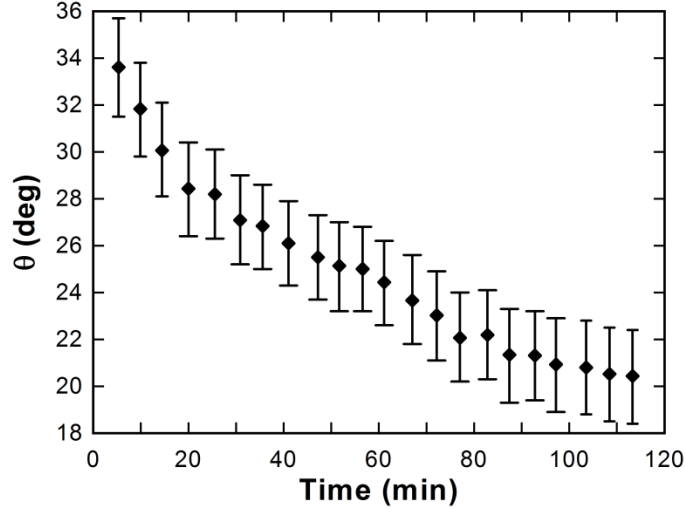


Figure 5 - 18 Contact angle evolution with constant laser power

5.5.2 Heat Transfer Coefficient in Evaporating Region

Maximum heat flux occurs in the thin evaporating region¹⁹ and is of critical importance in bubble growth dynamics; however, knowledge of the heat transfer coefficient and corresponding width of this region is currently lacking in the literature. By using experimental data from *in-situ* imaging of the contact line region, finite-element-method based numerical simulations were conducted to characterize the evaporating region in the microlayer.

Based on these experimental data, the heat transfer rate q in the evaporating region can be obtained from the air-water solubility mass balance calculation as Eq. (5-11).

$$q = \dot{m}_{water} h_{lv} = \left(\frac{\dot{m}_{water}}{S_a} \right) h_{lv} \quad \text{Eq. (5-11)}$$

where \dot{m}_{water} is the vaporization rate of water in the evaporating region, \dot{m}_{air} is the mass flow rate of air into the vapor bubble from the evaporating region, and S_a is the solubility of air in water, which is 0.023 g/kg at room temperature.¹⁴⁷

On the other hand, the heat transfer rate in the evaporating region q is also dependent on the overall heat transfer coefficient h and the area of the evaporating region through Eq. (5-12).

$$q = h(\pi d_{bb} w) \Delta T \quad \text{Eq. (5-12)}$$

where w is the width of the evaporating region, and ΔT is the temperature difference between the surface and the bulk fluid. Unknown parameters h and w characterize the evaporating region and finite-element-method based simulations were performed to determine the range of h and w for which the simulated release rate of air from the evaporating region agreed with that obtained through measured bubble geometry in the experiments (Figure 5 - 16). An axi-symmetric domain (Figure 5 - 19) was considered that included the glass substrate, 40 nm Au layer and 400 nm SiO₂ layer. A parametric study was then performed where h and w were varied from 5000 Wm⁻²K⁻¹ to 200,000 Wm⁻²K⁻¹, and from 0.5 μm to 19.5 μm, respectively for a total of 3500 simulation cases.

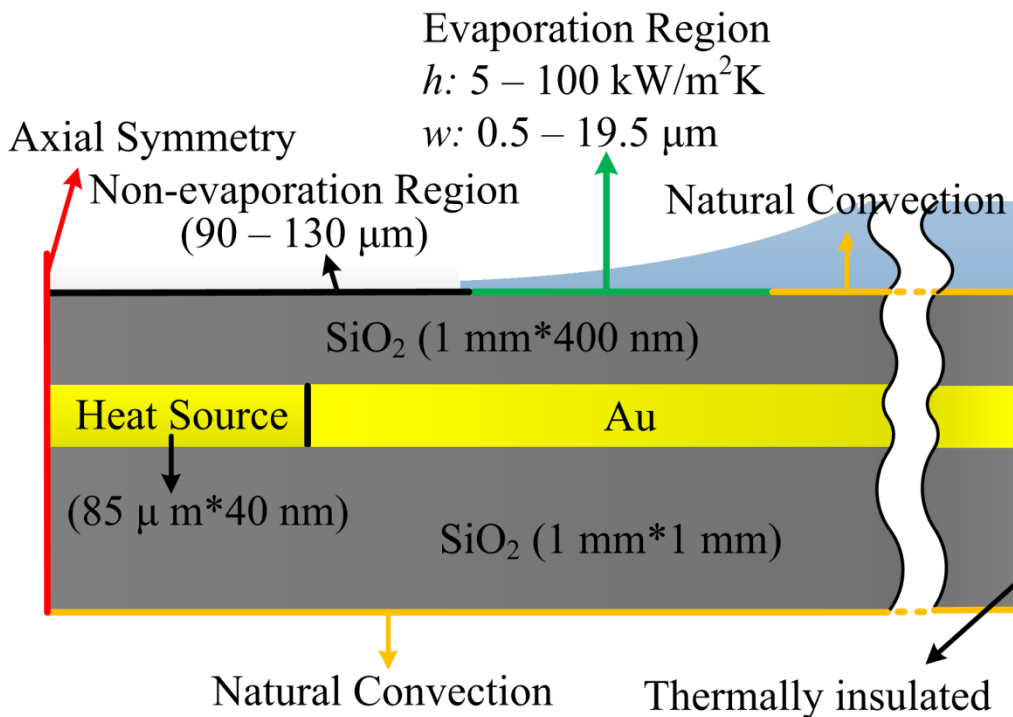


Figure 5 - 19 Simulation domain

Figure 5 - 20 shows the range of h and w for which simulation results were in good agreement with experiments within a standard uncertainty of 4.5 %.

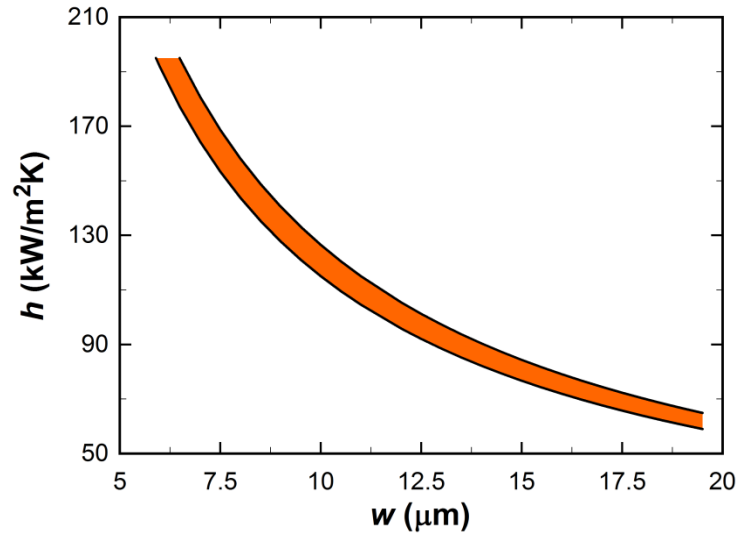


Figure 5 - 20 Approximation of heat transfer coefficient and width of evaporating region

The temperature profile of the surface is plotted for this range (Figure 5 - 21). Interestingly, the surface temperature at $r \approx 135 \mu\text{m}$ was $\approx 39^\circ\text{C}$, which is the critical temperature when Marangoni flow inhibits fluid flow towards the contact line,¹⁴⁸ thus equilibrating the incoming mass flow to the evaporation rate and causing the contact line to become stable at the bubble base diameter of $\approx 270 \mu\text{m}$. The temperature at the center of the bubble is calculated to be $\approx 82^\circ\text{C}$, which is also in good agreement with experiments,¹⁴⁹ where it has been shown that the formation of an air bubble in pool boiling in sub-cooled water at room temperature occurs at $\approx 84^\circ\text{C}$.

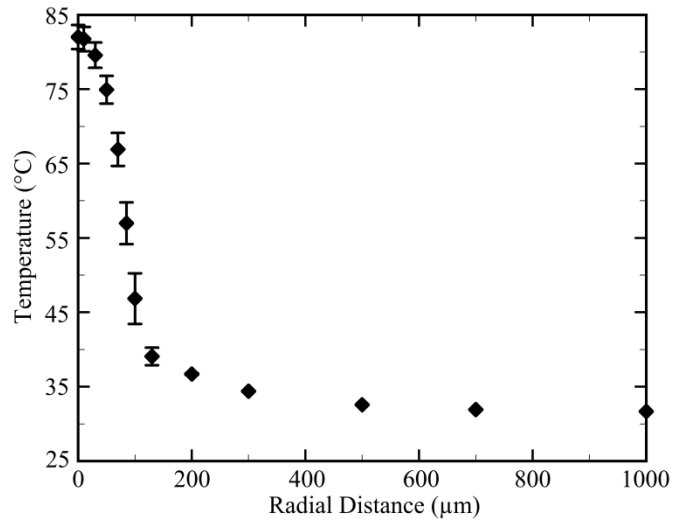


Figure 5 - 21 Surface temperature profile

5.6 Summary

In summary, a steady-state vapor bubble was created in a pool of sub-cooled water by femtosecond laser heating which allows for *in-situ* imaging of the microlayer and the contact line regions. The bubble can remain stable for hours as the evaporation of water at the surface is balanced by the condensation of vapor at the liquid-vapor interface inside the bubble. Experiments were conducted on hydrophilic (SiO_2) and hydrophobic (FOTS) surfaces in regular (with dissolved air) and degassed DI water. The contact angle of the vapor bubble was measured for various cases, and the microlayer and contact line region were imaged with white light and a coherent laser source. For the laser powers studied, it was found that the three-phase contact line readily forms in regular DI water, while the microlayer covers the entire bubble base in degassed DI water. The contact angle for the bubble was found to resemble the drop contact angle on the same surface if the three-phase contact line forms, otherwise the contact angle is dependent on the curvature of the microlayer and the bubble, and decreases with increasing laser power. The evaporating region in the contact line region was characterized by numerical simulations and

experimental results, and permissible values of the heat transfer coefficient and corresponding width were calculated, thus providing an estimate to the upper limit of the heat transfer coefficient attainable in nucleate boiling as well as thin-film evaporation. The work in this chapter will advance the design of nanostructures to enhance heat transfer by optimizing the width of microlayer, and improve the understanding of the boiling phenomenon in outer-space where the lack of gravity causes the bubbles to stay stationary on a heated surface. *In-situ* imaging of the microlayer and contact line region in a steady state bubble is a powerful technique for understanding the physical dynamics of the bubble growth process.

6. Contact Line Behavior of a Vapor Bubble

6.1 Introduction

The fundamental behavior of the three-phase contact line is essential for understanding the boiling heat transfer mechanism, CHF triggering mechanism,^{150,151} and for prediction of CHF.^{152,153} The thermodynamic and hydrodynamic interactions in the contact line region have been investigated.¹⁵⁴ However, most of the investigations were based on the application of meniscus evaporation in heat pipes.¹⁵⁵⁻¹⁵⁸ The handful of studies focused on the three-phase contact line region in pool boiling were conducted by both numerical and experimental methods. Son *et al.*¹⁵⁹ obtained the dynamics and heat transfer associated with a single bubble in nucleate boiling by implementing three-phase contact line model²⁹ into a level-set framework. Kunkelmann *et al.*^{160,161} simulated pool boiling using a numerical volume-of-fluid method. They found that the local heat transfer rate in the contact line region was strongly affected by the direction of contact line movement (receding or advancing) and the speed of this movement. The influence of contact line on heat transfer was also observed experimentally,^{28,162} where boiling was conducted in microgravity condition and the bubble base grew to $\sim 300 \mu\text{m}$ in the first 5 ms of nucleation. Further, during a complete bubble ebullition cycle, the liquid flows constantly from the bulk meniscus region to the evaporating region. The liquid flow rate depends on the gradients of the capillary pressure and the disjoining pressure in the evaporating region, both of them governed by the film thickness profile.^{163,164} However, the knowledge on contact line behavior (including contact line motion and the evolution of the film profile) during bubble formation and movement is still lacking, especially for a bubble in its early growth stage.

In this chapter, a vapor bubble was created using the laser heating method introduced in section 5.2.2. The bubble and three-phase contact line movement was achieved by moving the laser beam to change the heating location on the sample. The contact line motion and the evolution of the thin film profile were recorded by a high speed camera. The effect of surface wettability on contact line motion was investigated by conducting experiments on hydrophilic surface (SiO_2 with the drop contact angle of $33.4^\circ \pm 2.7^\circ$) and hydrophobic surface (FOTS with the drop contact angle of $109.8^\circ \pm 2.9^\circ$) respectively.

6.2 Experimental Methods

The sample fabrication follows the procedure explained in the section 5.2.1. The experimental setup and sample preparation are exactly the same as described in the section 5.2.2. A 50× microscope objective was used to focus the laser beam on the sample to form the bubble. The same objective was also used for imaging the bubble to observe the bubble contact line behavior and evolution of the microlayer during bubble growth and movement. All experiments were performed in the regular DI water with dissolved air as the entire bubble base would be covered by the microlayer and the contact line would not form in degassed water (due to the small bubble size).

6.3 Contact Line Behavior in Bubble Formation and Growth

Figure 6 - 1 shows the process of bubble formation and growth with laser heating. In the figures, the yellow dotted line represents the laser beam, which is a circle with the diameter of $\sim 11 \mu\text{m}$; the white dotted line is the contact line. The fringe pattern shows the microlayer. The first bubble image captured by the high speed camera (0.25 ms) has a bubble base with the diameter of $\sim 11 \mu\text{m}$, the same as the laser beam. The fringe patterns show up 3 ms after the nucleation,

representing the formation of the microlayer. It covers the entire bubble base initially. Both the bubble base and bubble diameter expand and the microlayer grows (Figure 6 - 1 (a-b)). A dark region shows up at ~500 ms and the region keeps growing as bubble grows. The fringe pattern still appears in this region but fades out gradually (Figure 6 - 1 (c-d)). It disappears completely at the center of the bubble base at ~2000 ms when the bubble diameter grows to ~60 μm , which depicts the formation of a dry region at the center of the bubble base, and thus the formation of the three-phase contact line. The contact line expands outward at an average speed of 0.004 $\mu\text{m}/\text{ms}$ between 3000 ms and 5000 ms (Figure 6 - 1 (e-f)).

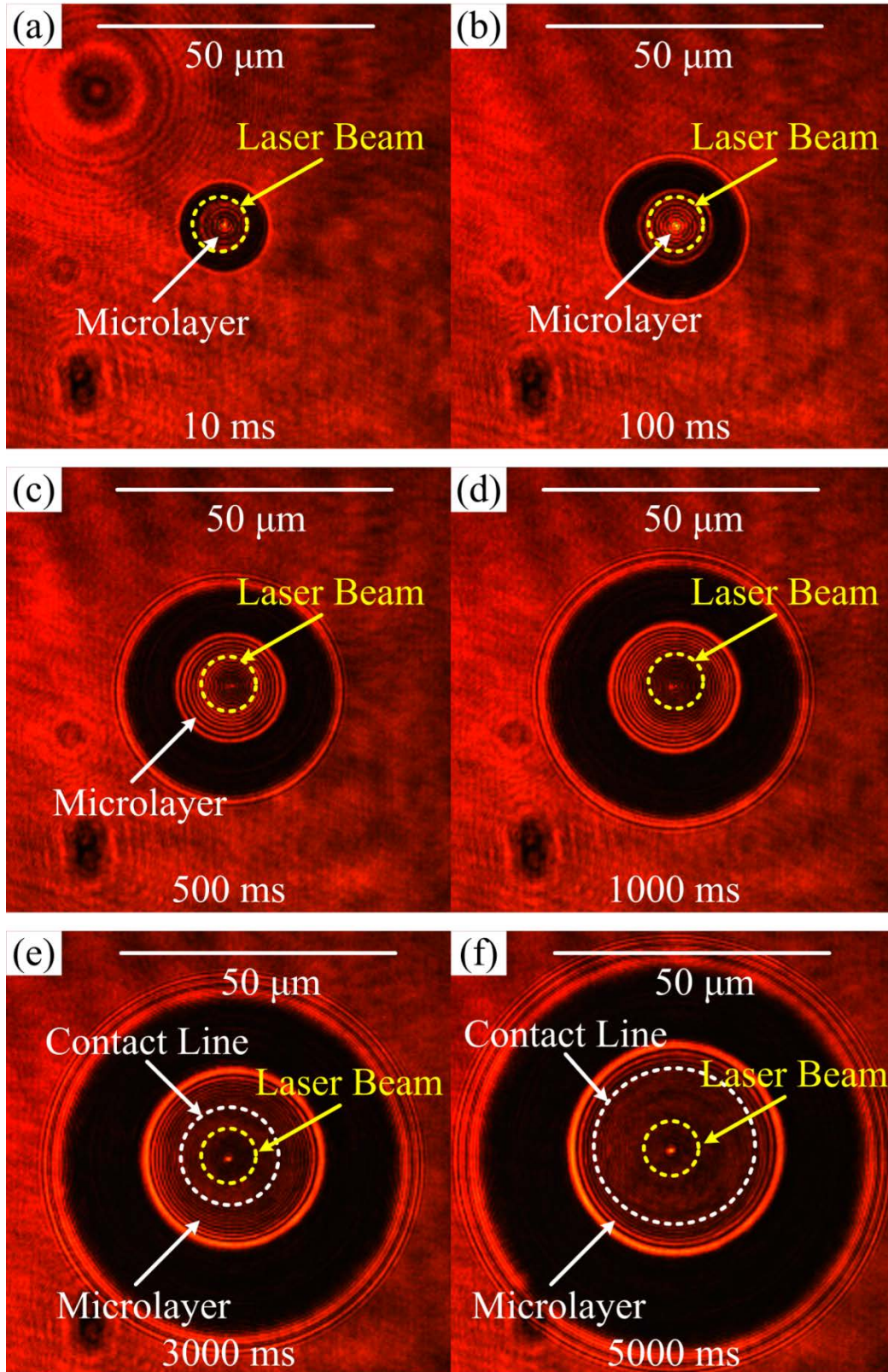


Figure 6 - 1 Contact line behavior during bubble formation and growth

6.4 Contact Line Behavior in Bubble Movement

The surface wettability strongly influences behavior and movement of the contact line. On the hydrophobic FOTS surface, as the laser beam is moved close to contact line region, the microlayer in that region evaporates and the dry spot expands (the shape of contact line changes). As the laser beam is moved continuously, the contact line sticks on the surface, leading the bubble to stay on its original location. While on the hydrophilic SiO₂ surface, the contact line as well as the entire microlayer moves forward with laser beam (the shape of contact line remains the same), leading to the bubble following the laser beam movement. The effect of surface wettability on contact line behavior is elaborated in the following sections with images recorded from the high speed camera.

6.4.1 Bubble Movement on Hydrophobic surface

Figure 6 - 2 and Figure 6 - 3 show the contact line behavior on FOTS surface with illumination of white and red light respectively. In the figures, the white dotted line shows the contact line of the bubble; the yellow dotted line illustrates the laser beam, which is a circle with diameter of ~11 μm; the white dash-dot line is a reference line to identify the location of the bubble during laser beam movement. Initially, a steady bubble was created and the laser beam is located at the center of the dry region (Figure 6 - 2 (a) and Figure 6 - 3 (a)). The laser beam is then moved to the left. Point *a* is defined as the leftmost point of the contact line (in the direction of laser beam movement), while points *b*, *c*, and *d* are rightmost, top, and bottom position of the contact line, respectively. As the laser beam approaches the contact line region (Figure 6 - 2 (b) and Figure 6 - 3 (b)), one fringe disappears showing decrease in the microlayer thickness. Since the surface is hydrophobic and prevents liquid spreading, fresh liquid replenishment in the microlayer becomes difficult. Once the local evaporation overwhelms the supply of the water, the microlayer

thickness decreases, and eventually evaporates completely. Thus, the dry region expands in the direction of the laser beam movement as point *a* moves to the left while points *b*, *c*, and *d* stay at the original positions. As the laser beam continues to move to the left (Figure 6 - 2 (c) and Figure 6 - 3 (c)), the microlayer in the region of points *a* and *b* evaporates completely and disappears; while it remains at the region near points *c* and *d*. The shape of contact line becomes elliptical due to this uneven expansion. After the local microlayer evaporates completely, point *a* is pushed with laser as the laser beam moves closer, forming an extra triangular dry region (Figure 6 - 2 (d-e) and Figure 6 - 3 (d-e)). Point *a* cannot be pushed further once the laser beam reaches the contact line region and is “pinned” on the surface, similar to points *b*, *c*, and *d* (Figure 6 - 2 (e-g) and Figure 6 - 3 (e-g)). As the laser beam moves out of the dry region, the bubble suddenly shifts to right and the contact line recovers to a circular shape (due to energy minimization) as the laser beam cannot influence the bubble (Figure 6 - 2 (h) and Figure 6 - 3 (h)).

Thus, on the FOTS surface, the microlayer evaporates and the contact line is pushed locally in the direction of the laser beam movement, while the rest of the contact line is pinned on the surface. The local movement of the contact line forms an extra triangular dry region. The bubble shifts to right once the laser beam moves out of the extra dry region to minimize the line tension circumference. In other words, the bubble as a whole “refuses” to follow the laser beam movement as expected due to the hydrophobicity of the surface.

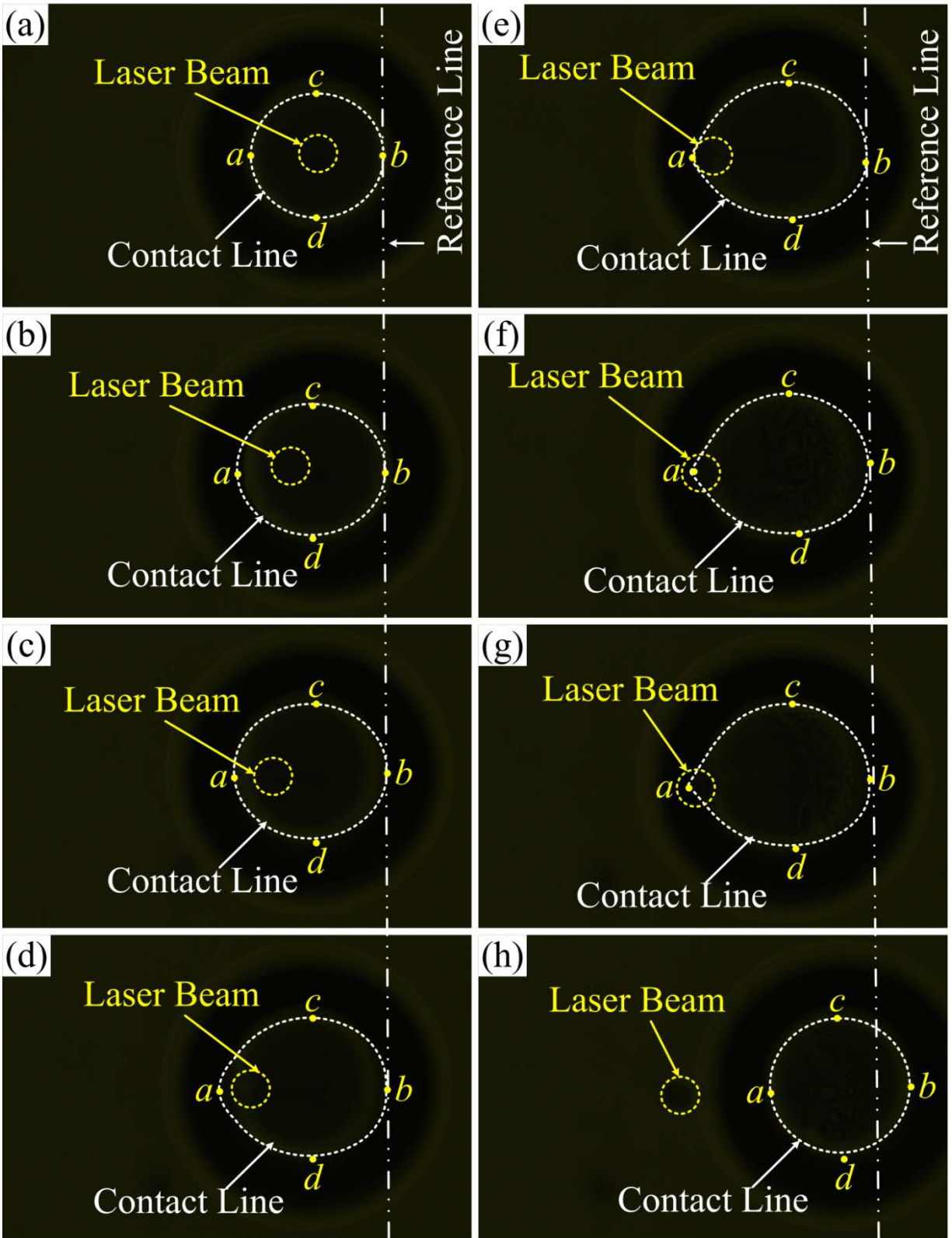


Figure 6 - 2 Contact line behavior on FOTS surface with white light

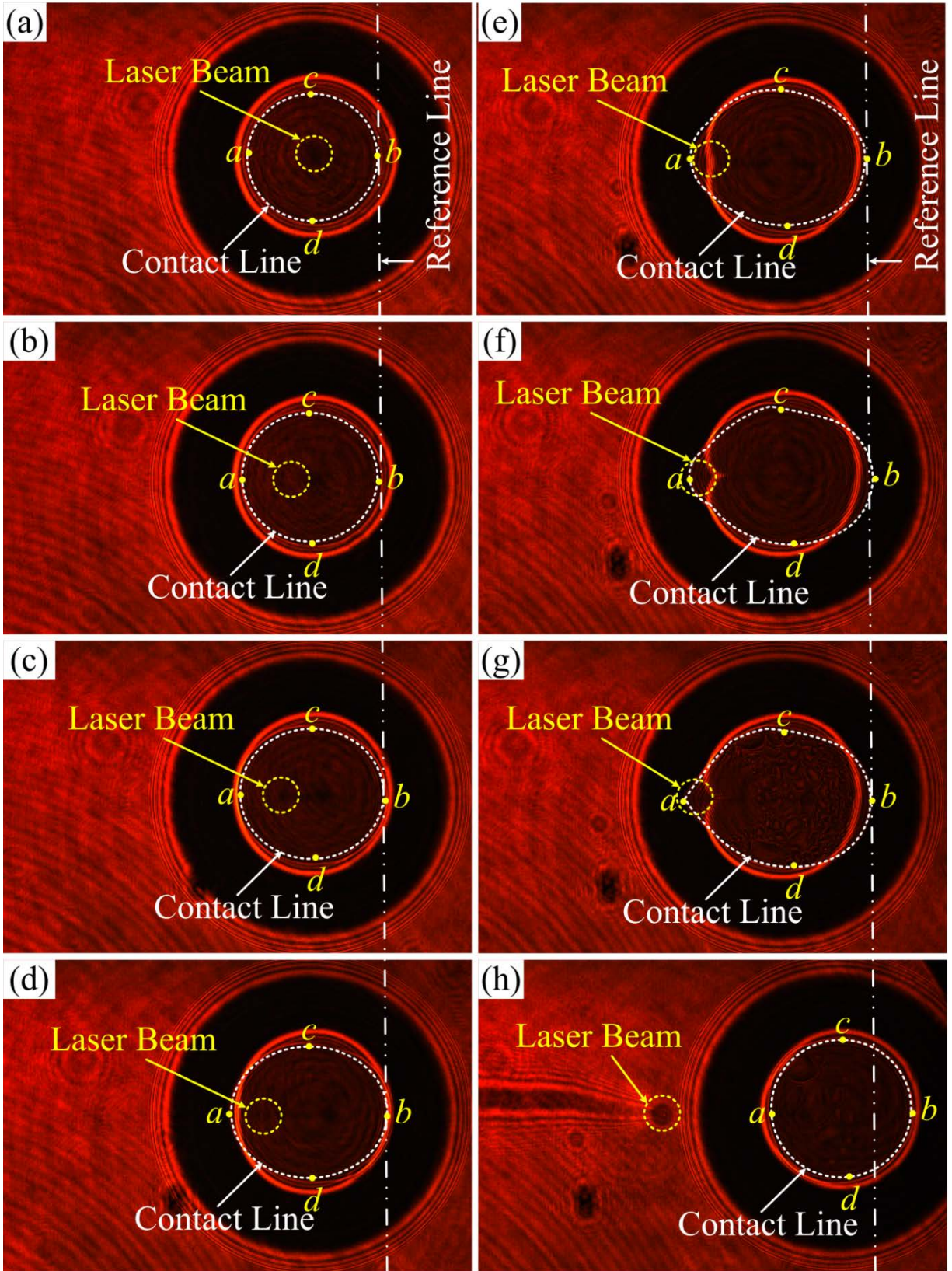


Figure 6 - 3 Contact line behavior on FOTS surface with red light

The reason why the bubble does not follow the laser movement can be explained by surface tension forces exerted on the bubble base, especially at the points *a* and *b*. Figure 6 - 4 shows the change of direction of the surface tension force at the point *a*. The bubble is not in parabolic shape as shown in Figure 5 - 3 because the 50X objective was used to create the bubble and image the microlayer. The laser beam size is around ~11 μm , smaller than bubble base diameter (~50 μm); while in bubble contact angle measurement, 5X objective was used and the laser beam size is ~170 μm , which is larger than bubble base diameter (86 – 150 μm for the laser power studied). As shown in Figure 6 - 4 (a), before the laser moves, the bubble is in the equilibrium state. The force balance in horizontal direction can be expressed as Eq. (6-1).

$$\sigma_{sv} = \sigma_{sl} + \sigma_{lv}\cos(\theta_1) \quad \text{Eq. (6-1)}$$

As the laser beam approaches the contact line region, shown in Figure 6 - 4 (b), the local microlayer evaporates completely and the contact line gets pushed forward to form the extra dry region. The contact angle changes from θ_1 to θ_2 . The direction of the liquid-vapor surface tension force changes as it is the tangential of the interface. This change disrupts the previous force balance, resulting in a net force *F* in horizontal direction (taking the direction of the laser beam movement as positive), as in Eq. (6-2).

$$F = \sigma_{sl} + \sigma_{lv}\cos(\theta_2) - \sigma_{sv} \quad \text{Eq. (6-2)}$$

By substituting Eq. (6-1) to Eq. (6-2), the net force can be expressed as a function of liquid-vapor surface tension and contact angles θ_1 and θ_2 (Eq. (6-3)).

$$F = \sigma_{lv}\cos(\theta_2) - \sigma_{lv}\cos(\theta_1) \quad \text{Eq. (6-3)}$$

Because $\theta_2 > 90^\circ$ and $\theta_1 < 90^\circ$, the net force *F* in Eq. (6-3) is always negative, implying that there is a force exerted on the point *a* to inhibit the contact line to move with the laser.

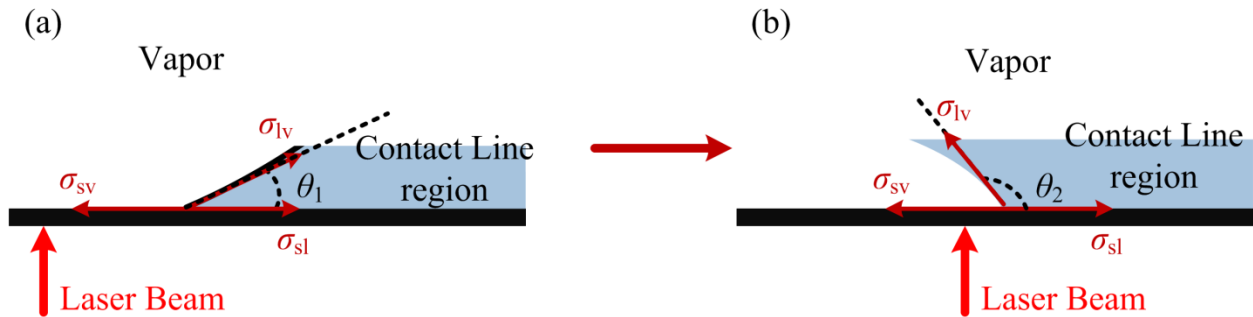


Figure 6 - 4 Change of direction of surface tension at point *a* on FOTS surface

Thus, on hydrophobic FOTS surface, the net force exerted on points *a* is negative, hindering the bubble to move with the laser. However, the evaporation momentum force acts on the bubble base, pushing the contact line to move with the laser. Thus, the bubble stays in its original position due to the balance between the pushing force (evaporation momentum force) and holding force (net force due to the direction change of liquid-vapor surface tension). After the laser moves outside the contact line region, these forces disappear and the balance is interrupted. Energy minimization of the line tension energy causes the bubble base to recover to its original circular shape (Figure 6 - 2 (h) and Figure 6 - 3 (h)) and the bubble reaches the equilibrium state again.

6.4.2 Bubble Movement on Hydrophilic Surface

Figure 6 - 5 and Figure 6 - 6 show the contact line behavior on SiO₂ surface with laser movement under illumination of white and red light respectively. In the figures, the white dotted line represents the contact line of the bubble; the yellow dotted line illustrates a ~11 μm laser beam; the white dash-dot line is a reference line to show the location of the bubble during laser beam movement. Initially, a steady bubble stays on the surface with the laser beam located at the center of dry region. Adjacent to the dry region, the microlayer was observed as a bright annulus under white illumination and circular fringes under red illumination (Figure 6 - 5 (a) and Figure 6

- 6 (a)). The laser beam is moved to left. a , b , c , and d are the leftmost, the rightmost, the top, and the bottom points of the contact line respectively. As shown in Figure 6 - 5 (b) and Figure 6 - 6 (b), when the laser beam approaches to the point a , one fringe disappears in that region and the contact line is pushed forward. Different from contact line behavior on FOTS surface where only a small local part of contact line is pushed forward forming an extra triangular dry region, the left half (~50%) of the contact line is pushed forward. However, the right half stays at its original location. The entire contact line expands to a ellipse-like shape. As the laser continues to move left, the number of fringes at region a maintains the same, implying the equilibrium state between the evaporation and supply of fresh liquid. On the other hand, at the point b , the liquid rewet the surface and the contact line moves forward. The entire contact line is elliptical as it is stretched in the direction of laser beam movement. Thus, as the laser beam moves, the contact line at point a is pushed forward due to evaporation, while the point b also moves as the liquid rewets the surface. The entire bubble follows the laser and moves smoothly on the surface (Figure 6 - 5 (c-d) and Figure 6 - 6 (c-d)).

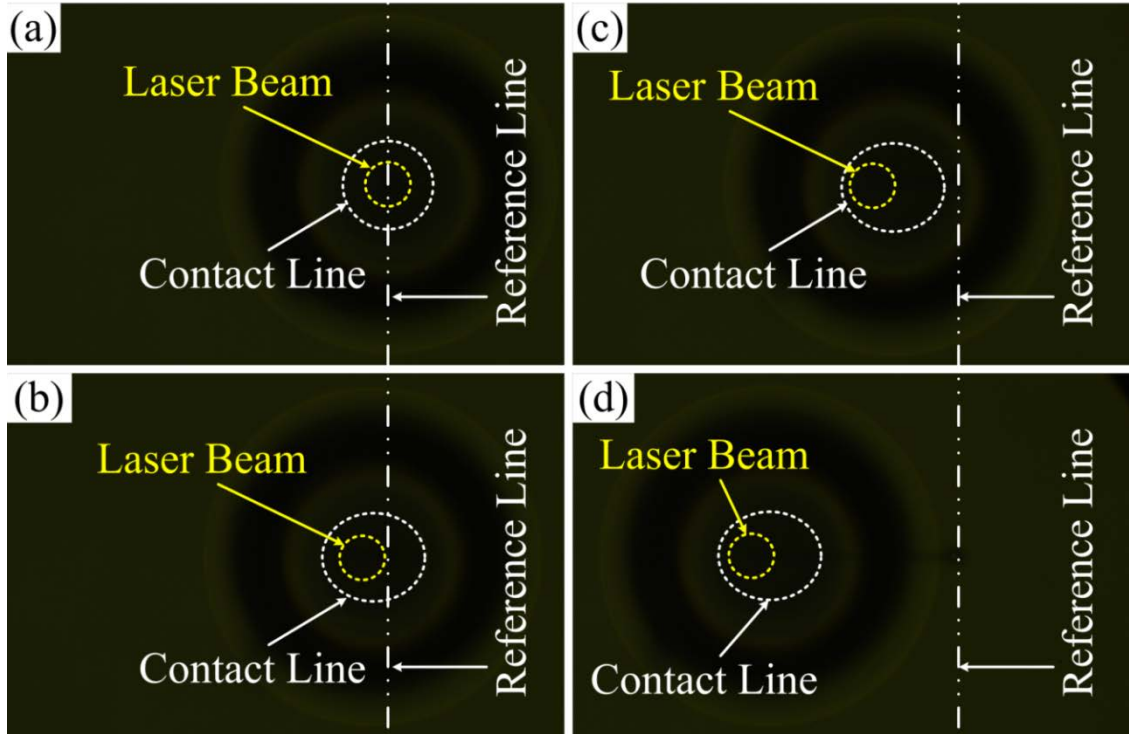


Figure 6 - 5 Contact line behavior on SiO₂ surface with white light

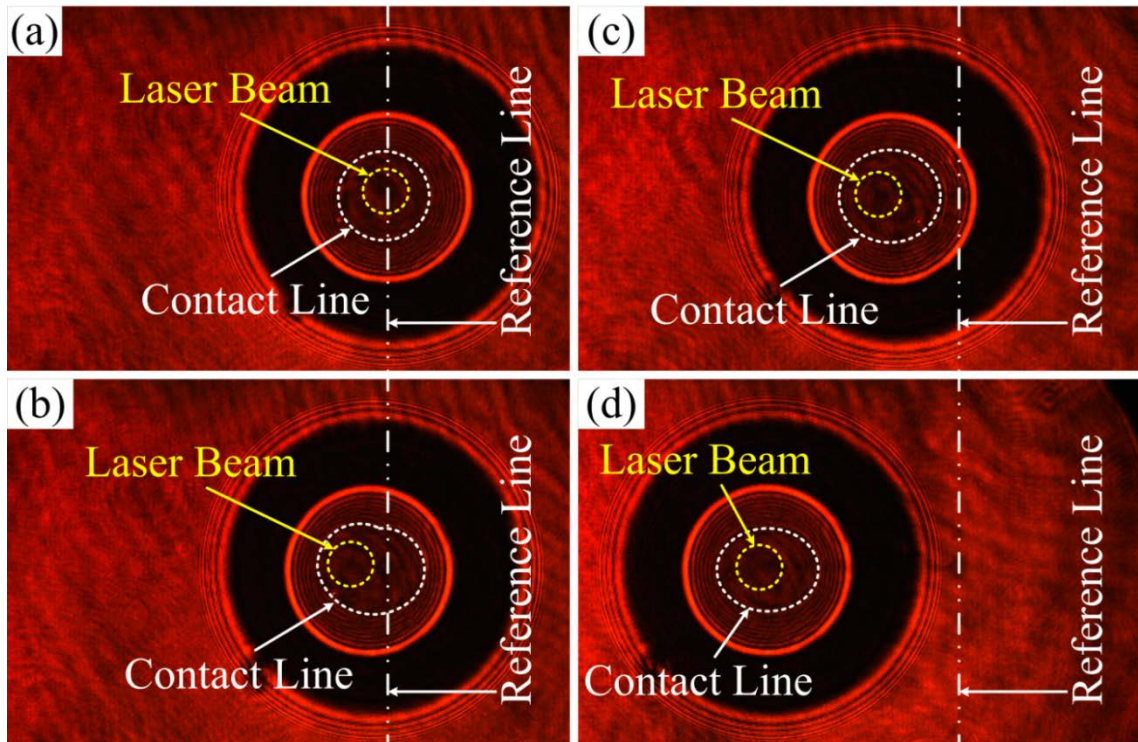


Figure 6 - 6 Contact line behavior on SiO₂ surface with red light

Figure 6 - 7 shows the evolution of microlayer profile at point *a* during the laser movement. The x-axis is the radial distance, which is defined as zero at the center of the bubble base; the y-axis is the local microlayer thickness. The four time steps shown in the Figure 6 - 7 are corresponding to the four snapshots in the Figure 6 - 6. The evaporation in microlayer dominates over the supply of the liquid as the laser beam approaches. Hence, the microlayer thickness decreases (Figure 6 - 6 (b-c)). After the bubble starts to follow the laser and moves at constant speed (Figure 6 - 6 (d)), the microlayer at the point *a* recovers to the steady state (Figure 6 - 6 (a)), at which point the laser is static at the center of bubble base.

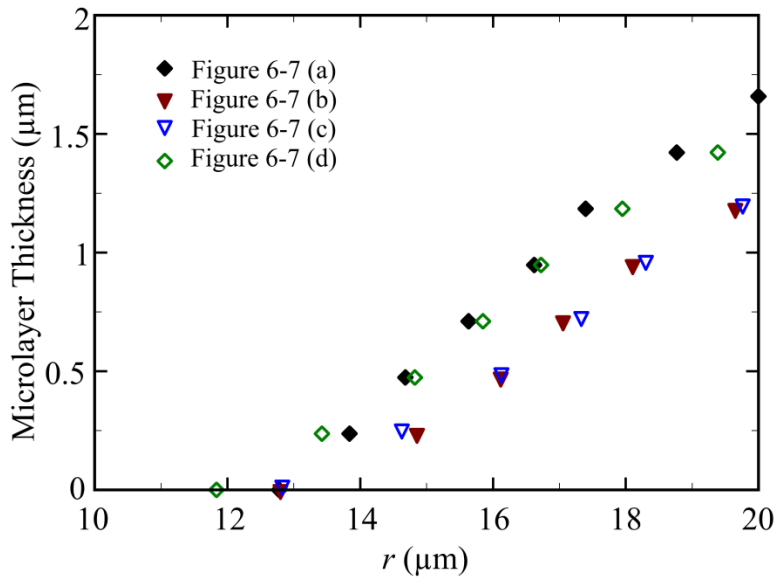


Figure 6 - 7 Microlayer profile at point *a* during laser movement

The bubble following the laser and moving smoothly on SiO_2 surface can be explained by the change of the direction of surface tension exerted on the bubble base, especially at point *a*.

Figure 6 - 8 (a) shows a bubble in the equilibrium state before the laser starts to move. The contact angle is θ_1 . The force balance in the horizontal direction follows Eq. (6-1). When the laser beam approaches to the contact line, as illustrated in Figure 6 - 8 (b), the microlayer

evaporates and the liquid-vapor interface lowers down. The contact angle decreases to θ_2 . This decrease of contact angle induces the change of liquid-vapor surface tension direction, resulted in a net force F as expressed in Eq. (6-3). Because $0^\circ < \theta_2 < \theta_1 < 90^\circ$, the net force F is always positive. Its direction is the same as the laser beam movement, making the contact line move forward and causing the bubble to follow the laser. Thus, the bubble moves smoothly on the hydrophilic SiO_2 surface along with the laser beam.

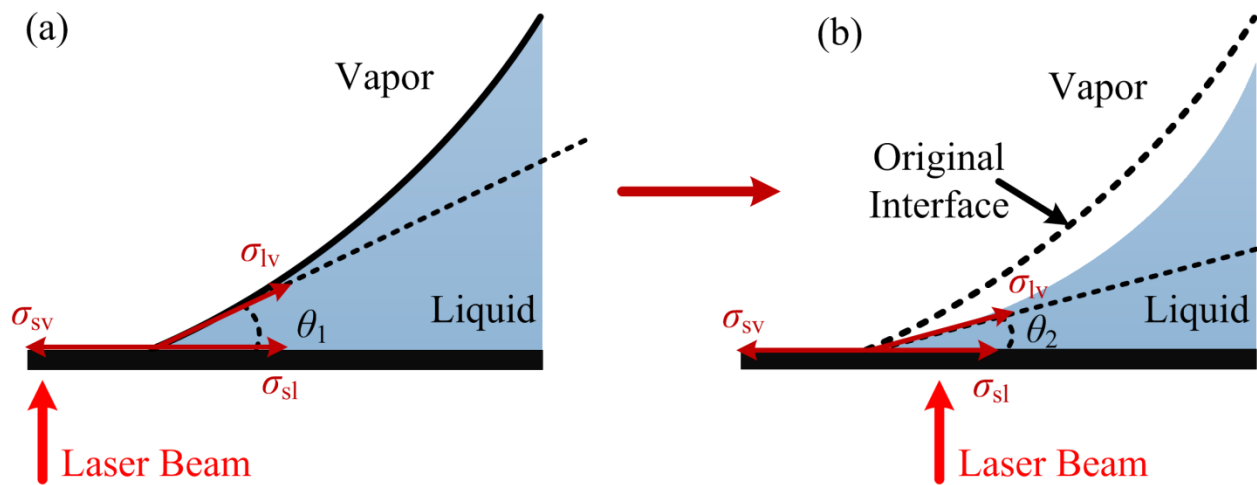


Figure 6 - 8 Change of direction of surface tension at point a on SiO_2 surface

6.5 Summary

In summary, this chapter introduces the investigation of the contact line behavior during the bubble formation, growth, and movement. The bubble was created by laser heating and its movement was achieved by moving the laser beam. It was found that the microlayer covered the entire bubble base at the early stage of the bubble base. The microlayer became thinner as the bubble grew in size and eventually disappeared at the center of the bubble base, thus forming the three-phase contact line. The surface wettability strongly influenced the contact line behavior. On hydrophobic FOTS surface, the contact line does not follow the laser. The contact line

stretched into an elliptical shape, but regained the original circular shape when the laser moved outside the bubble base region. On hydrophilic SiO₂ surface, the bubble followed the laser and moved smoothly on the surface. This difference behavior can be explained by the change of the direction of the liquid-vapor surface tension force exerted at the three-phase contact line. This change caused a negative net force F on FOTS surface, hindering the bubble to follow the laser, while it caused a positive net force F on SiO₂ surface, making the bubble follow the laser and move smoothly on the surface.

7. Conclusions and Future Work

7.1 Conclusions

7.1.1 Critical Height of Microstructures to Enhance CHF

A hypothesis of CHF enhancement by additional evaporation of the thin film was proposed and validated based on the use of ridge-shaped microstructures. Significant enhancement in CHF was attained with 500 nm high ridges on Si surface and 1.2 μm high ridges on SiO_2 surface. A critical height was found to exist below which no enhancement was observed while above which similar enhancements were achieved, irrelevant to the ridge height. An analytical model incorporating the additional evaporation of the thin-film to predict CHF was developed. By adjusting the average thin film thickness as 450 nm on Si and 900 nm on SiO_2 , the predictions from the model were in good agreement with the experimental results. Thus, CHF enhancement occurs only when the ridge heights are greater than the thin film thickness, thus defining the film thickness as the critical height for micro/nano structures to achieve pool boiling enhancement.

7.1.2 Early Evaporation of Microlayer to Enhance CHF

The effect of ridge spacing on CHF enhancement was investigated. A ~120% enhancement was obtained with only ~18% augmentation in surface area, which is among the highest reported in the literature. A new CHF enhancement mechanism, based on the early evaporation of microlayer by disconnecting it from bulk liquid, was proposed. The coupled effect of ridge height and spacing on CHF enhancement was also studied and analyzed. Three enhancement regions depending on ridge space and height were outlined: full enhancement region, partial enhancement region, and no enhancement region. Ridge spacing determined the full enhancement height (H_f) such that larger spacing requires higher H_f . The ratio of space to width

$(S / (S + W))$ determined the full enhancement that can be reached; the ratio of height to full enhancement height (H / H_f) determined the fraction of full enhancement that can be achieved. With dimensions of ridge spacing, width, and height, the CHF can be predicted by the proposed model. Further, the mechanism of early evaporation of microlayer was verified by comparison of growth rate of a laser created bubble on a ridge-structured surface and on a plain surface. The bubble grew 5.25 times faster on the ridge surface as on plain surface causing the CHF to be enhanced by 2.19 times (square root of the ratio of bubble growth rate) and in excellent agreement with pool boiling data.

7.1.3 Steady Vapor Bubble in Pool Boiling

In order to determine the heat transfer characteristics of the evaporating region in the microlayer, a steady-state vapor bubble was created in a pool of sub-cooled water by femtosecond laser heating which allowed for *in-situ* imaging of the microlayer and the contact line regions. The bubble remained stable for hours as the evaporation of water at the surface was balanced by condensation of vapor at the liquid-vapor interface inside the bubble. Experiments were conducted on hydrophilic (SiO_2) and hydrophobic (FOTS) surfaces in regular (with dissolved air) and degassed DI water. The contact angle of the vapor bubble was measured for various cases, and the microlayer and contact line region were imaged under white light and red laser sources. The contact angle for the bubble was found to resemble the drop contact angle on the same surface if the three-phase contact line formed; otherwise the contact angle was dependent on the curvature of the microlayer and the bubble, and decreased with the increasing laser power. For the laser powers studied, the three-phase contact line readily formed in regular DI water, while the microlayer covered the entire bubble base in degassed DI water. The evaporating region was characterized by numerical simulations and experimental results, and permissible

values of overall heat transfer coefficient and corresponding width of the evaporating region were calculated.

7.1.4 Contact Line Behavior of a Vapor Bubble

The contact line behavior of a vapor bubble during bubble formation, growth, and movement was studied. The bubble was created by laser heating and its movement was achieved by moving the laser beam on the sample. It was found that the microlayer covered the entire bubble base at the early stage of the bubble base. The microlayer became thinner as the bubble grew larger and eventually disappeared at the center of the bubble base forming the three-phase contact line. The surface wettability strongly influenced the contact line motion. On hydrophobic FOTS surface, the bubble stuck on the surface and resisted to follow the laser movement. The contact line was elongated when the laser was near it but regained its original shape when the laser moved outside the bubble base region. On hydrophilic SiO₂ surface, the bubble moved smoothly on the surface following the laser. This difference in behavior was explained by the change of the direction of the liquid-vapor surface tension forces exerted on the bubble base resulting in a negative net force F on FOTS surface, hindering the bubble to follow the laser, while it resulted in a positive net force F on SiO₂ surface, allowing the bubble to move smoothly with the laser.

7.2 Future Work

7.2.1 Early Evaporation Induced by Hydrophobic Patterns

In chapter 4, the early evaporation of microlayer was achieved by disconnecting it from bulk liquid using ridges. Another possibility is using hydrophobic patterns (triangular/square/hexagonal/circular dots, long lines, etc.) on a hydrophilic surface. The spacing of these patterns should be in micrometer scale to ensure enough patterns are present underneath

the bubble. The attraction between water and hydrophobic surface is weak that the no-slip boundary condition at wall will not be valid. The hydrophobic patterns on hydrophilic surface will tend to push the liquid to flow to the hydrophilic regions. Thus, the rewetting will be relatively difficult on these patterns. In other words, after the dry spot forms, the liquid cannot rewet the hydrophobic patterns. If these patterns isolate the hydrophilic regions with proper design, the microlayer underneath the bubble can become disconnected from bulk liquid. Early evaporation could possibly be triggered and CHF enhancement can be achieved. In addition to the new patterns to achieve early evaporation, the boiling on these modified surfaces can be visualized by the high speed camera. With proper optical setup, the effect of these patterns on the nucleation site density, bubble dynamics (bubble growth rate, bubble departure size and frequency), bubble contact angles and dry region evolution underneath the bubble can be characterized.

7.2.2 Boiling Heat Transfer Mechanisms

There are four kinds of mechanisms that are widely accepted as mechanisms of bubble growth in boiling heat transfer: transient conduction, microconvection, microlayer evaporation, and contact line evaporation. During boiling, the actual dominant mechanisms are normally a combination of two or more of these. For example, during bubble growth, microconvection, microlayer evaporation, and contact line evaporation contribute to the bubble growth; while during bubble departure, transient conduction and contact line evaporation affect the heat transfer rate. However, the contribution for these mechanisms is still unclear. The random, unstable nature of boiling, and the short time span of the bubble ebullition cycle make it challenging to study these mechanisms in boiling. The *in-situ* imaging of the microlayer and contact line region underneath a steady vapor bubble is a powerful technique (introduced in chapter 5) having large potential to

study the contributions for each mechanism during bubble growth. From the evolution of the microlayer profile as bubble grows, the liquid pressure distribution can be determined, as thus liquid flow in this region. In this way, the contribution of microconvection can be featured. With measured temperature profile, the overall heat transfer rate in microlayer region can be obtained numerically from energy conservation. Thus, the individual contribution of microconvection, microlayer evaporation, and contact line evaporation can be determined.

7.2.3 “Controlling” the Bubbles Behavior in Boiling

The contact line motion influences heat transfer rate. It has been shown that surface wettability strongly affects contact line behavior in chapter 6. Thus, understanding how anisotropic structures (ridges, channels, nanorods, and nano particles, etc.) and isotropic structures (uniform pillars, cavities, etc.) affect contact line behavior during bubble growth and departure will be extremely insightful. Further, contact line behavior on a surface with hybrid wettability, such as hydrophilic surface with hydrophobic structures, and vice versa, will prove to be a fundamental study to predict heat transfer performance on such surfaces. Generally speaking, hydrophobic surfaces facilitate nucleation of vapor bubbles, resulting in a higher heat transfer coefficient but lower CHF. Hydrophilic surfaces allow the liquid to rewet dry region easily and can thus delay the CHF occurrence, but have lower heat transfer coefficient. Thus, the surface with hybrid wettability (hydrophobic structures on hydrophilic substrate or hydrophilic structures on hydrophobic substrate) is a promising technique to enhance heat transfer coefficient and CHF simultaneously. Briefly, CHF occurs when the vapor release blocks the liquid flow path to prevent it from rewetting the surface. Thus, with proper design of the patterns (shape, dimension), the bubble can be possibly guided to move on the surface in a certain direction, while the liquid can flow to rewet the surface in the other direction. In this way, the bubble

behavior is “controlled” so that the vapor release pathway and liquid rewetting pathway are separated, and thus can potentially delay CHF.

References

- 1 Dhir, V. K. Boiling heat transfer. *Annual Review of Fluid Mechanics* **30**, 365-401 (1998).
- 2 Anandan, S. S. & Ramalingam, V. Thermal management of electronics: A review of literature. *Thermal Science* **12**, 5-26 (2008).
- 3 Abu-Khader, M. M. Recent advances in nuclear power: A review. *Progress in Nuclear Energy* **51**, 225-235 (2009).
- 4 Lu, Y. W. & Kandlikar, S. G. Nanoscale Surface Modification Techniques for Pool Boiling Enhancement A Critical Review and Future Directions. *Heat Transfer Engineering* **32**, 827-842 (2011).
- 5 Nukiyama, S. The maximum and minimum values of the heat Q transmitted from metal to boiling water under atmospheric pressure. *International Journal of Heat and Mass Transfer* **9**, 1419-1433 (1966).
- 6 Carey, V. P. *Liquid-Vapor Phase-Change Phenomena: An Introduction to the Thermophysics of Vaporization and Condensation Processes in Heat Transfer Equipment, 2nd ed.*, (Taylor & Francis, 2007).
- 7 Hsu, Y. Y. On the Size Range of Active Nucleation Cavities on a Heating Surface. *Journal of Heat Transfer* **84**, 207-213 (1962).
- 8 Mikic, B. B., Rohsenow, W. M. & Griffith, P. On bubble growth rates. *International Journal of Heat and Mass Transfer* **13**, 657-666 (1970).
- 9 Mikic, B. B. R., W.M. . Bubble growth rates in non uniform temperature field. *Progress in Heat and Mass Transfer* **2**, 283-292 (1969).
- 10 Zuber, N. *hydrodynamic aspects of boiling heat transfer* PhD thesis, University of California, Los Angeles, (1959).

- 11 Zuber, N. Nucleate boiling. The region of isolated bubbles and the similarity with natural convection. *International Journal of Heat and Mass Transfer* **6**, 53-78 (1963).
- 12 Kim, J. Review of nucleate pool boiling bubble heat transfer mechanisms. *International Journal of Multiphase Flow* **35**, 1067-1076 (2009).
- 13 Mikic, B. B. & Rohsenow, W. M. A New Correlation of Pool-Boiling Data Including Effect of Heating Surface Characteristics. *Journal of Heat Transfer* **91**, 245-250 (1969).
- 14 Chen, T. L. & Chung, J. N. Coalescence of bubbles in nucleate boiling on microheaters. *International Journal of Heat and Mass Transfer* **45**, 2329-2341 (2002).
- 15 Gerardi, C., Buongiorno, J., Hu, L. W. & McKrell, T. Study of bubble growth in water pool boiling through synchronized, infrared thermometry and high-speed video. *International Journal of Heat and Mass Transfer* **53**, 4185-4192 (2010).
- 16 Rohsenow, W. M. A Method of Correlating Heat Transfer Data for Surface Boiling Liquids. *Transaction ASME* **74**, 969-976 (1952).
- 17 Moore, F. D. & Mesler, R. B. The measurement of rapid surface temperature fluctuations during nucleate boiling of water. *AIChE Journal* **7**, 620-624 (1961).
- 18 Cooper, M. G. & Lloyd, A. J. P. The microlayer in nucleate pool boiling. *International Journal of Heat and Mass Transfer* **12**, 895-913 (1969).
- 19 Judd, R. L. & Hwang, K. S. A Comprehensive Model for Nucleate Pool Boiling Heat Transfer Including Microlayer Evaporation. *Journal of Heat Transfer* **98**, 623-629 (1976).
- 20 Jawurek, H. H. Simultaneous determination of microlayer geometry and bubble growth in nucleate boiling. *International Journal of Heat and Mass Transfer* **12**, 843-848 (1969).

- 21 Koffman, L. D. & Plesset, M. S. Experimental Observations of the Microlayer in Vapor Bubble Growth on a Heated Solid. *Journal of Heat Transfer* **105**, 625-632 (1983).
- 22 Gao, M., Zhang, L., Cheng, P. & Quan, X. An investigation of microlayer beneath nucleation bubble by laser interferometric method. *International Journal of Heat and Mass Transfer* **57**, 183-189 (2013).
- 23 Jung, S. & Kim, H. An Experimental Study on Heat Transfer Mechanisms in the Microlayer using Integrated Total Reflection, Laser Interferometry and Infrared Thermometry Technique. *Heat Transfer Engineering* **36**, 1002-1012 (2015).
- 24 Wayner Jr, P. C., Kao, Y. K. & LaCroix, L. V. The interline heat-transfer coefficient of an evaporating wetting film. *International Journal of Heat and Mass Transfer* **19**, 487-492 (1976).
- 25 Potash, M. & Wayner, P. C. Evaporation from a two-dimensional extended meniscus. *International Journal of Heat and Mass Transfer* **15**, 1851-1863 (1972).
- 26 Demiray, F. & Kim, J. Microscale heat transfer measurements during pool boiling of FC-72: effect of subcooling. *International Journal of Heat and Mass Transfer* **47**, 3257-3268 (2004).
- 27 Myers, J. G., Yerramilli, V. K., Hussey, S. W., Yee, G. F. & Kim, J. Time and space resolved wall temperature and heat flux measurements during nucleate boiling with constant heat flux boundary conditions. *International Journal of Heat and Mass Transfer* **48**, 2429-2442 (2005).
- 28 Kunkelmann, C., Ibrahim, K., Schweizer, N., Herbert, S., Stephan, P. & Gambaryan-Roisman, T. The effect of three-phase contact line speed on local evaporative heat

- transfer: Experimental and numerical investigations. *International Journal of Heat and Mass Transfer* **55**, 1896-1904 (2012).
- 29 Stephan, P. & Hammer, J. A new model for nucleate boiling heat transfer. *Warme- und Stoffubertragung* **30**, 119-125 (1994).
- 30 Lienhard, J. H., Dhir, V. K., Kentucky, U. O. & Center, L. R. *Extended hydrodynamic theory of the peak and minimum pool boiling heat fluxes*. (National Aeronautics and Space Administration, 1973).
- 31 Rohsenow, W. M. & Griffith, P. *Correlation of Maximum Heat Flux Data for Boiling of Saturated Liquids*. (Massachusetts Institute of Technology, Division of Industrial Cooperation, 1955).
- 32 Kim, D. E., Yu, D. I., Jerng, D. W., Kim, M. H. & Ahn, H. S. Review of boiling heat transfer enhancement on micro/nanostructured surfaces. *Experimental Thermal and Fluid Science* **66**, 173-196 (2015).
- 33 Haramura, Y. & Katto, Y. A new hydrodynamic model of critical heat flux, applicable widely to both pool and forced convection boiling on submerged bodies in saturated liquids. *International Journal of Heat and Mass Transfer* **26**, 389-399 (1983).
- 34 Kandlikar, S. G. A theoretical model to predict pool boiling CHF incorporating effects of contact angle and orientation. *Journal of Heat Transfer-Transactions of the ASME* **123**, 1071-1079 (2001).
- 35 Rajvanshi, A. K., Saini, J. S. & Prakash, R. Investigation of macrolayer thickness in nucleate pool boiling at high heat flux. *International Journal of Heat and Mass Transfer* **35**, 343-350 (1992).

- 36 Guan, C. K., Klausner, J. F. & Mei, R. A new mechanistic model for pool boiling CHF on horizontal surfaces. *International Journal of Heat and Mass Transfer* **54**, 3960-3969 (2011).
- 37 Chu, K. H., Enright, R. & Wang, E. N. Structured surfaces for enhanced pool boiling heat transfer. *Applied Physics Letters* **100**, 241603 (2012).
- 38 Gambill, W. R. & Lienhard, J. H. An Upper Bound for the Critical Boiling Heat Flux. *Journal of Heat Transfer* **111**, 815-818 (1989).
- 39 McCarthy, M., Gerasopoulos, K., Maroo, S. C. & Hart, A. J. Materials fabrication and manufacturing of micro/nanostructured surfaces for phase change heat transfer enhancement. *Nanoscale and Microscale Thermophysical Engineering* **18**, 288-310 (2014).
- 40 Taylor, R. *et al.* Small particles, big impacts: A review of the diverse applications of nanofluids. *Journal of Applied Physics* **113**, 011301 (2013).
- 41 Eastman, J. A., Choi, U. S., Li, S., Thompson, L. J. & Lee, S. in *Nanophase and Nanocomposite Materials II* Vol. 457 *Materials Research Society Symposium Proceedings* (eds S. Komarneni, J. C. Parker, & H. J. Wollenberger) 3-11 (Materials Research Society, 1997).
- 42 You, S. M., Kim, J. H. & Kim, K. H. Effect of nanoparticles on critical heat flux of water in pool boiling heat transfer. *Applied Physics Letters* **83**, 3374-3376 (2003).
- 43 Murshed, S. M. S., de Castro, C. A. N., Lourenco, M. J. V., Lopes, M. L. M. & Santos, F. J. V. A review of boiling and convective heat transfer with nanofluids. *Renewable and Sustainable Energy Reviews* **15**, 2342-2354 (2011).

- 44 Barber, J., Brutin, D. & Tadrist, L. A review on boiling heat transfer enhancement with nanofluids. *Nanoscale Research Letters* **6**, 16 (2011).
- 45 Kamatchi, R. & Venkatachalapathy, S. Parametric study of pool boiling heat transfer with nanofluids for the enhancement of critical heat flux: A review. *International Journal of Thermal Sciences* **87**, 228-240 (2015).
- 46 Ciloglu, D. & Bolukbasi, A. A comprehensive review on pool boiling of nanofluids. *Applied Thermal Engineering* **84**, 45-63 (2015).
- 47 Seon Ahn, H. & Hwan Kim, M. A Review on Critical Heat Flux Enhancement With Nanofluids and Surface Modification. *Journal of Heat Transfer* **134**, 024001-024001 (2011).
- 48 Das, S. K., Putra, N. & Roetzel, W. Pool boiling characteristics of nano-fluids. *International Journal of Heat and Mass Transfer* **46**, 851-862 (2003).
- 49 Das, S. K., G., P. N. & Baby, A. Survey on nucleate pool boiling of nanofluids: the effect of particle size relative to roughness. *Journal of Nanoparticle Research* **10**, 1099-1108 (2008).
- 50 Xu, L., Xu, J., Wang, B. & Zhang, W. Pool boiling heat transfer on the microheater surface with and without nanoparticles by pulse heating. *International Journal of Heat and Mass Transfer* **54**, 3309-3322 (2011).
- 51 Arik, M. & Bar-Cohen, A. Effusivity-based correlation of surface property effects in pool boiling CHF of dielectric liquids. *International Journal of Heat and Mass Transfer* **46**, 3755-3764 (2003).

- 52 Sefiane, K. On the role of structural disjoining pressure and contact line pinning in critical heat flux enhancement during boiling of nanofluids. *Applied Physics Letters* **89**, 044106 (2006).
- 53 Park, S. D. *et al.* Effects of nanofluids containing graphene/graphene-oxide nanosheets on critical heat flux. *Applied Physics Letters* **97**, 023103 (2010).
- 54 Kim, S. J., Bang, I. C., Buongiorno, J. & Hu, L. W. Surface wettability change during pool boiling of nanofluids and its effect on critical heat flux. *International Journal of Heat and Mass Transfer* **50**, 4105-4116 (2007).
- 55 Yang, W. J., Takizawa, H. & Vrable, D. L. Augmented boiling on copper-graphite composite surface. *International Journal of Heat and Mass Transfer* **34**, 2751-2758 (1991).
- 56 Liang, H. S. & Yang, W. J. Nucleate pool boiling heat transfer in a highly wetting liquid on micro-graphite-fiber composite surfaces. *International Journal of Heat and Mass Transfer* **41**, 1993-2001 (1998).
- 57 Parker, J. L. & El-Genk, M. S. Effect of Surface Orientation on Nucleate Boiling of FC-72 on Porous Graphite. *Journal of Heat Transfer* **128**, 1159-1175 (2006).
- 58 Li, S., Furberg, R., Toprak, M. S., Palm, B. & Muhammed, M. Nature-Inspired Boiling Enhancement by Novel Nanostructured Macroporous Surfaces. *Advanced Functional Materials* **18**, 2215-2220 (2008).
- 59 Zhang, B. J., Kim, K. J. & Yoon, H. Enhanced heat transfer performance of alumina sponge-like nano-porous structures through surface wettability control in nucleate pool boiling. *International Journal of Heat and Mass Transfer* **55**, 7487-7498 (2012).

- 60 Ahn, H. S., Kim, J. M., Par, C., Jang, J. W., Lee, J. S., Kim, H., Kaviany, M. & Kim, M. H. A Novel Role of Three Dimensional Graphene Foam to Prevent Heater Failure during Boiling. *Scientific Reports* **3**, 1960 (2013).
- 61 Ahn, H. S., Kim, J. M., Kaviany, M. & Kim, M. H. Pool boiling experiments in reduced graphene oxide colloids part II – Behavior after the CHF, and boiling hysteresis. *International Journal of Heat and Mass Transfer* **78**, 224-231 (2014).
- 62 Ahn, H. S., Sinha, N., Zhang, M., Banerjee, D., Fang, S. & Baughman, R. H. Pool Boiling Experiments on Multiwalled Carbon Nanotube (MWCNT) Forests. *Journal of Heat Transfer* **128**, 1335-1342 (2006).
- 63 Hee Seok, A., Sathyamurthi, V. & Banerjee, D. Pool Boiling Experiments on a Nano-Structured Surface. *Components and Packaging Technologies, IEEE Transactions on* **32**, 156-165 (2009).
- 64 Lu, M. C., Chen, R., Srinivasan, V., Carey, V. P. & Majumdar, A. Critical heat flux of pool boiling on Si nanowire array-coated surfaces. *International Journal of Heat and Mass Transfer* **54**, 5359-5367 (2011).
- 65 Ujereh, S., Fisher, T. & Mudawar, I. Effects of carbon nanotube arrays on nucleate pool boiling. *International Journal of Heat and Mass Transfer* **50**, 4023-4038 (2007).
- 66 Chen, R., Lu, M. C., Srinivasan, V., Wang, Z., Cho, H. H. & Majumdar, A. Nanowires for Enhanced Boiling Heat Transfer. *Nano Letters* **9**, 548-553 (2009).
- 67 Yao, Z., Lu, Y. W. & Kandlikar, S. G. Direct growth of copper nanowires on a substrate for boiling applications. *Micro & Nano Letters, IET* **6**, 563-566 (2011).

- 68 Im, Y., Joshi, Y. K., Dietz, C. & Lee, S. S. Enhanced Boiling of a Dielectric Liquid on Copper Nanowire Surfaces. *International Journal of Micro-nano Scale Transport* **1**, 79-96 (2010).
- 69 Dai, X., Huang, X., Yang, F., Li, X., Sightler, J., Yang, Y. & Li, C. Enhanced nucleate boiling on horizontal hydrophobic-hydrophilic carbon nanotube coatings. *Applied Physics Letters* **102**, 161605 (2013).
- 70 Yao, Z., Lu, Y. W. & Kandlikar, S. G. Effects of nanowire height on pool boiling performance of water on silicon chips. *International Journal of Thermal Sciences* **50**, 2084-2090 (2011).
- 71 McHale, J. P., Garimella, S. V., Fisher, T. S. & Powell, G. A. Pool boiling performance comparison of smooth and sintered copper surfaces with and without carbon nanotubes. *Nanoscale and Microscale Thermophysical Engineering* **15**, 133-150 (2011).
- 72 Hsieh, S. S. & Weng, C. J. Nucleate pool boiling from coated surfaces in saturated R-134a and R-407c. *International Journal of Heat and Mass Transfer* **40**, 519-532 (1997).
- 73 Cieśliński, J. T. Nucleate pool boiling on porous metallic coatings. *Experimental Thermal and Fluid Science* **25**, 557-564 (2002).
- 74 Chang, J. Y. & You, S. M. Enhanced boiling heat transfer from microporous surfaces: effects of a coating composition and method. *International Journal of Heat and Mass Transfer* **40**, 4449-4460 (1997).
- 75 Chang, J. Y. & You, S. M. Boiling heat transfer phenomena from microporous and porous surfaces in saturated FC-72. *International Journal of Heat and Mass Transfer* **40**, 4437-4447 (1997).

- 76 Liter, S. G. & Kaviany, M. Pool-boiling CHF enhancement by modulated porous-layer coating: theory and experiment. *International Journal of Heat and Mass Transfer* **44**, 4287-4311 (2001).
- 77 Hwang, G. S. & Kaviany, M. Critical heat flux in thin, uniform particle coatings. *International Journal of Heat and Mass Transfer* **49**, 844-849 (2006).
- 78 Li, C., Wang, Z., Wang, P. I., Peles, Y., Koratkar, N. & Peterson, G. P. Nanostructured copper interfaces for enhanced boiling. *Small* **4**, 1084-1088 (2008).
- 79 Forrest, E., Williamson, E., Buongiorno, J., Hu, L. W., Rubner, M. & Cohen, R. Augmentation of nucleate boiling heat transfer and critical heat flux using nanoparticle thin-film coatings. *International Journal of Heat and Mass Transfer* **53**, 58-67 (2010).
- 80 Feng, B., Weaver, K. & Peterson, G. P. Enhancement of critical heat flux in pool boiling using atomic layer deposition of alumina. *Applied Physics Letters* **100**, 053120 (2012).
- 81 Phan, H. T., Caney, N., Marty, P., Colasson, S. & Gavillet, J. Surface wettability control by nanocoating: The effects on pool boiling heat transfer and nucleation mechanism. *International Journal of Heat and Mass Transfer* **52**, 5459-5471 (2009).
- 82 Hendricks, T. J., Krishnan, S., Choi, C., Chang, C. H. & Paul, B. Enhancement of pool-boiling heat transfer using nanostructured surfaces on aluminum and copper. *International Journal of Heat and Mass Transfer* **53**, 3357-3365 (2010).
- 83 Guglielmini, G., Misale, M. & Schenone, C. Boiling of saturated FC-72 on square pin fin arrays. *International Journal of Thermal Sciences* **41**, 599-608 (2002).
- 84 Rainey, K. N., You, S. M. & Lee, S. Effect of pressure, subcooling, and dissolved gas on pool boiling heat transfer from microporous, square pin-finned surfaces in FC-72. *International Journal of Heat and Mass Transfer* **46**, 23-35 (2003).

- 85 Honda, H., Takamastu, H. & Wei, J. J. Enhanced boiling of FC-72 on silicon chips with micro-pin-fins and submicron-scale roughness. *Journal of Heat Transfer-Transactions of the Asme* **124**, 383-390 (2002).
- 86 Honda, H. & Wei, J. J. Enhanced boiling heat transfer from electronic components by use of surface microstructures. *Experimental Thermal and Fluid Science* **28**, 159-169 (2004).
- 87 Wei, J. J. & Honda, H. Effects of fin geometry on boiling heat transfer from silicon chips with micro-pin-fins immersed in FC-72. *International Journal of Heat and Mass Transfer* **46**, 4059-4070 (2003).
- 88 Mori, S. & Okuyama, K. Enhancement of the critical heat flux in saturated pool boiling using honeycomb porous media. *International Journal of Multiphase Flow* **35**, 946-951 (2009).
- 89 Dong, L., Quan, X. & Cheng, P. An experimental investigation of enhanced pool boiling heat transfer from surfaces with micro/nano-structures. *International Journal of Heat and Mass Transfer* **71**, 189-196 (2014).
- 90 Kim, S. H., Lee, G. C., Kang, J. Y., Moriyama, K., Kim, M. H. & Park, H. S. Boiling heat transfer and critical heat flux evaluation of the pool boiling on micro structured surface. *International Journal of Heat and Mass Transfer* **91**, 1140-1147 (2015).
- 91 Kim, D. E., Yu, D. I., Park, S. C., Kwak, H. J. & Ahn, H. S. Critical heat flux triggering mechanism on micro-structured surfaces: Coalesced bubble departure frequency and liquid furnishing capability. *International Journal of Heat and Mass Transfer* **91**, 1237-1247 (2015).
- 92 Chien, L. H. & Webb, R. L. Visualization of pool boiling on enhanced surfaces. *Experimental Thermal and Fluid Science* **16**, 332-341 (1998).

- 93 Chien, L. H. & Webb, R. L. Measurement of bubble dynamics on an enhanced boiling surface. *Experimental Thermal and Fluid Science* **16**, 177-186 (1998).
- 94 Chien, L. H. & Webb, R. L. A nucleate boiling model for structured enhanced surfaces. *International Journal of Heat and Mass Transfer* **41**, 2183-2195 (1998).
- 95 Ramaswamy, C., Joshi, Y., Nakayama, W. & Johnson, W. B. High-speed visualization of boiling from an enhanced structure. *International Journal of Heat and Mass Transfer* **45**, 4761-4771 (2002).
- 96 Ghiu, C. D. & Joshi, Y. K. Visualization study of pool boiling from thin confined enhanced structures. *International Journal of Heat and Mass Transfer* **48**, 4287-4299 (2005).
- 97 Das, A. K., Das, P. K. & Saha, P. Performance of different structured surfaces in nucleate pool boiling. *Applied Thermal Engineering* **29**, 3643-3653 (2009).
- 98 Cooke, D. & Kandlikar, S. G. Pool Boiling Heat Transfer and Bubble Dynamics Over Plain and Enhanced Microchannels. *Journal of Heat Transfer* **133**, 052902-052902 (2011).
- 99 Chen, T. An experimental investigation of nucleate boiling heat transfer from an enhanced cylindrical surface. *Applied Thermal Engineering* **59**, 355-361 (2013).
- 100 Kim, D. E., Park, S. C., Yu, D. I., Kim, M. H. & Ahn, H. S. Enhanced critical heat flux by capillary driven liquid flow on the well-designed surface. *Applied Physics Letters* **107**, 023903 (2015).
- 101 Cooke, D. & Kandlikar, S. G. Effect of open microchannel geometry on pool boiling enhancement. *International Journal of Heat and Mass Transfer* **55**, 1004-1013 (2012).

- 102 Kandlikar, S. G. Controlling bubble motion over heated surface through evaporation momentum force to enhance pool boiling heat transfer. *Applied Physics Letters* **102**, 051611 (2013).
- 103 Launay, S., Fedorov, A. G., Joshi, Y., Cao, A. & Ajayan, P. M. Hybrid micro-nano structured thermal interfaces for pool boiling heat transfer enhancement. *Microelectronics Journal* **37**, 1158-1164 (2006).
- 104 Wei, B. Q., Vajtai, R., Jung, Y., Ward, J., Zhang, R., Ramanath, G. & Ajayan, P. M. Assembly of Highly Organized Carbon Nanotube Architectures by Chemical Vapor Deposition. *Chemistry of Materials* **15**, 1598-1606 (2003).
- 105 Kim, S., Kim, H. D., Kim, H., Ahn, H. S., Jo, H., Kim, J. & Kim, M. H. Effects of nano-fluid and surfaces with nano structure on the increase of CHF. *Experimental Thermal and Fluid Science* **34**, 487-495 (2010).
- 106 Yao, Z., Lu, Y. W. & Kandlikar, S. G. Fabrication of nanowires on orthogonal surfaces of microchannels and their effect on pool boiling. *Journal of Micromechanics and Microengineering* **22** (2012).
- 107 Yao, Z., Lu, Y. W. & Kandlikar, S. G. Pool Boiling Heat Transfer Enhancement Through Nanostructures on Silicon Microchannels. *Journal of Nanotechnology in Engineering and Medicine* **3**, 031002-031002 (2013).
- 108 Jaikumar, A. & Kandlikar, S. G. Enhanced pool boiling heat transfer mechanisms for selectively sintered open microchannels. *International Journal of Heat and Mass Transfer* **88**, 652-661 (2015).
- 109 Rahman, M. M., Ölçeroğlu, E. & McCarthy, M. Role of Wickability on the Critical Heat Flux of Structured Superhydrophilic Surfaces. *Langmuir* **30**, 11225-11234 (2014).

- 110 Dhillon, N. S., Buongiorno, J. & Varanasi, K. K. Critical heat flux maxima during boiling crisis on textured surfaces. *Nature Communications* **6** (2015).
- 111 C'oso, D., Srinivasan, V., Lu, M. C., Chang, J. Y. & Majumdar, A. Enhanced Heat Transfer in Biporous Wicks in the Thin Liquid Film Evaporation and Boiling Regimes. *Journal of Heat Transfer* **134**, 101501-101501 (2012).
- 112 Ahn, H. S., Jo, H. J., Kang, S. H. & Kim, M. H. Effect of liquid spreading due to nano/microstructures on the critical heat flux during pool boiling. *Applied Physics Letters* **98**, 071908 (2011).
- 113 Jones, B. J., McHale, J. P. & Garimella, S. V. The Influence of Surface Roughness on Nucleate Pool Boiling Heat Transfer. *Journal of Heat Transfer* **131**, 121009-121009 (2009).
- 114 Chen, S. W., Hsieh, J. C., Chou, C. T., Lin, H. H., Shen, S. C. & Tsai, M. J. Experimental investigation and visualization on capillary and boiling limits of micro-grooves made by different processes. *Sensors and Actuators A: Physical* **139**, 78-87 (2007).
- 115 Maroo, S. C. & Chung, J. N. Nanoscale liquid-vapor phase-change physics in nonevaporating region at the three-phase contact line. *Journal of Applied Physics* **106**, 064911 (2009).
- 116 Maroo, S. C. & Chung, J. N. Heat transfer characteristics and pressure variation in a nanoscale evaporating meniscus. *International Journal of Heat and Mass Transfer* **53**, 3335-3345 (2010).
- 117 Maroo, S. C. & Chung, J. N. Molecular dynamic simulation of platinum heater and associated nano-scale liquid argon film evaporation and colloidal adsorption characteristics. *Journal of Colloid and Interface Science* **328**, 134-146 (2008).

- 118 Maroo, S. C. & Chung, J. N. A Possible Role of Nanostructured Ridges on Boiling Heat Transfer Enhancement. *Journal of Heat Transfer* **135**, 041501-041501 (2013).
- 119 Jo, H., Ahn, H. S., Kang, S. H. & Kim, M. H. A study of nucleate boiling heat transfer on hydrophilic, hydrophobic and heterogeneous wetting surfaces. *International Journal of Heat and Mass Transfer* **54**, 5643-5652 (2011).
- 120 Angirasa, D. & Peterson, G. P. Upper and lower rayleigh number bounds for two dimensional natural convection over a finite horizontal surface situated in a fluid-saturated porous medium. *Numerical Heat Transfer, Part A: Applications* **33**, 477-493 (1998).
- 121 Glassbrenner, C. J. & Slack, G. A. Thermal Conductivity of Silicon and Germanium from 30K to the Melting Point. *Physical Review* **134**, A1058-A1069 (1964).
- 122 Dhir, V. K. & Liaw, S. P. Framework for a Unified Model for Nucleate and Transition Pool Boiling. *Journal of Heat Transfer-Transactions of the ASME* **111**, 739-746 (1989).
- 123 Yang, D., Krasowska, M., Priest, C., Popescu, M. N. & Ralston, J. Dynamics of Capillary-Driven Flow in Open Microchannels. *The Journal of Physical Chemistry C* **115**, 18761-18769 (2011).
- 124 Park, K. & Lee, K. S. Flow and heat transfer characteristics of the evaporating extended meniscus in a micro-capillary channel. *International Journal of Heat and Mass Transfer* **46**, 4587-4594 (2003).
- 125 Nam, Y., Aktinol, E., Dhir, V. K. & Ju, Y. S. Single bubble dynamics on a superhydrophilic surface with artificial nucleation sites. *International Journal of Heat and Mass Transfer* **54**, 1572-1577 (2011).

- 126 Mukherjee, A. & Kandlikar, S. G. Numerical study of single bubbles with dynamic contact angle during nucleate pool boiling. *International Journal of Heat and Mass Transfer* **50**, 127-138 (2007).
- 127 Mitrovic, J. & Hartmann, F. A new microstructure for pool boiling. *Superlattices and Microstructures* **35**, 617-628 (2004).
- 128 Ahn, H. S. & Kim, M. H. The boiling phenomenon of alumina nanofluid near critical heat flux. *International Journal of Heat and Mass Transfer* **62**, 718-728 (2013).
- 129 Mukherjee, A. & Kandlikar, S. G. Numerical Study of an Evaporating Meniscus on a Moving Heated Surface. *Journal of Heat Transfer* **128**, 1285-1292 (2006).
- 130 Drelich, J., Miller, J. D. & Good, R. J. The effect of drop (bubble) size on advancing and receding contact angles for heterogeneous and rough solid surfaces as observed with sessile-drop and captive-bubble techniques. *Journal of Colloid and Interface Science* **179**, 37-50 (1996).
- 131 Drelich, J. The effect of drop (bubble) size on contact angle at solid surfaces. *Journal of Adhesion* **63**, 31-51 (1997).
- 132 Xue, J., Shi, P., Zhu, L., Ding, J., Chen, Q. & Wang, Q. A modified captive bubble method for determining advancing and receding contact angles. *Applied Surface Science* **296**, 133-139 (2014).
- 133 Kowalczyk, P. B. & Drzymala, J. Contact Angle of Bubble with an Immersed-in-Water Particle of Different Materials. *Industrial and Engineering Chemistry Research* **50**, 4207-4211 (2011).
- 134 Drzymala, J. & Lekki, J. Flotometry—Another way of characterizing flotation. *Journal of Colloid and Interface Science* **130**, 205-210 (1989).

- 135 Drzymala, J. Characterization of materials by Hallimond tube flotation. Part 2: maximum size of floating particles and contact angle. *International Journal of Mineral Processing* **42**, 153-167 (1994).
- 136 Watanabe, M., Kowalczyk, P. B. & Drzymala, J. Analytical Solution of Equation Relating Maximum Size of Floating Particle and its Hydrophobicity. *Physicochemical Problems of Mineral Processing*, 13-20 (2011).
- 137 Kowalczyk, P. B., Sahbaz, O. & Drzymala, J. Maximum size of floating particles in different flotation cells. *Minerals Engineering* **24**, 766-771 (2011).
- 138 Kandlikar, S. G. & Steinke, M. E. Contact angles and interface behavior during rapid evaporation of liquid on a heated surface. *International Journal of Heat and Mass Transfer* **45**, 3771-3780 (2002).
- 139 Serret, D., Guignard, S. & Tadrist, L. Nucleate Boiling on a Single Site: Contact Angle Analysis for a Quasi-2D Growing Vapour Bubble. *Microgravity Science and Technology* **21**, 101-105 (2009).
- 140 van der Geld, C. W. M. Prediction of dynamic contact angle histories of a bubble growing at a wall. *International Journal of Heat and Fluid Flow* **25**, 74-80 (2004).
- 141 Ramanujapu, N. & Dhir, V. K. *Dynamics of contact angle during growth and detachment of a vapor bubble at a single nucleation site*. (5th ASME/JSME Thermal Engineering Joint Conference, San Diego, CA (US), American Society of Mechanical Engineers, New York, NY (US), 1999).
- 142 Ljunggren, S. & Eriksson, J. C. The lifetime of a colloid-sized gas bubble in water and the cause of the hydrophobic attraction. *Colloids and Surfaces A: Physicochemical and Engineering Aspects* **129–130**, 151-155 (1997).

- 143 Brenner, M. P. & Lohse, D. Dynamic Equilibrium Mechanism for Surface Nanobubble Stabilization. *Physical Review Letters* **101**, 214505 (2008).
- 144 Ducker, W. A. Contact Angle and Stability of Interfacial Nanobubbles. *Langmuir* **25**, 8907-8910 (2009).
- 145 Weijs, J. H. & Lohse, D. Why Surface Nanobubbles Live for Hours. *Physical Review Letters* **110**, 054501 (2013).
- 146 Zhang, X., Chan, D. Y. C., Wang, D. & Maeda, N. Stability of Interfacial Nanobubbles. *Langmuir* **29**, 1017-1023 (2013).
- 147 Battino, R., Rettich, T. R. & Tominaga, T. The Solubility of Nitrogen and Air in Liquids. *Journal of Physical Chemical Reference Data* **13**, 563-600 (1984).
- 148 Liu, X., Guo, D., Xie, G., Liu, S. & Luo, J. “Boiling” in the water evaporating meniscus induced by Marangoni flow. *Applied Physics Letters* **101**, 211602 (2012).
- 149 Petrovic, S., Robinson, T. & Judd, R. L. Marangoni heat transfer in subcooled nucleate pool boiling. *International Journal of Heat and Mass Transfer* **47**, 5115-5128 (2004).
- 150 Theofanous, T. G., Dinh, T. N., Tu, J. P. & Dinh, A. T. The boiling crisis phenomenon: Part II: dryout dynamics and burnout. *Experimental Thermal and Fluid Science* **26**, 793-810 (2002).
- 151 Nikolayev, V. S., Chatain, D., Garrabos, Y. & Beysens, D. Experimental Evidence of the Vapor Recoil Mechanism in the Boiling Crisis. *Physical Review Letters* **97**, 184503 (2006).
- 152 Nikolayev, V. S. & Beysens, D. A. Boiling crisis and non-equilibrium drying transition. *Europhysics Letters* **47**, 345 (1999).

- 153 Nikolayev, V. S., Beysens, D. A., Lagier, G. L. & Hegseth, J. Growth of a dry spot under a vapor bubble at high heat flux and high pressure. *International Journal of Heat and Mass Transfer* **44**, 3499-3511 (2001).
- 154 Ibrahim, K., Abd Rabbo, M. F., Gambaryan-Roisman, T. & Stephan, P. Experimental investigation of evaporative heat transfer characteristics at the 3-phase contact line. *Experimental Thermal and Fluid Science* **34**, 1036-1041 (2010).
- 155 Wayner, P. C. & Coccio, C. L. Heat and mass transfer in the vicinity of the triple interline of a meniscus. *AIChE Journal* **17**, 569-574 (1971).
- 156 Reyes, R. & Wayner, J. P. C. An Adsorption Model for the Superheat at the Critical Heat Flux. *Journal of Heat Transfer* **117**, 779-782 (1995).
- 157 Renk, F. J. & Wayner, J. P. C. An Evaporating Ethanol Meniscus—Part I: Experimental Studies. *Journal of Heat Transfer* **101**, 55-58 (1979).
- 158 Renk, F. J. & Wayner, J. P. C. An Evaporating Ethanol Meniscus—Part II: Analytical Studies. *Journal of Heat Transfer* **101**, 59-62 (1979).
- 159 Son, G., Dhir, V. K. & Ramanujapu, N. Dynamics and heat transfer associated with a single bubble during nucleate boiling on a horizontal surface. *Journal of Heat Transfer-Transactions of the ASME* **121**, 623-631 (1999).
- 160 Kunkelmann, C. & Stephan, P. CFD Simulation of Boiling Flows Using the Volume-of-Fluid Method within OpenFOAM. *Numerical Heat Transfer, Part A: Applications* **56**, 631-646 (2009).
- 161 Kunkelmann, C. & Stephan, P. Numerical simulation of the transient heat transfer during nucleate boiling of refrigerant HFE-7100. *International Journal of Refrigeration* **33**, 1221-1228 (2010).

- 162 Schweizer, N. & Stephan, P. Experimental study of bubble behavior and local heat flux in pool boiling under variable gravitational conditions. *Multiphase Science and Technology* **21**, 329-350 (2009).
- 163 Wayner Jr, P. C. Fluid flow in the interline region of an evaporating non-zero contact angle meniscus. *International Journal of Heat and Mass Transfer* **16**, 1777-1783 (1973).
- 164 Panchangam, S. S., Chatterjee, A., Plawsky, J. L. & Wayner Jr, P. C. Comprehensive experimental and theoretical study of fluid flow and heat transfer in a microscopic evaporating meniscus in a miniature heat exchanger. *International Journal of Heat and Mass Transfer* **51**, 5368-5379 (2008).

Vita

An Zou received his Bachelor of Science degree in chemical engineering and technology from East China University of Science and Technology (ECUST) in June 2007. Following graduation, he was admitted to the graduate program in chemical engineering at ECUST with postgraduate recommendation. He finished his research work (thesis ‘Microwave Pretreatment of Corn Stover for Ethanol Fuel Production’) for Master of Science degree in Transport Phenomena Laboratory with Professor Gance Dai in March 2010. An joined Multiscale Research and Engineering Laboratory (MREL) in mechanical and aerospace engineering at Syracuse University in January 2012 for this doctoral research with Dr. Shalabh C. Maroo. An completed his research work for the Doctor of Philosophy degree in Fall 2015.